



# Development of FENSI (Flow Enhanced Signal Intensity) perfusion sequence and application to the characterization of microvascular flow dynamics using MRI

Olivier Reynaud

## ► To cite this version:

Olivier Reynaud. Development of FENSI (Flow Enhanced Signal Intensity) perfusion sequence and application to the characterization of microvascular flow dynamics using MRI. Other [cond-mat.other]. Université Paris Sud - Paris XI, 2012. English. NNT : 2012PA112158 . tel-00740639

**HAL Id: tel-00740639**

**<https://theses.hal.science/tel-00740639>**

Submitted on 10 Oct 2012

**HAL** is a multi-disciplinary open access archive for the deposit and dissemination of scientific research documents, whether they are published or not. The documents may come from teaching and research institutions in France or abroad, or from public or private research centers.

L'archive ouverte pluridisciplinaire **HAL**, est destinée au dépôt et à la diffusion de documents scientifiques de niveau recherche, publiés ou non, émanant des établissements d'enseignement et de recherche français ou étrangers, des laboratoires publics ou privés.

UNIVERSITE PARIS SUD XI

*DOCTORAL SCHOOL: Sciences et Technologies de l'Information des  
Télécommunications et des Systèmes (STITS)*

*INSTITUTE: NeuroSpin, CEA Saclay*

*DOMAIN: Physics*

## **PhD THESIS**

September 24<sup>th</sup>, 2012

**Olivier REYNAUD**

# **Development of FENSI (Flow Enhanced Signal and Intensity) perfusion sequence and application to the characterization of microvascular flow dynamics using MRI**

Jury:

Luisa Ciobanu	PhD supervisor
Bradley Sutton	Reviewer
Emmanuel Barbier	Reviewer
Stéphane Lehéricy	Committee member
Denis Le Bihan	Committee member
Xavier Maitre	Committee member

*“Planet Earth is blue and there is nothing I can do.”*

*David Bowie.*

*“In my opinion, we don't devote nearly enough  
scientific research to finding a cure for jerks.”*

*Calvin.*

# Acknowledgements

I would like to thank here all the people that help me carry this project for more three years and a half, in good and bad times - mostly great times - and made of this final “scholar” experience a joyful journey.

I remember my excitement on my very first visit of the NeuroSpin facility in December 2008, and I still consider myself lucky to have conducted my research in such a tremendous MRI center. For that I would like to thank Pr. Denis Le Bihan, and I hope the trust that I was given will be renewed in the future towards new “theoretical-physics-backgrounded” master graduates.

Of course I should really recognize Luisa Ciobanu as my main benefactress. From the beginning and until my desk cleaning, she has always been the manager I needed in order to perform what I would call “Good Science” at NeuroSpin. I share now her enthusiasm for meticulous scientific experimentation and fairness regarding work recognition. I have also learned so much from her as system manager, and especially how to debug a 1.5 million dollar machine (only when necessary, of course). This was a real pleasure and I should probably thank Bruker too, for that matter.

I would also like to thank Pr. Stéphane Lehericy for accepting to be the president of my PhD defense jury, Bradley Sutton and Emmanuel Barbier for reviewing my manuscript and Xavier Maitre for completing - along with Luisa and Denis - this very nice jury.

Dear colleagues I had a blast working with you and I wish you the very best for the rest of life. I am sure that our paths will cross again, I will make sure that our paths will cross again and will always remember the warmest welcome from the Microscopy and the Iseult group. Benjamin, Julien, Benoit, Céline, Nadya, Françoise and Ileana ☺ be sure that if I ever smiled or laughed during these three years it was because of you. I sure hope it worked both sides. Recently Alfredo, Guillaume and Ludovic (briefly but with brio) took over, and I am glad to see that our seats will not remain empty.

I want to thank Julien, Sébastien, Fawzi, Aurélie and Franck, for all being excellent lunch partners. I did also interact with quite a lot of members of the LRMN and NeuroSpin, and you were all very kind and helpful. Thank you Eric, Marie-France, Jérémy, Béchir, Lynn, Tom, Michel, Fabrice, Cyril, Véronique, Alice, Benoit, Clarisse, Alexis, Nicolas, Philippe, Denis, Séverine, Maryline, Elizabeth...

Mulțumesc mult.

# Table of contents

Abbreviations and notations .....	10
List of tables .....	13
General Introduction.....	15
I. NMR, MRI, perfusion-MRI and FENSI .....	17
I.1 From Nuclear Magnetic Resonance to Perfusion.....	18
<i>History</i> .....	18
<i>The net magnetization</i> .....	18
<i>MR signal, relaxation times and contrast</i> .....	19
<i>Perfusion</i> .....	20
<i>Perfusion MRI in clinical neuroimaging</i> .....	21
I.2 Dynamic Susceptibility Contrast.....	22
<i>Presentation</i> .....	22
<i>Limitations</i> .....	23
I.3 Arterial Spin Labeling techniques .....	24
<i>Presentation</i> .....	24
<i>Continuous ASL</i> .....	26
<i>Pulsed ASL</i> .....	26
<i>Pseudo-continuous ASL</i> .....	27
<i>Velocity Selective ASL</i> .....	28
<i>Limitations</i> .....	28
I.3 The Flow Enhanced Signal Intensity method .....	29
<i>DESIRE</i> .....	29
<i>From diffusion to perfusion: the FENSI technique</i> .....	30
<i>Signal enhancement</i> .....	32
<i>Flux calculation</i> .....	34
<i>FENSI: state of the art</i> .....	35
II. Quantification of blood flux with FENSI .....	37
II.1 Magnetization transfer .....	38
<i>Introduction</i> .....	38
<i>Flux over-estimation</i> .....	40

<i>MT quantification</i> .....	41
<i>Conclusion</i> .....	44
II.2 Post-processing correction .....	44
<i>Process</i> .....	44
<i>First quantitative cerebral blood flux maps</i> .....	45
<i>Accuracy of the MT modelization</i> .....	48
<i>Limitations</i> .....	48
<i>Conclusion</i> .....	49
II.3 MT correction within the preparation module .....	49
<i>Pulse sequence modification</i> .....	49
<i>Experimental removal of MT effects</i> .....	51
<i>Influence of the remaining <math>MTR_{FENSI}</math> on flux calculation</i> .....	52
<i>Quantitative Cerebral Blood Flux maps at 7 Tesla</i> .....	53
<i>Discussion and conclusion on the two correction protocols</i> .....	54
II.4 Discussion on CBFlux quantification.....	55
<i>On the removal of magnetization transfer effects</i> .....	55
<i>One technique, two flux formula</i> .....	56
<i>Labeling efficiency and blood transversal relaxation time</i> .....	57
<i>Blood longitudinal relaxation time</i> .....	57
<i>Which reference should we use to quantify blood flux?</i> .....	58
<i>Blood flux and flowing spins fraction</i> .....	59
<i>CBF, CBFlux and Q</i> .....	59
<i>On the comparison between FENSI and ASL</i> .....	60
<i>Conclusion</i> .....	60
III. Quantifying brain tumor microvascular flow dynamics using FENSI.....	61
III.1 Glioblastoma Multiforme and perfusion MRI.....	62
<i>Glioblastoma</i> .....	62
<i>Angiogenesis &amp; Tumor Grading</i> .....	62
<i>Perfusion MRI</i> .....	63
<i>Characterizing tumor microvasculature with FENSI</i> .....	63
III.2 The 9L gliosarcoma rat brain tumor growth.....	63
<i>The 9L gliosarcoma</i> .....	64
<i>Animal Experiments</i> .....	64
<i>Cell implantation</i> .....	64

<i>Imaging protocol</i> .....	65
<i>Tumor Growth</i> .....	65
III.3 CBF <sub>flux</sub> quantification at early and late tumor stage .....	66
<i>Acquisition parameters</i> .....	66
<i>Cerebral blood flux map</i> .....	67
<i>ROI in tumor/healthy region and data analysis</i> .....	67
<i>Early stage tumor blood flux</i> .....	68
<i>Late stage tumor blood flux</i> .....	70
<i>Imprecision on flux calculations</i> .....	71
<i>Choice of axial orientation</i> .....	71
<i>Consistency with literature on 9L perfusion</i> .....	72
III.4 Compartmentalization of tumor at late stage .....	72
<i>9L glioma segmentation based on microvascular flux calculation</i> .....	72
<i>Immunohisto-chemistry and microvessel concentration</i> .....	74
<i>Discussion</i> .....	76
IV. Towards FENSI functional MRI .....	79
IV.1 fMRI, BOLD, CBF and CBF <sub>flux</sub> .....	80
<i>Mapping cerebral activity with MRI</i> .....	80
<i>The BOLD signal</i> .....	80
<i>BOLD fMRI</i> .....	81
<i>Perfusion fMRI versus BOLD fMRI</i> .....	82
IV.2 Preclinical BOLD and FENSI fMRI at 7 T .....	84
<i>The fMRI set-up</i> .....	84
<i>Functional MRI parameters: starting point</i> .....	85
<i>Parameters optimization</i> .....	86
<i>The BOLD response to electrical stimulation at 7 T</i> .....	87
<i>FENSI fMRI: temporal resolution and SNR</i> .....	90
<i>FENSI fMRI: the hypercapnia challenge at 7 T</i> .....	90
<i>CBF<sub>flux</sub> changes during forepaw electrical stimulation at 7 T</i> .....	92
IV.3 UHF, BOLD contrast and CBF <sub>flux</sub> .....	93
<i>Increased sensitivity to anesthesia at UHF</i> .....	93
<i>Imaging the venous system at 7 and 17.2 T</i> .....	93
<i>Influence of magnetic field on BOLD contrast during general anesthesia</i> ...	94
<i>Quantification of anesthesia effect on BOLD contrast at 17.2 T</i> .....	95



<i>Anesthesia: a contrast agent at UHF</i> .....	97
<i>Future use of UHF</i> .....	98
<i>BOLD fMRI: Echo Time and magnetic field dependence</i> .....	99
<i>The experimental BOLD response at 17.2 T</i> .....	100
<i>SNR, temporal SNR and discussion on FENSI fMRI</i> .....	101
<i>Perspectives on the use of FENSI fMRI at UHF</i> .....	102
V. Mapping brain microvasculature and its orientation with FENSI .....	105
V.1 Velocity range and microvasculature .....	106
<i>Clinical standards using conventional ASL and limitations</i> .....	106
<i>Velocity-Selective ASL</i> .....	107
<i>The FENSI enhancement versus blood velocity</i> .....	107
<i>Microvascular flux</i> .....	109
<i>Blood longitudinal relaxation time <math>T_{1b}</math> and FENSI</i> .....	111
<i>Utilization of the FENSI method</i> .....	112
V.2 Probing flow orientation.....	114
<i>Influence of blood flow orientation on flux measurement</i> .....	114
<i>In vivo CBFlux measurements in multiple directions</i> .....	115
<i>Non-directionality of microvascular blood flux</i> .....	117
<i>Feasibility of a flux tensor</i> .....	118
<i>Potential applications</i> .....	118
VI. Gains, pitfalls, perspectives and applications.....	121
VI.1 The perks of using FENSI .....	122
<i>FENSI versus DSC-MRI: non-invasiveness</i> .....	122
<i>FENSI versus DSC-MRI: absolute quantification</i> .....	122
<i>On ASL &amp; FENSI</i> .....	123
<i>FENSI versus ASL: slow flows and transit time effects</i> .....	123
<i>FENSI &amp; ASL: arbitrary tagging</i> .....	124
<i>Conclusion</i> .....	124
VI.2 The FENSI technique: pitfalls and limitations .....	124
<i>Single Slice Imaging</i> .....	125
<i>Temporal resolution</i> .....	125
<i>Contamination by macrovasculature</i> .....	126
<i>Temporal Signal-to-Noise Ratio</i> .....	128
<i>Conclusion</i> .....	129

VI.3 The FENSI technique at UHF: gains and roses.....	129
<i>Increase of the blood longitudinal relaxation time at high field</i> .....	129
<i>SNR increase at high field</i> .....	131
<i>Susceptibility artefacts</i> .....	132
<i>Efficiency of the labeling and refocusing of the spins</i> .....	133
<i>On the use of UHF</i> .....	134
VI.4 Perspectives and applications .....	135
<i>FENSI and Intra Voxel Incoherent Motion</i> .....	135
<i>FENSI functional MRI</i> .....	136
<i>Pharmacological MRI / Treatment follow-up</i> .....	137
<i>Cerebrovascular diseases, ischemia and collateral flow</i> .....	137
<i>Muscular diseases</i> .....	138
General conclusion .....	139
References .....	141
Appendix – List of relevant publications .....	155

# Abbreviations and notations

## Imaging Techniques

(P/VS) ASL	(Pulsed/Velocity-Selective) Arterial Spin Labeling
(C/PC) ASL	(Continuous/Pseudo-continuous) Arterial Spin Labeling
CT	Computed Tomography
DESIRE	Diffusion Enhanced Signal Intensity and Resolution
DSC	Dynamic Susceptibility Contrast
DTI / DWI	Diffusion Tensor / Diffusion Weighted Imaging
EPI	Echo Planar Imaging
BGS	Background Suppression
BOLD	Blood Oxygenation Level Dependent
FAIR	Flow-sensitive Alternating Inversion Recovery
FENSI	Flow Enhanced Signal Intensity
FLASH	Fast Low Angle Shot
GE	Gradient Echo
IVIM	Intra-voxel Incoherent Motion
MRA	Magnetic Resonance Angiography
MRI	Magnetic Resonance Imaging
PET	Positron Emission Tomography
RARE	Rapid Acquisition with Relaxation Enhancement
SE	Spin Echo
SPECT	Single Photon Emission Computed Tomography
TILT	Transfer Insensitive Labeling Technique
UHF	Ultra High Field

## Parameters

ADC	Apparent Diffusion Coefficient ( $\text{mm}^2/\text{s}$ )
$B_0$	Static Magnetic Field (T)
$B_1$	Oscillating Magnetic Field, perpendicular to $B_0$ (T)
BPM	Beats Per Minute ( $\text{min}^{-1}$ )
CBF	Cerebral Blood Flow ( $\text{mL}/\text{min}/100\text{g tissue}$ )
CBFlux	Cerebral Blood Flux ( $\mu\text{L}/\text{min}/\text{cm}^2$ )
CBV	Cerebral Blood Volume (%)
FA	Flip Angle ( $^\circ$ )
FOV	Field of View ( $\text{mm}^2$ )
Hct	Hematocrit rate (%)
$M_z$	Longitudinal magnetization (A/m)
MTT	Mean Transit Time (s)
MT / MTR	Magnetization Transfer / Magnetization Transfer Ratio (%)
ROI	Region of Interest ( $\text{mm}^2$ )
SNR	Signal-to-Noise Ratio
$T_1$ ( $T_{1b}$ )	(Blood) Longitudinal Relaxation Time (s)
$T_2$ ( $T_{2b}$ )	(Blood) Transversal Relaxation Time (s)
TBF	Mean Tumor Blood Flow ( $\text{mL}/\text{min}/100\text{g tissue}$ )
TBFlux	Mean Tumor Blood Flux ( $\mu\text{L}/\text{min}/\text{cm}^2$ )
TE	Echo Time (s)
TI	Inversion Time (s)
TR	Repetition Time (s)
$T_{\text{SAT}}$	Total Saturation Time (s)
VOI	Volume of Interest ( $\text{mm}^3$ )

## Structures

$^1\text{H}$	Proton
BBB	Blood Brain Barrier
CD31	Cluster of Differentiation 31 (endothelial cell staining)
CNS	Central Nervous System
CSF	Cerebro-Spinal Fluid
GBM	Glioblastoma Multiforme
Gd	Gadolinium
GM	Gray Matter
(oxy)Hb	(Oxygenated) Hemoglobin
MCA	Major Cerebral Artery
MNU	N-methyl-N-nitrosourea
PFA	Paraformaldehyde
S1	Primary Somatosensory Cortex Area
V1	Primary Visual Area
WM	White Matter

## Institute

CEA	Commissariat à l'Energie Atomique
DSV	Direction des Sciences du Vivant
LRMN	Laboratoire de Résonance Magnétique Nucléaire

## List of tables

Table 1 MTR (%) in white and gray matter introduced by the FENSI tag.....	44
Table 2 List of experimental parameters used for calculation of cerebral blood flux with FENSI at 7 Tesla.....	46
Table 3 Comparison of the FENSI flux ratio WM/GM with the CBF ratio obtained with other methods.....	47
Table 4 <i>In vivo</i> and <i>ex vivo</i> CBFlux calculated with FENSI in the rat brain ....	52
Table 5 Parameters of the MT balanced FENSI Spin Echo EPI sequence at 7 Tesla .....	53
Table 6 List of optimized stimulation parameters to perform BOLD fMRI using medetomidine at 7 T .....	87
Table 7 Set of imaging parameters used to probe blood oxygenation level. ....	94
Table 8 Ratio of the number of hypo-intense pixels counted for different anesthesia conditions at 17.2 T.....	97
Table 9 Effect of isoflurane, ketamine-xylazine and medetomidine on different physiological parameters.....	98
Table 10 Methods to improve the detection of slow flows with FENSI .....	109
Table 11 $T_{1b}$ of arterial blood measured at various field strengths .....	130
Table 12 Comparison of the FENSI parameters used to perform <i>in vivo</i> CBFlux measurements at 7 and 17.2 T .....	132



# General Introduction

The discoveries, implementations and developments of NMR and MRI have had a major impact in medical imaging. Compared to other imaging modalities (PET, SPECT, CT, optical imaging), current MRI research helps to further and better understand the inner mechanisms of the human body in a less invasive manner. In clinical neuroimaging, perfusion MRI is of spectacular importance to study cerebrovascular diseases and cancer.

However, at the moment, there is no perfusion MRI sequence that allows for a complete and precise quantification of microvascular flow dynamics. In this manuscript we investigate the use of the recently introduced Flow Enhanced Signal Intensity method (FENSI) to characterize and quantify vasculature at capillary level. Potentially of great interest in functional MRI (fMRI) and in perfusion MRI in general, additional studies need to be performed to assess the utility of the FENSI sequence compared to the already existing perfusion MRI techniques.

For that purpose, the first step of our investigation is the possible quantification of blood flux *in vivo* with FENSI. This feature is shared by the Arterial Spin Labeling (ASL) techniques and represents a huge advantage compared to the other minimally-invasive perfusion MR methods (whose advantage is the increased SNR). The combination of flux quantification and flow-enhanced signal (compared to ASL) can make of FENSI an ideal method to characterize in a complete non-invasive way the brain microvasculature. The second chapter of the manuscript is therefore dedicated to the investigations towards the removal of the magnetization transfer (MT) effects introduced by the FENSI preparation module. Our quantification strategy is discussed and compared with the recent work of colleagues on the implementation of the FENSI technique in a human scanner.

Only after the FENSI pulse sequence has been modified to allow for balanced MT effects between “control” and “tag” images we are able to characterize CBFlux in an animal model. The third chapter of this manuscript presents the first preclinical application of the FENSI sequence at 7 Tesla. The blood flow dynamics are studied with FENSI in a very aggressive and propagative rat brain tumor model: the 9L gliosarcoma. Our objective is to assess whether FENSI is suitable for a longitudinal non-invasive characterization of microvascular changes associated with tumor growth. The results obtained with FENSI are compared with literature on 9L perfusion and immunohisto-chemistry.



In the first paper published on FENSI (1) we casted a first glance on the potential of the flow enhanced technique when applied to fMRI. The results obtained at the time were indeed contaminated by MT effects. With the implementation of a new MT-free FENSI technique, we investigate the possibility to map the brain cerebral functioning based on a quantitative physiological parameter (CBFlux) more directly related to neuronal activity than the usual BOLD signal. At ultra-high field (UHF), the influence of different anesthetics on the rat brain microvascular network is also considered. Results are presented in chapter 4.

The FENSI technique can be sensitized to various blood velocities. In chapter 5 we detail the influence of the different imaging parameters on the flux-weighted contrast obtained with flow-enhanced MRI. The interested researcher will access precious information to implement the technique. The influence of the flow directionality on the flux measurements is presented and discussed.

After many developments around the FENSI technique, we detail the strengths and weaknesses of the method, its characteristics, ‘precautions for use’, and potential main applications. Future methodological developments and potential improvements are also discussed. After optimization of the technique at 17.2 T, the gain in SNR, the advantages and drawbacks of UHF are investigated. We also propose a range of applications of interest for the FENSI technique, where MRI can gain from the use of that particular technique compared to ASL or Dynamic Susceptibility Contrast (DSC-MRI).

# **I. NMR, MRI, perfusion-MRI and FENSI**

A brief introduction reminds the reader of the major discoveries that have led to the development of Nuclear Magnetic Resonance and Magnetic Resonance Imaging in the last fifty years. A short description of the mechanisms of MR signal generation and acquisition illustrates the various parameters MRI can be sensitized to. The particular domain of perfusion MRI, its utility and application in clinical neuroimaging are detailed.

After introducing perfusion MRI, the two main types of methods used to characterize cerebral blood flux are presented: Dynamic Susceptibility Contrast MRI (DSC-MRI) and Arterial Spin Labeling (ASL). These two techniques are based on different contrast mechanisms and use respectively exogenous and endogenous tracers to probe the cerebral vasculature.

The basic principles, advantages and drawbacks of DSC-MRI and ASL are presented and discussed. We highlight the fact that today there is no ideal MRI method to assess efficiently the brain vascular malfunctions.

Originally deriving from a diffusion MR sequence, the Flow Enhanced Signal Intensity (FENSI) method is finally introduced. The FENSI method repeatedly saturates spins in a thin slice of interest and acquires signal from all the spins that escape the labeling plane. Compared to ASL techniques, it has the potential to obtain significant signal enhancement.

FENSI is a new technique and very few groups have implemented it and studied its possible applications. We present the different approaches chosen in this manuscript to answer the question: How does FENSI stand compared to conventional perfusion MRI? Our research field extends from blood flux quantification to blood flow dynamics, functional MRI, ultra high field imaging or interactions between diffusion and perfusion.

## I.1 From Nuclear Magnetic Resonance to Perfusion

The aim of this section is to introduce NMR and MRI; and briefly explain how the NMR signal is generated, acquired and sensitized to perfusion. The main applications of perfusion MRI in clinical neuroimaging are also described.

### *History*

The basic principles of Nuclear Magnetic Resonance (NMR) were discovered independently by Bloch (2) and Purcell (3) in 1946. Both share the Nobel Prize of Physics in 1952 for this achievement. NMR has been used extensively since to study molecular structures and diffusion. The first MR images were reported by Lauterbur (4) and Mansfield (5) in 1973 by adding linear magnetic field gradients to the MR system.

The technique, baptized Magnetic Resonance Imaging (MRI), allows for non invasive *in vivo* physiological measurements and can combine precious anatomical and metabolic information. Compared to other medical imaging modalities (CT, PET, SPECT), MRI presents high spatial resolution and increased soft tissue contrast. Its flexibility makes it suitable for various applications. Over the years, developments in MRI have increased general knowledge on clinical diagnostic, response to treatment, cardiac flow dynamics, cognitive performances or tissue degradation for instance. Up to this date, no health risk is known when performing or receiving an MRI scan under normal procedures.

### *The net magnetization*

The interested reader will refer to specialized literature on MRI such as [Haacke et al, 1999] (6) for a quantum description of the NMR phenomenon. We will focus here on its classical description.

The atoms possessing an odd number of protons and/or neutrons exhibit a nuclear spin angular momentum. In what follows we will refer to these atoms as spins. In biology,  $^1\text{H}$  is often used as it is the most abundant spin and produces the largest signals.

In the absence of magnetic field, the spins are randomly oriented. The macroscopic net magnetization (sum of the small magnetic momenta) is null.

The application of a static magnetic field  $B_0$  induces major changes at microscopic level. The spins align in a parallel or anti-parallel direction with respect to the main magnetic field and generate at thermal equilibrium a net magnetization. This 'longitudinal' magnetization is proportional to the strength of  $B_0$  and points in the direction of  $B_0$ . Resonant absorption occurs at Larmor frequency  $\omega$  (in Hz) defined by equation [1.1] when the energy of a single photon  $\hbar\omega$  matches the energy gap between the two different spin states (parallel/anti-parallel,  $\Delta E = \gamma\hbar B_0$ ).

$$\omega = \gamma * B_0 \quad 1.1$$

where  $\gamma$  is the gyro-magnetic ratio (in Hz/T) and is nuclei dependent ( $\gamma = 42.58$  MHz/T for  $^1\text{H}$ ). The spins can be excited by any radiofrequency magnetic field at Larmor frequency. If excited, they will start to oscillate and produce a signal, also oscillating at Larmor frequency.

### *MR signal, relaxation times and contrast*

In presence of an external field at Larmor frequency  $B_1$  in the transverse plane (orthogonal to  $B_0$ ), the spins and magnetization vector start to precess in phase. The spins in the parallel state absorb energy from the  $B_1$  field and make a transition to the anti-parallel state. The magnetization rotates depending on  $B_1$  strength and duration.

After  $B_1$  turns off, the magnetization precesses around  $B_0$ . As it goes back to equilibrium along  $B_0$ , it generates, according to Faraday's law, an electromotive force and a signal (called *free induction decay* or FID) can be detected using a receiver oriented to detect magnetization changes in the transverse plane.

In the transverse plane, the magnetization is subject to a rapid and exponential decay. This phenomenon is due to the dephasing and loss of coherence of the spins, and is characterized by the transverse relaxation time  $T_2$ . The return to equilibrium of the longitudinal magnetization along  $B_0$  is characterized independently by the time constant  $T_1$ , known as the longitudinal relaxation time.

Depending on the radio-frequency pulse scheme, delays and magnetic fields gradients applied to the system, the measured NMR signal can be sensitized to several parameters such as  $T_1$ ,  $T_2$ , proton density, diffusion or perfusion for instance.

In clinical practice, these multiple contrasts inform on different physiological properties of real use for the diagnosis of cerebral pathologies. For instance, tissue oxygenation (related to brain activity) and degradation (such as edema) is visible through changes in  $T_2^*$  and  $T_2$ . Based on  $T_1$  contrast, the accumulation of paramagnetic MR contrast agents highlights the cerebral structures affected by the disruption of the Blood-Brain-Barrier (BBB) in cancer. On the other hand, dynamic  $T_2$  and  $T_2^*$ -weighted acquisitions can inform on the propagation of the same paramagnetic compound and will reflect cerebral macro- and microvasculature, respectively. Proton densities or diffusion have other applications, and one will rather investigate articulations or white matter tract diseases (such as mild cognitive impairment or Alzheimer) using these techniques. The present manuscript focuses exclusively on perfusion MRI, whose main applications are cancer, stroke and functional MRI.

### *Perfusion*

Perfusion, typically characterized using cerebral blood flow (CBF) and measured in ml/g/min, reflects the volume of blood delivered to tissues per brain mass unit and per unit of time. CBF characterizes the exchange of oxygen and nutrients to the tissues or the organs and is therefore an efficient biomarker of the well-functioning organism.

The sensitivity of NMR to the motion of spins has been studied for a long time. Different techniques have been developed to probe the brain vascularization. Magnetic Resonance Angiography (MRA) has for instance encountered a huge success in radiology by providing 3D maps of the brain macrovasculature (arteries and veins with relatively high blood velocity). Other methods, like Intra-Voxel Incoherent Motion (IVIM) developed by Le Bihan et al. (7) in 1986, tried to access microvasculature considering the random nature of blood motion in the capillary network. The technique did not meet its audience at the time due to insufficient MR hardware to perform true quantification. Very recent studies (8-10) show however a regain of interest towards IVIM.

In clinical practice, there are two main classes of perfusion MRI methods currently used to characterize brain microvasculature: bolus tracking after an injection of exogenous contrast agent (Dynamic Susceptibility Contrast, or DSC-MRI) and labeling of water protons as an endogenous contrast agent (Arterial Spin Labeling, or ASL). True and absolute quantification of CBF requires the passage of a tracer from the vasculature to the tissues (from the intra- to the extravascular compartment). In DSC-MRI, the use of pure intravascular contrast agents and CBF estimation based on

hemodynamic measurements is however considered as perfusion imaging. DSC-MRI and ASL techniques will be introduced in the next sections.

### *Perfusion MRI in clinical neuroimaging*

Perfusion imaging provides a fantastic tool to probe the malfunctions of the cerebral vascular mechanisms. In normal patients, DSC-MRI and ASL studies have shown a longitudinal decrease of the CBF with aging (11). This effect needs to be taken into account when performing important studies including a large population of patients. An increase of CBF has also been reported on pediatric subjects (12).

In the brain, perfusion can be measured in most structures. Calculation of CBF in Gray Matter (GM) is for instance easily achievable in reasonable scan times. However, the accuracy of the CBF estimation in White Matter (WM) with ASL can suffer from the extended blood transit times associated with the slow blood velocity in these regions. Recent studies report significant measurements of CBF in WM above the limit of detection when performing pseudo-continuous ASL at high magnetic field (13).

Applied to cerebrovascular diseases, perfusion MRI can predict recurrent stroke (14). Both DSC-MRI and ASL techniques are in good agreement with MRA and clinical symptoms. Associated with Diffusion Weighted Imaging (DWI), the tissues with possible reperfusion can be targeted in acute stroke based on the perfusion-diffusion mismatch (15). Perfusion studies of regions with elevated blood transit times are also of great interest as collateral flow seems to be correlated with positive clinical outcome in stroke (16-17) and other cerebrovascular disorders (18).

In cancer, the regional Cerebral Blood Volume (CBV) obtained with DSC-MRI is a potential marker of tumor grade and increased vasculature. The local characterization of microvessels (mean vessel diameter, mean vessel density, vessel size index) can also reflect the angiogenic process associated with tumor growth (19-20). Both ASL and DSC-MRI can distinguish low grade (I-II) from high grade (III-IV) tumors (21-22). DSC-MRI is used to assess vessel permeability, whereas ASL provides quantitative information and suffers less from disruption of the BBB. After treatment, CBF mapping can help the clinician to distinguish recurrent high grade gliomas from radiation necrosis (23). Inside the tumor, hypo-perfused regions usually characterize cysts, calcification, hemorrhage or necrosis.

Many more brain pathologies and cognitive disorders can be characterized by modifications at microvascular level. These include for

instance Alzheimer’s disease (24-25), mild cognitive impairments and dementia (26), epilepsy (27-28) or CNS infections (29).

Last but not least, perfusion MRI was recently considered to investigate cognition and neuronal activation (30). Commonly performed with Blood Oxygen Level Dependent (BOLD) techniques (31), functional MRI (fMRI) measures classically an indirect marker of the brain activity based on  $T_2^*$  contrast due to local changes in deoxyhemoglobin concentration inside the venous system. ASL performed at high temporal resolution can in principle provide a true and quantitative measurement of neuronal activation. Perfusion fMRI can therefore reduce the inter-subject and inter-platform variability obtained with BOLD, and is more adapted to detect longer time scales changes. In practice, CBF maps are less artefacted but present very low SNR compared to BOLD images.

## **I.2 Dynamic Susceptibility Contrast**

We will present in this section the main perfusion MRI technique used in the clinic to characterize cerebral blood flow *in vivo*.

### *Presentation*

First proposed in 1988, the estimation of CBF using DSC-MRI is based on the dynamic tracking of a bolus of paramagnetic contrast agent through the vascular network (32-33). After injection of a bolus of Gadolinium compound (typically 0.1 to 0.3 mmol/kg), dynamic measurements of the signal loss in  $T_2/T_2^*$  weighted images reflect the time-dependent concentration of contrast material (**Figure 1.1**). Due to blood transit times on the orders of seconds, a high temporal resolution is required to observe the wash-in and wash-out of the contrast agent. This is usually achieved using Echo Planar Imaging (EPI) sequences, acquiring the complete Fourier k-space in a single repetition time. Different physiological parameters, such as CBV, Mean Transit Time (MTT) and CBF can be derived from the temporal evolution of Gd concentration, based on the tracer kinetics model for non-diffusible tracers (34-35).

The flowing spins represent in the brain only 1 to 5 % of the total population of spins per voxel. However,  $T_2^*$  weighted imaging is very sensitive to magnetic field susceptibilities, and the use of a paramagnetic contrast agent can generate up to complete signal loss in a given voxel. This makes DSC-MRI very sensitive to small concentration changes. Multi-slice CBV, MTT and CBF

maps exhibit high SNR, making DSC-MRI by far the most widely used perfusion technique in the clinic. Moreover, DSC-MRI offers the possibility to probe both macro- and micro-vasculature when associated with Gradient Echo or Spin Echo sequences (36). The determination of the local  $\Delta R_2$  and  $\Delta R_2^*$  changes after the Gd injection can also inform on the average microvessel diameter and density per voxel (20).

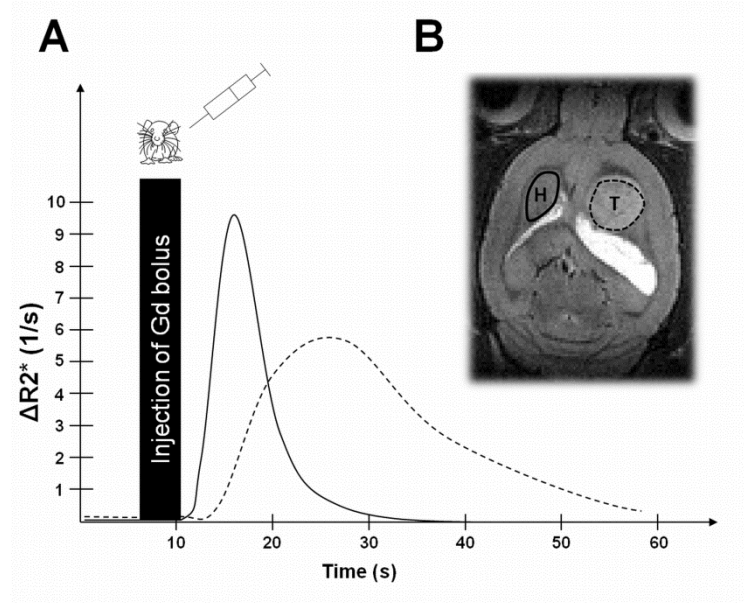


**Figure 1.1 Dynamic Susceptibility Contrast (DSC-MRI) experiment in a rat brain with a tumor.** **A.** Dynamic evolution of the transverse relaxation rate  $R_2^*$  (1/s) in tumor (dashed line) and healthy tissues (plain line) after [Gd] injection. The ROIs used for averaging (H: healthy tissue; T: tumor) are shown on the  $T_2$  weighted image (**B**). The evolution of the relaxation rate reflects the temporal concentration of contrast agent in the ROI and helps derive CBV, MTT and CBF maps of the brain.

### Limitations

There are however several drawbacks using DSC-MRI. Practical limitations include toxicity of the tracer at high dosage and invasiveness of the method. The application of DSC-MRI in patients subject to chronic renal failure led for instance to multiple nephrogenic systemic fibrosis cases (37). Allergies to the compound have also been reported. Moreover, typical contrast agents have a complete wash-out time on the orders of hours, henceforth excluding the possibility to repeat the experiment, or to apply DSC-MRI to dynamic measurements.



In addition, one must consider the reliability of the ‘absolute’ quantification performed with DSC-MRI. First, the tracer kinetics model is only valid if the contrast agent remains exclusively intravascular. Therefore it assumes an intact BBB. Leakage of contrast agent is however common in numerous cerebrovascular diseases, and particularly in the case of high grade CNS neoplasms. Special DSC-MRI protocols and post-processing correction (38-39) need to be performed in order to obtain reliable perfusion information in cases of BBB disruption. The tracer kinetics model (33) also assumes negligible delays and dispersion of the bolus as it reaches the Region of Interest (ROI), negligible  $T_1$  effect on the tissue, negligible effect of the tracer on CBF (therefore negligible volume) and no recirculation of the paramagnetic compound. All of these approximations lead to measurements imprecision and/or demand additional information to correct for it.

Second, DSC-MRI really provides relative quantification of the CBF in the brain, and knowledge on the Arterial Input Function (AIF) is required to obtain quantitative CBF. Although possible with PET or CT, this is hardly achievable using MRI. Although recent studies are still investigating the best choices of ROIs (40-41), the common method is to estimate the concentration of contrast agent in a major artery feeding the brain, such as the major cerebral artery (MCA) or the carotid artery (42). Estimation of the AIF using MRI is however subject to flow turbulence, partial volume effects, delay and dispersion due to the distance between the artery and ROI. Progress is currently being done towards automation of the AIF estimation process in order to minimize CBF quantification bias due to the user.

### **I.3 Arterial Spin Labeling techniques**

In this section we describe the ASL techniques allowing a true and completely non-invasive quantification of CBF. The different types of existing ASL sequences and their limitations are presented.

#### *Presentation*

In ASL the magnetization of water molecules in large arteries feeding the brain (MCA), is manipulated in preparation modules placed in front of conventional MRI sequences (**Figure 1.2**). After a transit time (1 to 2 s), the in-flowing labeled spins replace the spins left at equilibrium in the slice of interest. Perfusion weighted images are generated by taking the difference between “control” (without labeling) and “tag” (with labeling) images. The CBF maps are then calculated with sufficient knowledge of physiological

parameters ( $T_1$  of blood, blood-brain partition coefficient) or imaging parameters. For instance, the labeling efficiency  $\alpha$  depends on the type of radio-frequency pulse used, but also on slice/vessel orientation and blood velocity.

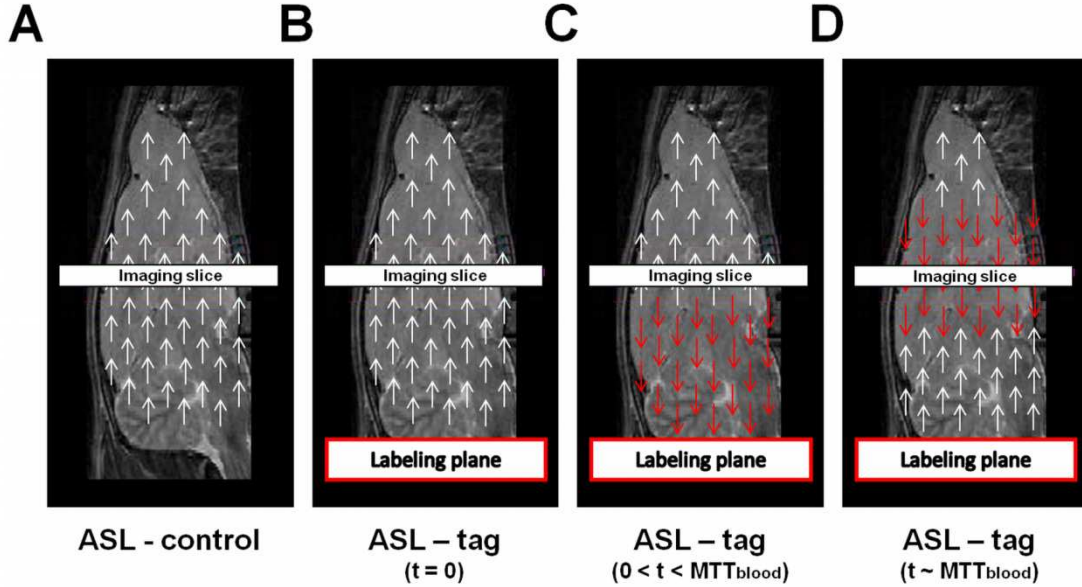


**Figure 1.2 Arterial Spin Labeling (ASL) experiment on a rat brain.** ASL slices orientation: coronal (sagittal view of a rat brain). Two datasets are required to obtain a perfusion-weighted image. **A.** The first “control” image accounts for reference and measures the magnetization of the spins (white arrows) at equilibrium. **B.** A preparation module inverts the magnetization of the spins in the MCA. The labeling plane must be oriented perpendicular to the vessel for maximum labeling efficiency. **C.** The labeled spins propagate in the brain with blood flow. **D.** After a delay corresponding to the blood transit time (1-2 s), signal is acquired in the slice of interest (“tag” image). Signal intensity difference between “control” and “tag” is proportional to the number of spins that have flown from the neck to the slice. The static tissue signals, present in both “control” and “tag” images, cancel each other.

Compared to DSC-MRI, ASL sequences offer the possibility to obtain complete non-invasive and quantitative perfusion information. This method presents the advantage to be less sensitive to permeability effects, as there is no accumulation of contrast agent: the labeled spins go back to equilibrium with relaxation time  $T_1$  (1 – 3 s). One can also use dynamic measurements to investigate local CBF changes in response to various stimuli: ASL provides new tools for fMRI. Last but not least, ASL benefits greatly from the recent developments of high and ultra magnetic field MRI scanners through the increase in  $T_1$  (allowing longer efficient labeling durations) and SNR, and is

expected to replace DSC-MRI and become the standard practice in the near future.

Under the name of ASL lie four main groups of techniques: continuous ASL (CASL), pulsed ASL (PASL), pseudo-continuous ASL (PCASL) and velocity-selective ASL (VS-ASL). These four techniques share the same basic principles described earlier (arterial blood as an endogenous contrast agent). However, their specificities make them sensitive to different phenomena that limit CBF quantification.

### *Continuous ASL*

The first CASL method was developed in 1992 by Detre et al. (43-44). In CASL, the arterial blood water is continuously labeled as the blood passes through a thin labeling plane at the base of the brain or just below the imaging plane (**Figure 1.3-A**). For maximum labeling efficiency and reduced sensitivity to transit time, the pulse used for labeling is very selective and lasts several seconds. These sequences measure steady-state blood flow and present high perfusion contrast (45). They are however difficult to implement in practice, deposit a high radio-frequency power on the patient (46) and are very sensitive to magnetization transfer (MT) effects.

### *Pulsed ASL*

In PASL, a very short pulse (covering a large area) is applied in the “tag” image. Similar to CASL, signal is then acquired after a delay TI matching the blood transit time. Preferred to CASL in clinical practice because easier to perform, a large variety of PASL sequences (EPISTAR, PTILT, PULSAR, BASE, PICORE...) have been developed since 1994 (47-53). These include classical “distal inversion” techniques (EPISTAR, **Figure 1.3-B**) and inversion-recovery techniques, such as the Flow Alternating Inversion Recovery (FAIR) (49) and FAIR-derived sequences (54-55). In the latter, the “tag” is applied with a non-selective inversion pulse, while the preparation of the “control” image selectively inverts the magnetization around the imaging slice (**Figure 1.3-C**). Due to lower radio-frequency power, PASL methods do not suffer from MT effects as much as CASL techniques. The accuracy of CBF measurements with PASL is however more sensitive than CASL to transit times variations. Recent methods (QUIPSS, Q2TIPS) (48) apply an additional saturation module after the labeling pulse to increase the precision on the estimation of the distance between labeling and imaging. CBF mapping of the whole brain is now possible with PASL techniques associated with 3D acquisition schemes (56).

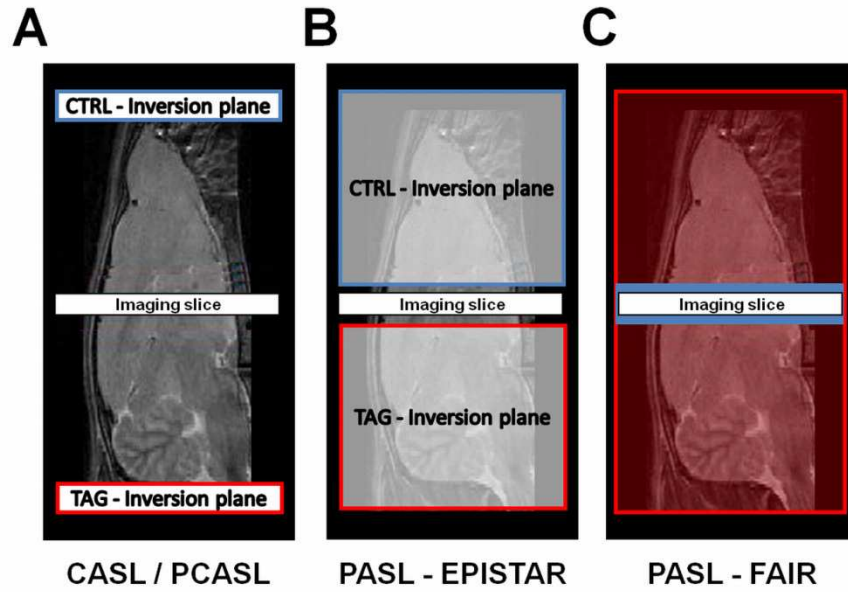


**Figure 1.3 Examples of CASL, PCASL and PASL methodologies.** **A.** Spin tagging in continuous ASL is driven by adiabatic flow-driven inversion. Typical radio-frequency pulses last 2 to 4 seconds. Pseudo-continuous ASL schemes model continuous inversion with a train of short  $180^\circ$  FA pulses. **B.** Pulsed ASL Echo Planar Imaging and Signal Targeting with Alternating Radio-Frequency (EPISTAR) labeling protocol. Inversion is achieved in the “tag” image with a short inversion pulse (5-20 ms) proximal to the slice of interest. Radio-frequency deposition is balanced in the “control” image (symmetric inversion plane). **C.** Pulsed ASL Flow Alternating Inversion Recovery (FAIR) methodology. A non-selective//selective inversion labels all the spins//the static spins in the “tag”//“control” image. After recovery, signal intensity difference reflects the inflowing spins only.

#### *Pseudo-continuous ASL*

Recently PCASL techniques have been developed to combine the easy implementation of PASL with the higher SNR of CASL. Garcia et al. (57) suggested to mimic a continuous excitation by several short pulses, thus reducing energy deposition and hardware demands. Recent studies reported that PCASL is the best compromise between labeling efficiency, SNR and sensitivity to MT effects. CBF quantification with these techniques can however suffer from  $B_0$  inhomogeneities and eddy currents (58) that might occur when implementing ASL on high field scanners.

## *Velocity Selective ASL*

Another ASL method has been created to eliminate the problem of transit time sensitivity shared by CASL, PASL and PCASL. Opposed to these techniques, VS-ASL techniques label all the flowing spins, regardless of their position (59-60). In practice, the labeling module of the “tag” image inverts the magnetization of all the spins flowing above the cut-off velocity  $v_c$ . After a delay (TI – inversion time), the imaging module acquires signal from the spins below velocity  $v_c$ . Signal intensity difference with the “control” image eliminates the static spins contribution. Therefore only the decelerating spins (with initial velocity above  $v_c$  and current velocity below  $v_c$ ) contribute to the perfusion weighted image. Because the blood in the venous system usually accelerates with time, VS-ASL truly reflects arterial blood.

## *Limitations*

The major limitation when performing ASL is the intrinsic low SNR of the perfusion weighted images. As previously discussed, the flowing spins only represent a small fraction of the entire spin population (1 - 5 %), limiting the maximum SNR with ASL. Fast encoding techniques such as Echo Planar (EPI) or Spiral Imaging need to be considered in order to optimize the SNR, making ASL subject to distortions at high field. In the clinic, numerous repetitions of “control” and “tag” images are required to map the CBF and typical ASL experiments last 4 to 6 minutes. As a consequence, CBF calculation is very sensitive to motion. Background suppression (eliminating the noise coming from static tissue) and motion correction techniques can highly improve the image quality (13,61).

MT effects due to high radio-frequency power can lead to major overestimation of CBF with ASL (62), especially when performing CASL and PCASL. When possible, symmetric radio-frequency deposition between “control” and “tag” in ASL techniques (**Figure 1.3**) lead to reduced MT effects on CBF calculation. This is however not always possible, due to Specific Absorption Rate (SAR) or design constraints. In that case, one will use two-coils systems (labeling/imaging) actively decoupled during the acquisition (63-65).

Another drawback of ASL is the inefficient and unequal contribution of the labeled spins to the perfusion weighted signal. In many cerebrovascular diseases such as stroke, tumors or arterial occlusions, the vascular tree is affected and the blood circulation hindered. CBF calculation with CASL, PASL and PCASL is inaccurate in regions where the labeled blood does not reach the imaging slice during TI. These problems can be overcome by using specific

pulse sequences modifications using multiple TIs, at cost of extended scan times (66) and increased  $T_1$  relaxation of the labeled spins. In practice, ASL is a poor choice to measure perfusion when in presence of collateral flow or small blood velocities.

### **I.3 The Flow Enhanced Signal Intensity method**

This section will introduce the Flow Enhanced Signal Intensity method, its origin, principle and potential advantages compared to ASL and DSC-MRI.

#### *DESIRE*

With the recent emergence of high magnetic fields and gradients strengths, MRI can achieve higher and higher spatial resolution (67-68). At such a high resolution (a few micrometers), the mechanisms of diffusion usually lead to a decrease of the already low SNR typically obtained in Magnetic Resonance Microscopy using standard acquisition strategies. As opposed to this, Paul Lauterbur et al. proposed first in 1992 (69) an original imaging scheme called DESIRE (Diffusion Enhancement of Signal and REsolution) to increase the sensitivity of diffusion NMR techniques.

The underlying principle of DESIRE is the following. By repeatedly saturating at microscopic level, one generates a signal loss depending on the Brownian motion of the saturated spins. When the spins accumulate and the typical diffusion distances exceed the saturation size, the missing magnetization can be magnified by a factor much larger than unity. Depending on spatial resolution, diffusion degree of freedom (**Figure 1.4-A**; 1D, 2D or 3D implementation) and saturation period (70), the first prospects into DESIRE predict a signal increase of one to three orders of magnitude (**Figure 1.4-B**). The signal difference between the images acquired with and without repeated saturation is often referred to as signal enhancement (compared to a single saturation).

A first experimental diffusion enhancement of factor 8 was reported in 1D on plant stems by Ciobanu et al. (71) using a 8  $\mu\text{m}$  thick infinite saturation plane. More recently, an enhancement of 25 was obtained with 5  $\mu\text{m}$  resolution (72). The first 2D implementation of DESIRE was recently achieved at ultra high magnetic field (17.2 T) (73). MRI Experiments were however constrained by gradient strength and duty cycle, greatly increasing the minimum size of the saturation “hole” (60  $\mu\text{m}$ ) and reducing the diffusion time, therefore providing limited diffusion enhancement ( $\sim 2.3$ ). In the future, the use

of DESIRE at lower magnetic field associated with very strong gradients (1-10 T/m) is expected to produce unique diffusion contrast at high resolution. This can potentially help to resolve the mechanisms of diffusion, still poorly understood at cellular level.

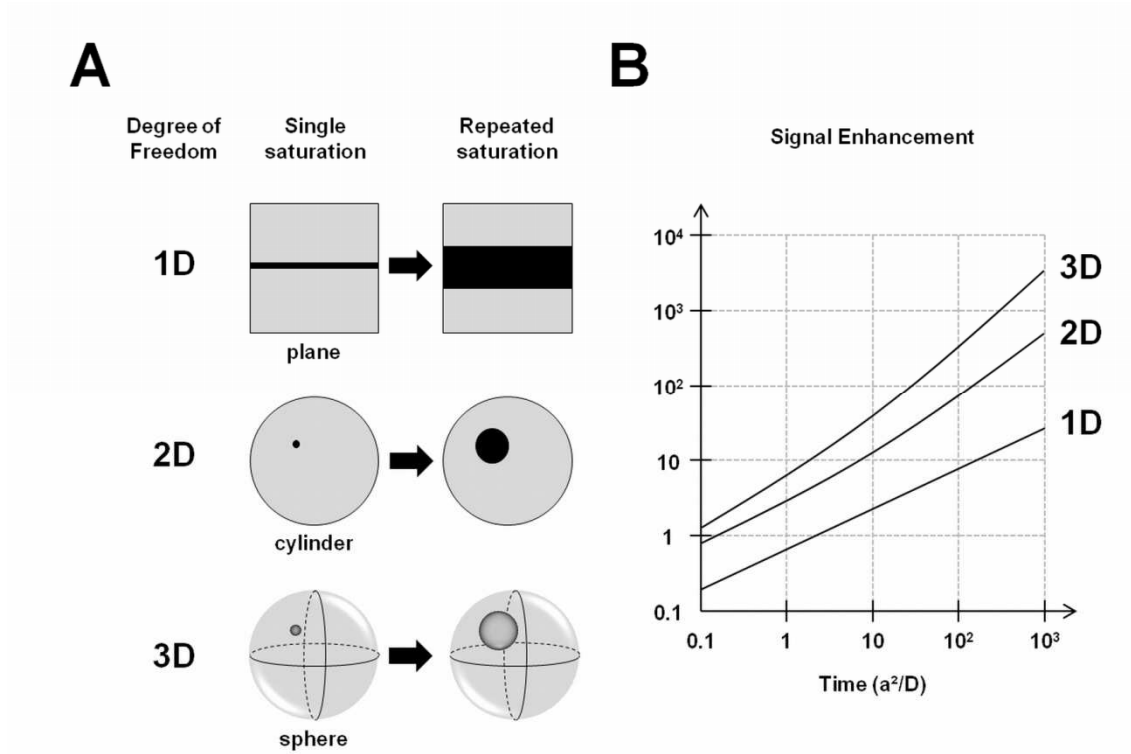


**Figure 1.4 DESIRE experiment** **A.** Representation of the missing magnetization (black area) before and after diffusion when implementing the DESIRE technique in 1, 2 or 3 dimensions. **B.** Theoretical signal enhancement versus diffusion time (normalized to  $d_{\text{sat}}^2/D$ , where  $d_{\text{sat}}$  is the radius of saturation and  $D$  the diffusion coefficient), taken from (70). The more dimensions diffusion can expand into, the larger the signal enhancement. Practical implementation of 2D and 3D DESIRE experiments is however difficult and demands excellent hardware.

#### *From diffusion to perfusion: the FENSI technique*

The Flow Enhanced Signal Intensity (FENSI) method is a direct extension of the DESIRE technique implemented in 1D. When compared to diffusion distances blood water molecules travel much longer (velocities of 1 – 100 mm/s) and therefore the same technique can lead to high signal enhancements even for relatively large saturation thicknesses (300 – 2000  $\mu\text{m}$ ) (**Figure 1.5**).

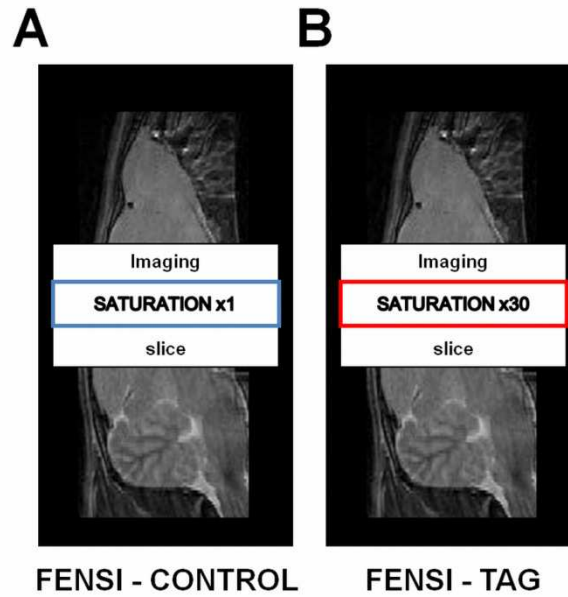


**Figure 1.5 Schematic of a FENSI experiment in a rat brain. A.** A first “control” image is acquired to measure the magnetization in the imaging plane. A single saturation slice is used to eliminate the contribution of the static tissue to the signal. **B.** The original “tag” preparation module (1) consisted in 30 consecutive saturation pulses (total saturation time 330 ms). Signal intensity subtraction provides information on the spins that have flown through the labeling plane during the saturation period.

FENSI generates contrast based on flow mechanisms. Moreover, the precise signal enhancement depends on the number and the velocity of the spins that are being repeatedly labeled. In a typical two dimensional *in vivo* MR acquisition (XY plane), a thin saturation slice (equivalent to 1D DESIRE saturation, **Figure 1.4**) labels all the spins in the middle of the imaging slice (**Figure 1.6**). Assuming a blood flow orthogonal to the saturation plane (along Z), the labeled spins will more or less rapidly exit the labeling plane and be replaced by new unlabeled spins, depending on their velocity. The more saturation pulses are used, the more spins are being tagged and generate a decrease of magnetization in the imaging plane. When the preparation module has finished, the signal enhancement  $E$  depends on the number of spins that have flown through the saturation plane but remain in the imaging plane. Therefore FENSI can potentially provide a gain in SNR compared to the classical ASL techniques used to assess local brain perfusion.



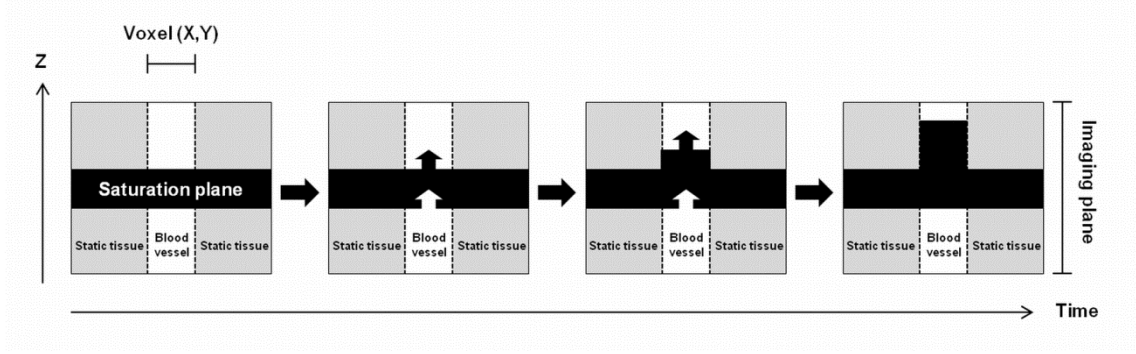


**Figure 1.6 Build-up of the saturation due to flowing blood.** The white rectangle represents the magnetization (proportional to the number of unlabeled spins) in the blood vessel voxel of coordinates  $(X,Y)$  of the imaging plane. As spins continuously flow through the thin saturation plane, they build up saturation in the imaging plane. The signal enhancement obtained with FENSI compared to a single saturation depends on many parameters, such as blood velocity and blood concentration, saturation and imaging plane thicknesses or total saturation time.

After this first introduction to FENSI, we will now explain quantitatively how the signal is sensitized to the blood velocity and how cerebral blood flux is measured with FENSI.

### Signal enhancement

In what follows, we will often use the term “missing magnetization” ( $m$ ) defined as  $m(x,y,z,t) = 1 - M(x,y,z,t) / M_0(x,y,z)$ .  $M$  and  $M_0$  represent the macroscopic magnetization inside the voxel of coordinates  $(x,y)$  at time  $t$  and at equilibrium, respectively. Based on the DESIRE equations (70), the signal enhancement  $E$  is related to the missing magnetization  $m$  by equation [1.2]

$$E(x, y, t) = \frac{1}{2 * L_{SAT}} * \int_{|z| > L_{SAT}/2}^{|z| < L_{IMG}/2} m(x, y, z, t) dz \quad 1.2$$

where  $L_{SAT}$  and  $L_{IMG}$  represent the saturation and the imaging slice thicknesses. Assuming negligible  $T_1$  relaxation of the labeled spins, the evolution of the missing magnetization during the saturation period is governed by equation [1.3]

$$\frac{\partial m}{\partial t} + v * \frac{\partial m}{\partial z} = D * \frac{\partial^2 m}{\partial z^2} \quad 1.3$$

where  $D$  and  $v$  are the diffusion coefficients and spin velocity, assumed to be uniform and constant at position  $(x,y)$  during saturation. The saturation slice dictates the following boundary conditions [1.4].

$$\begin{aligned} m_{|z| > L_{sat}/2} &= 0 & \text{for } t \leq 0 \\ m_{|z| \rightarrow \infty} &= 0 & \text{for } t = 0 \\ m_{|z| \leq L_{sat}/2} &= 1 & \text{for all } t \end{aligned} \quad 1.4$$

The boundary conditions reflect the equilibrium state in the imaging plane before saturation, and the perfect saturation inside the labeling plane. This system can be solved analytically for  $m$  and gives [1.5]

$$\begin{aligned} m(x, y, z, t) &= \frac{1}{2} * \operatorname{erfc}\left(\frac{z - v(x, y) * t}{2 * \sqrt{Dt}}\right) + \frac{1}{2} * \exp\left(\frac{v(x, y) * z}{D}\right) * \operatorname{erfc}\left(\frac{z + v(x, y) * t}{2 * \sqrt{Dt}}\right) \\ \text{with } \operatorname{erfc}(x) &= \frac{2}{\sqrt{\pi}} * \int_x^{\infty} \exp(-t^2) dt \end{aligned} \quad 1.5$$

The signal enhancement after saturation  $E(x,y,z,t=T_{SAT})$  can be calculated according to equation [1.2], knowing the blood velocity, diffusion coefficient, saturation period and thickness, and the imaging plane thickness. **Figure 1.7** shows a 70 % signal increase for a particular set of acquisition parameters ( $L_{SAT}/L_{IMG} = 0.4/10$  mm,  $T_{SAT} = 330$  ms) and assuming a uniform diffusion coefficient  $D = 3 \mu m^2/ms$ . It is worth noting that the enhancement  $E(v=0)$  found in absence of flow matches the DESIRE signal enhancement found with the same imaging parameters. One will also notice that the enhancement reaches a plateau on the  $E/v$  plot for velocities higher than  $v_P = 15$  mm/s. Above this threshold, the spins labeled at the beginning of the saturation module exit the imaging plane before the end of the labeling module. Therefore they do not contribute to the signal. Both the maximum enhancement and the velocity threshold depend strongly on the different imaging parameters, making FENSI potentially sensitive to a wide range of velocities.

To synthesize, in the absence of  $T_1$  relaxation effects, the signal enhancement  $E/v$  is fully characterized by three different parameters:  $v_{MIN}$ ,  $v_P$  and  $E_{MAX}$ . These parameters depend entirely on  $L_{IMG}$ ,  $L_{PS}$ ,  $T_{SAT}$  and  $L_{SAT}$  and will be further detailed later in this manuscript. The following lines illustrate the relationship between the FENSI enhancement  $E$  and the velocity  $V$ .

$$\begin{aligned} V < V_{MIN} & & E &= 0 \\ V_{MIN} < V < V_P & & E &= \frac{T_{SAT}}{L_{SAT}} * (V - V_{MIN}) \\ V_P < V & & E &= E_{MAX} \end{aligned}$$

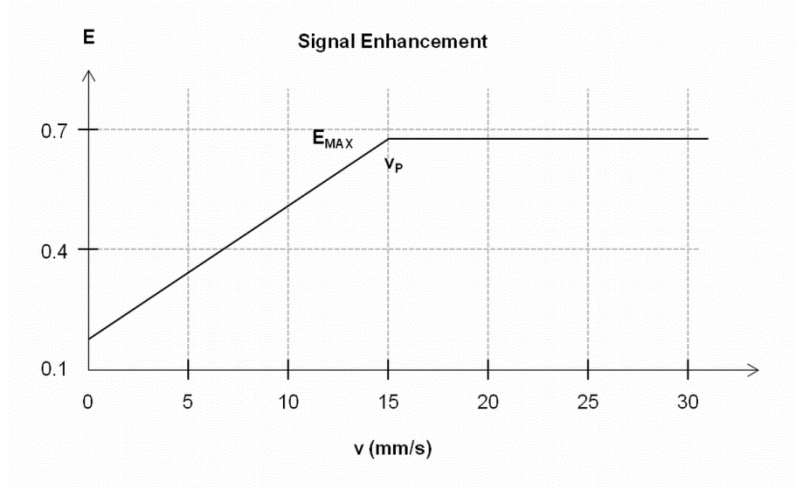


**Figure 1.7 E/v plot: theoretical signal enhancement obtained with FENSI for different blood velocities.** For estimation, we used the following parameters:  $L_{SAT}/L_{IMG} = 0.4/10$  mm,  $D = 3 \mu\text{m}^2/\text{ms}$ ,  $T_{SAT} = 330$  ms.

It is worth noting that the existence of a plateau  $E_{MAX}$  in the E/v plot (**Figure 1.7**) does not mean that all the spins equally contribute to the signal loss. The experimental FENSI enhancement  $E_{EXP}$  is in practice weighted by the flowing spins fraction  $f$  (proportional to the regional CBV). This last parameter can increase substantially near large blood vessels and varies locally in patients suffering from cerebrovascular diseases, such as brain tumors.

This also indicates that the FENSI method can be used in different ways. If the plateau  $E=E_{MAX}$  is reached instantaneously, all the spins with velocities  $v > v_P$  equally contribute to the FENSI enhancement. Because the signal intensity difference between the control and tag image reflects the number of flowing spins through the labeling slice, any difference in the flux-weighted image will be due to differences in the local flowing spins fraction.

### *Flux calculation*

As opposed to the theoretical calculation performed in the previous paragraph, it is also possible to estimate the spins velocity based on the experimental signal enhancement obtained with FENSI. This was first shown by Sutton and Ciobanu (personal communication) who imaged in 2008 a flow phantom. Using the imaging parameters previously described, they calculated a velocity of 8.5 mm/s in the phantom, in good agreement with the physical input of 10 mm/s flow rate.

Their calculation is however only accurate if the flow is oriented orthogonal to the labeling plane. When performing *in vivo* experiments, one will therefore prefer to measure the local blood flux rather than estimate the longitudinal component of the blood velocity. The calculation of the volumetric flow rate of blood can be performed on the same phantom on a voxel-by-voxel basis using equation [1.6].

$$CBFlux = \left\{ \frac{I_{FLUX}}{I_{STATIC}} \right\} \times \frac{\lambda}{\alpha} \times \frac{V_{TAG}}{S_{CS}} \times \frac{60}{T_{SAT}} \times \exp\left(\frac{T_{SAT}}{T_{1b}}\right) \times \exp\left(\frac{TE}{T_{2b}}\right) \quad 1.6$$

$I_{FLUX}$  and  $I_{STATIC}$  represent the signal intensity difference due to blood flow and the static tissue signal,  $\lambda$  is the tissue-blood partition coefficient,  $V_{TAG}$  and  $S_{CS}$  the volume and the cross section of an imaging voxel,  $\alpha$  the labeling efficiency,  $TE$  the echo time and  $T_{SAT}$  the total saturation time.  $T_{1b}$  and  $T_{2b}$  are the blood longitudinal and transverse relaxation times, respectively. In this manuscript we consider equation [1.6] as standard for flux calculation.

In practice, one assumes  $T_{1b}$  and  $T_{2b}$  large enough compared to  $T_{SAT}$  and  $TE$ , respectively. In addition, the labeling efficiency is also often considered ideal ( $\alpha=1$ ) to minimize post-processing. Under these assumptions, the equation [1.6] simplifies to [1.7]

$$CBFlux = \left\{ \frac{I_{FLUX}}{I_{STATIC}} \right\} \times \lambda \times \frac{V_{TAG}}{S_{CS}} \times \frac{60}{T_{SAT}} \quad 1.7$$

Given the particular imaging parameters of Sutton et al., equation [1.7] becomes [1.8]

$$Q = \left\{ \frac{M_1 - M_{30}}{M_1} \right\} \times \lambda \times \frac{V_{IMG} - V_{TAG}}{S_{CS}} \times \frac{60}{T_{SAT}} \quad 1.8$$

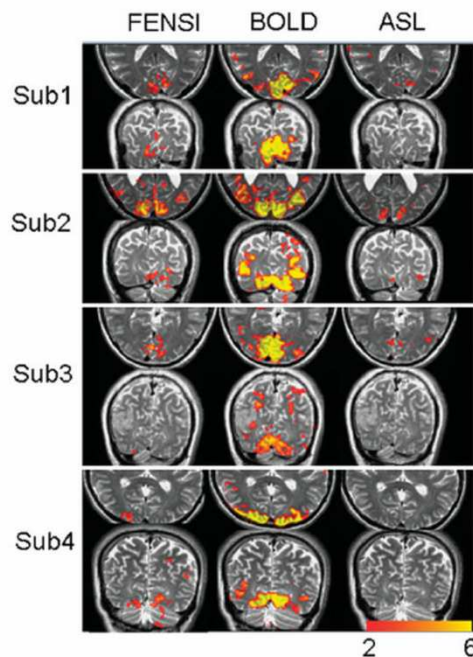
where  $M_1$  and  $M_{30}$  represent the intensity of the “control” and “tag” images (respectively acquired after 1 and 30 saturation pulses). Equation [1.8] was verified on the same water phantom. A good correlation was found between the experimental volumetric flow rate  $Q$  of  $2.8 \pm 0.6$  ml/min/cm<sup>2</sup> calculated with [1.8] and the preset rate of 3.0 ml/min/cm<sup>2</sup>.

### *FENSI: state of the art*

The FENSI technique was first introduced in 2007 as a qualitative functional imaging method. The relationships [1.2] and [1.5] between the signal enhancement and blood velocity were derived and the method was used to measure relative changes of blood flux in the human brain performing a visual task (1). The experiment showed neural activation based on FENSI, ASL and BOLD techniques (**Figure 1.8**). Out of 8 functional experiments (four subjects and two orientations), 4 presented no significant changes with ASL.

Both FENSI and BOLD were reliable in detecting neural activity during each stimulus, and measured in average +6.9 % blood flux and +1.6 %  $T_2^*$  weighted signal during the visual task. This first study, although performed on a limited number of subjects, showed the potential important impact of FENSI in fMRI studies.

**Figure 1.8 Z-score axial and coronal activation maps** derived from FENSI, BOLD and ASL acquisitions in four subjects performing a visual task (from *Functional Imaging with FENSI: Flow-Enhanced Signal Intensity by Sutton et al. (1)*). Note that ASL does not detect any significant change ( $Z < 2$ ,  $p > 0.05$ ) under visual stimulus for subject #4, suggesting lower sensitivity compared to FENSI or BOLD. Under stimulation, the signal increased in average by 6.9 %, 1.6 % and 1.2 % with FENSI, BOLD and ASL, respectively (1).



More recently, FENSI was used with the exact same imaging parameters to estimate cerebral blood flow in the hippocampal and brainstem region, and investigate the possible correlations between CBF, aging, reaction time and cognitive decline (74). Although claiming CBF quantification, the study was really measuring blood flux and assumed negligible side-effects due to repeated saturation, leading to possible overestimation of flux. Absolute quantification was of little importance, as only relative changes (between two regions and two populations of subject) were used in their calculations. However, the fact that CBF was maybe non-uniformly affected by MT effects might have biased the authors' statistics.

## II. Quantification of blood flux with FENSI

In this chapter we investigate the possibility to quantify blood flux *in vivo* with FENSI. For this purpose, we estimate the amount of magnetization transfer (MT) introduced by the repeated saturation described in chapter 1. Measured on samples without flow, MT causes a decrease in the signal intensity of the tag image which will lead to an overestimation of the flux.

After we estimate the amount of magnetization transfer introduced when performing FENSI *ex vivo* (on sacrificed rats), we perform a post-processing correction for MT in order to calculate the first MT-free *in vivo* cerebral blood flux maps of the rat brain. These results, published in 2011 (75) in Magnetic Resonance in Medicine, show that MT can be efficiently removed from FENSI data. The CBFlux results calculated in gray and white matter are in good agreement with the literature on rat brain perfusion.

However, the MT effects depend on the many parameters of the saturation module. They are also tissue dependent. The post-correcting method is therefore not suitable for *in vivo* studies and characterization of microvascular changes associated with brain pathologies.

In the second part of this chapter we show how the design of the Flow Enhanced Signal Intensity method was modified in order to introduce the exact same amount of MT in the control and the tag image. Experiments on phantoms and *ex vivo* samples show that the remaining MT effects are negligible compared to flux. We provide with FENSI quantitative cerebral blood flux measurements of the rat brain at 7 Tesla. Based on the new sequence design, the FENSI method is suitable for a completely non-invasive and quantitative characterization of the brain microvasculature.

Finally we discuss the validity of our flux measurements and compare the approach that we used to quantify blood flux to that of another group that implemented the MT-balanced FENSI technique on a clinical scanner. Both specificities are detailed. Quantitative comparison of CBFlux with ASL-based CBF measurements is performed and discussed.

## II.1 Magnetization transfer

We will first introduce in this section the mechanisms of MT and the effect this phenomenon has on signal intensity after application of the FENSI preparation module used to repeatedly label the flowing spins. Then we will propose and apply a protocol to precisely quantify the amount of MT introduced by our sequence in a typical FENSI CBFlux measurement experiment at 7 Tesla.

### *Introduction*

First observed in 1989, MT refers to the following phenomenon: due to an exchange of spins between free water and macromolecules, an off-resonance irradiation applied in tissues generates a decrease in the bulk water signal observed in MRI. For a given off-frequency pulse, the water signal decay depends on the exchange rate between the different spins population. Therefore MT can be used to identify local structures as well as tissue alteration and degradation.

The mechanisms under MT have first been studied by Wolff and Balaban (76) after an accidental discovery (77), then quickly quantified by Henkelman et al. (62) and applied to the clinic (78-80) in the early 90's. MT is nowadays used as a natural source of contrast between tissues, along with proton density, transverse and longitudinal relaxation times.

**Figure 2.1** illustrates the MT effects introduced by a saturation pulse applied a few ppm away from the water peak, in a simple model with two pools of protons, in free water and macromolecules. We will refer to these populations as free protons and bound protons, respectively.

A radio-frequency irradiation at off resonance frequency leaves the longitudinal magnetization of the free protons unchanged. Because the bound protons are strongly coupled to each other, they present a much broader and homogeneous radio-frequency absorption lineshape than the free protons (**Figure 2.1-A**). Therefore the application of the off resonance  $B_1$  magnetic field results in a progressive saturation of the bound protons.

The bound and free protons interact with each other (**Figure 2.1-B**).  $R$  represents the MT exchange rate between the two populations of spins.  $M_z^w$  and  $M_z^m$  represent the total normalized longitudinal magnetization of the spins from the free water and the macromolecules pool respectively. Immediately after saturation and assuming very little direct saturation of the free protons,  $M_z^m \sim 0$  and  $M_z^w \sim 1$ . The two pools of protons are coupled through the Bloch

equations describing their evolution (62). These introduce the spin exchange rates  $R^*M_z^w$  (free water to macromolecules) and  $R^*M_z^m$  (macromolecules to free water).

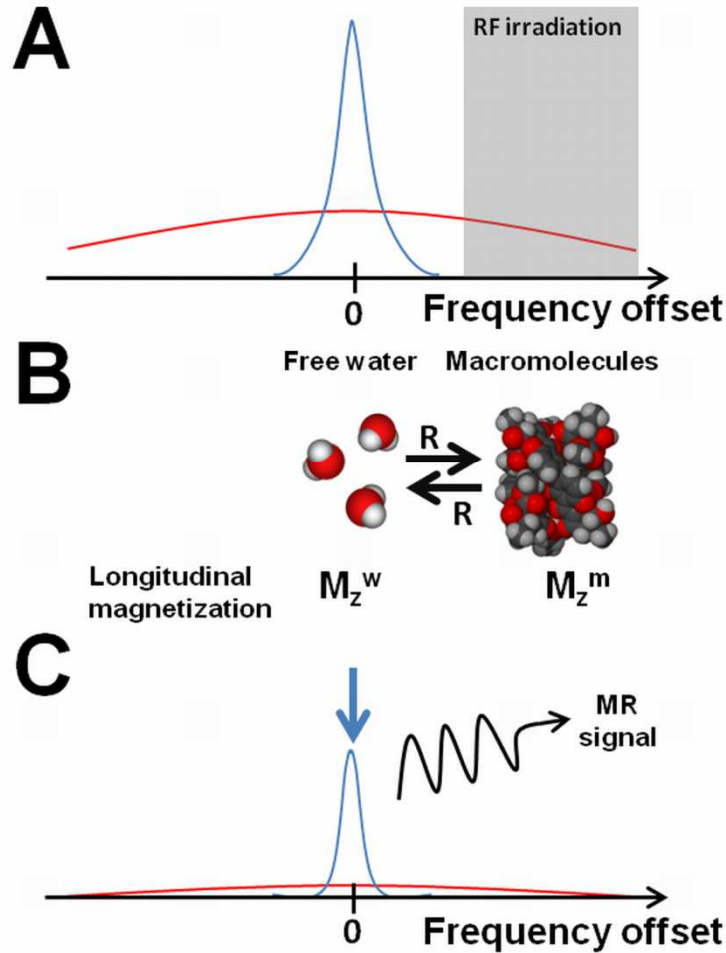


**Figure 2.1 Mechanism of magnetization transfer** **A.** Radio-frequency absorption lineshapes of free protons (blue) and bound protons (red). The application of a pulse at off-resonant frequency (grey band) affects only the longitudinal magnetization of the bound protons. **B.** Bound and free protons interact during and after radio-frequency irradiation with exchange rate  $R$ . The magnetization is partially transferred from the free protons ( $M_z^w$ ) to the bound protons ( $M_z^m$ ). **C.** The MR signal is proportional to the longitudinal magnetization of the free protons. MT generates a decrease in MR signal due to indirect saturation of the bulk water signal.

The purpose of this introduction to MT is not to solve for these Bloch equations (whose analytical solution is known (62)), but to explain the origin of the decrease in MR signal. After saturation,  $M_z^m \ll M_z^w$  and spins are mainly transferred from the free water pool to the macromolecules pool.



This generates a decrease in the longitudinal magnetization of the free protons. It is worth noting that the bound protons present an extremely short transverse relaxation time  $T_2$  (in the order of microseconds (62)). In a typical MRI experiment (with a TE on the orders of 10 ms), the MR signal decay is proportional to  $\exp(-TE/T_2)$ . Therefore no signal is acquired from the bound protons. Only the indirect saturation of the free protons due to magnetization transfer can be measured and quantified (**Figure 2.1-C**).

### *Flux over-estimation*

Magnetization transfer affects FENSI as well as most of the ASL techniques. The saturation pulse used to label the water molecules in the blood is indeed seen as an off-resonance pulse by the spins contributing to the imaging slice signal. Therefore the longitudinal magnetization of the spins is decreased in the tag image. However, the signal from the control image (without saturation) is not subject to this phenomenon.

The calculation of the theoretical cerebral blood flux crossing the saturation slice with FENSI depends on the signal intensity difference between the control and the tag image in absence of MT. In reality the decrease in signal observed when saturating spins with FENSI is also sensitive to indirect saturation of the imaging slice because the MT effects are not balanced between control and tag.

FENSI is ideally only sensitive to the moving spins crossing the saturation plane (see Chapter 1). These represent typically 1 to 5 % of the total population of spins in that plane. On the other hand, MT can affect a large part of the spin population of the imaging slice, which is by definition much thicker than the saturation plane. A more precise quantification of the MT effects introduced by the FENSI module will follow.

The following experiment highlights the MT effects introduced after application of the FENSI preparation module. Two phantoms (samples) were made of pure water and 2 % weighted agarose gel, respectively (**Figure 2.2-A**). The theoretical signal intensity difference between control and tag is zero in these two phantoms, in absence of flux and MT effects.

The effective signal intensity difference reaches 30 % of the control image intensity inside the gel (**Figure 2.2-B**). The intensity difference in water is used here as a reference, because pure water is not affected by MT. This experiment provides evidence of the MT effects introduced by repeated saturation.

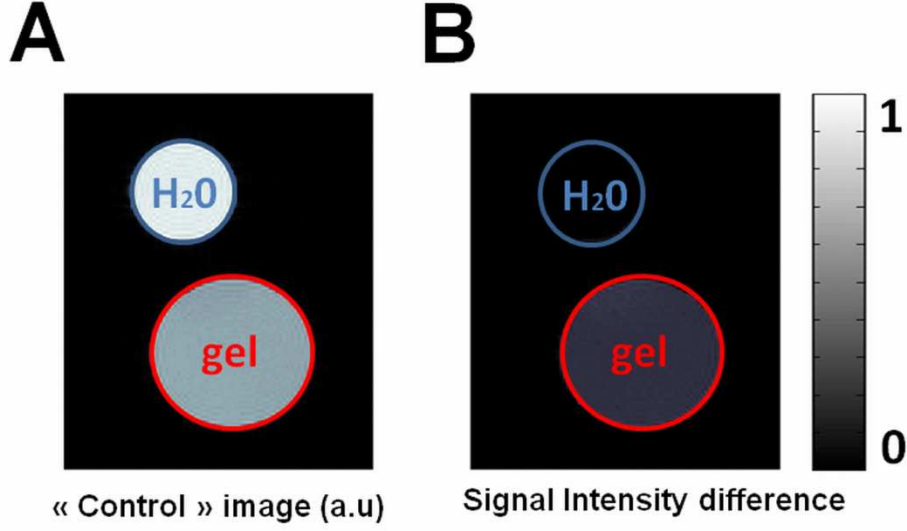


**Figure 2.2 Evidence of magnetization transfer effects on signal intensity difference obtained on phantoms with FENSI.** **A.** Localization of pure water (blue ROI) and 2 % weighted agarose phantom (red ROI) on FENSI control image (arbitrary units). **B.** Signal intensity difference between control and tag image normalized to control gel intensity, in absence of flux. Pure water is not affected by MT. The apparent difference in intensity observed in gel (30 %) is due to MT only.

#### MT quantification

To quantify this MT effect we introduce the Magnetization Transfer Ratio (MTR) defined by equation [2.1], where  $M_0$  and  $M_{SAT}$  represent the longitudinal magnetization of the free protons at equilibrium and after radio-frequency irradiation and MT respectively.

$$MTR = \frac{M_0 - M_{SAT}}{M_0} \quad 2.1$$

This MTR takes into account two different phenomena: MT and direct saturation of the free protons. This ratio can be experimentally measured by calculating the ratio of the MR signal intensity with and without saturation. In absence of flux and direct saturation, an accurate estimation of the amount of MT introduced by the FENSI preparation module is then given by equation [2.2]

$$MTR_{FENSI} = \frac{I_{CTRL} - I_{TAG}}{I_{CTRL}} \quad 2.2$$

**Figure 2.3-B** illustrates the design of the  $MTR_{FENSI}$  measurement protocol. Compared to a classical FENSI experiment (**Figure 2.3-A**), the pulse sequence is slightly modified to tag a 300  $\mu\text{m}$  thick slice 1 mm away (to avoid direct saturation effects) from the imaging slice, chosen to be 1 mm thick. Imaging is performed on both sides of the saturation plane.

In order to estimate the MT introduced by FENSI in the rat brain in absence of flow, five animals are euthanized right before the  $MTR_{FENSI}$  measurements. One animal is used to study the influence of the total saturation duration (proportional to the number of pulses) on the amount of MT generated. Four rats are used to estimate the possibility to quantify the effect of MT in gray matter (GM) and white matter (WM), and to generate  $MTR_{FENSI}$  maps of the rat brain.

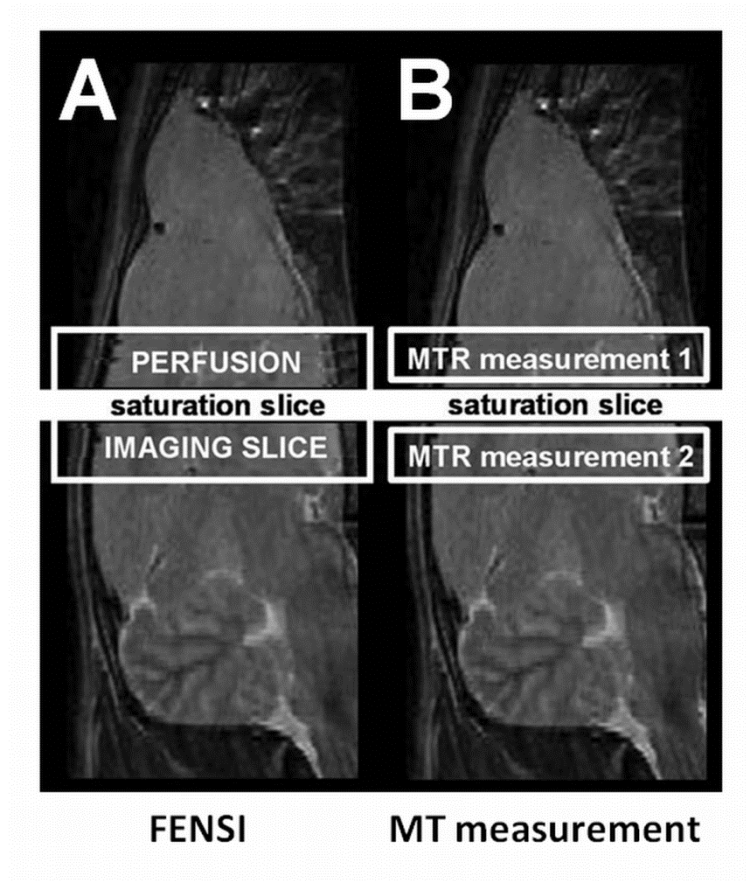


**Figure 2.3 Design of the FENSI /  $MTR_{FENSI}$  measurement imaging protocol**

**A.** In a typical FENSI experiment, the capillary network is being continuously saturated. Imaging of a thicker imaging slice provides information on all the spins that have crossed the saturation slice but is also contaminated by MT effects. **B.** The MR signal is being measured above and below the saturation slice (no direct saturation) on a sacrificed rat to estimate the amount of MT introduced by the repeated saturation.

The parameters of the FENSI preparation module are chosen similar to those used for in vivo studies. Only the total duration of the saturation varies from 250 ms to 1500 ms along the experiment. **Figure 2.4-A** presents plots of the MTR versus the number of saturation pulses for white and gray matter, averaged on four slices at 7 Tesla. The different ROI used for brain segmentation are shown in **Figure 2.4-B**.

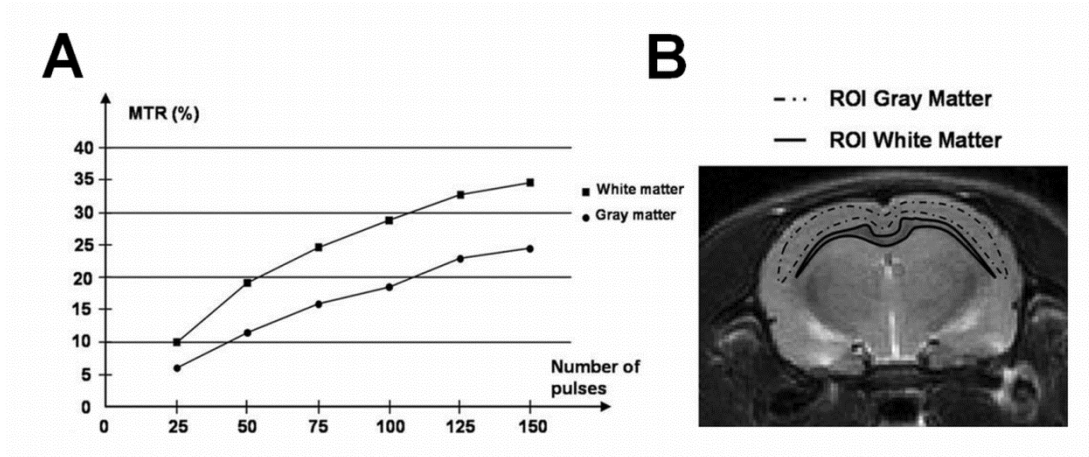


**Figure 2.4 Quantification of MTR<sub>FENSI</sub> in gray and white matter at 7 T**  
**A.** Evolution of MTR<sub>FENSI</sub> as a function of the number of pulses used for saturation. The MTR reaches up to 35 % in white matter and 24 % in gray matter, for 150 saturation pulses (saturation duration = 1500 ms). **B.** Regions of Interest used to calculate MTR<sub>FENSI</sub> in white and gray matter (corpus callosum/cerebral cortex). The corresponding number of pixels was 156 and 500, respectively. The saturation was located below the imaging slice.

One can see that, as expected, the MT effect is dependent on the tissue type and gets stronger as the number of pulses increases. For a 1500 ms saturation period, the MT effect accounts for a decrease in signal intensity of up to 35 % in WM and 24 % in GM, respectively.

In order to estimate the variability of the MTR<sub>FENSI</sub> ratio across animals the MT measurements are repeated on four different animals (4 slices, using the same saturation period of 1500 ms). The results from these measurements are presented in **Table 1**. The decrease in signal due to the MT effect found in WM/GM is  $[34.1 \pm 3.9 \%]/[23.9 \pm 3.3 \%]$  when the tagging plane is placed below the imaging slice and  $[40.9 \pm 4.1 \%]/[29.0 \pm 3.4 \%]$  when the tagging plane is placed above. No significant difference is observed among the slices taken for the same individual or for different individuals.

**Table 1 MTR (%) in white and gray matter introduced by the FENSI tag**

<b>MTR<sub>FENSI</sub> [%]</b>	<b>Rat1</b>	<b>Rat2</b>	<b>Rat3</b>	<b>Rat4</b>	<b>mean</b>
white matter <sup>a</sup>	41.0 ± 2.8	40.0 ± 3.2	41.1 ± 3.7	41.5 ± 3.5	40.9 ± 4.1
gray matter <sup>a</sup>	29.1 ± 3.0	28.6 ± 3.8	29.3 ± 3.3	29.1 ± 3.7	29.0 ± 3.4
white matter <sup>b</sup>	33.9 ± 3.5	35.9 ± 3.5	35.4 ± 3.7	31.3 ± 3.2	34.1 ± 3.9
gray matter <sup>b</sup>	24.5 ± 3.2	24.9 ± 2.6	24.6 ± 3.2	21.9 ± 3.2	23.9 ± 3.3

*The results are averaged over four different slices in four rats. <sup>a</sup>Tag located above the imaging slice. <sup>b</sup>Tag located below the imaging slice.*

### Conclusion

The repeated saturation used to label the flowing spins with FENSI is seen as an off resonant radio-frequency irradiation by the spins from the thicker imaging slice. This leads to an indirect saturation of the free protons due to magnetization transfer and to an overestimation of the cerebral blood flux CBFlux calculated with FENSI. However, this MT effect can be quantified once a particular set of experimental parameters was selected.

## II.2 Post-processing correction

In this section we will describe a post-processing correction protocol to correct for the effect of MT on signal intensity and derive the first non-invasive quantitative cerebral blood flux maps of the rat brain from contaminated FENSI data.

### Process

Brain microvasculature is characterized with FENSI by calculating the flux CBFlux (in units of mL/min/cm<sup>2</sup>) defined by equation [1.7] (see Chapter 1).

$$\text{CBFlux} = \left\{ \frac{I_{\text{FLUX}}}{I_{\text{STATIC}}} \right\} \times \lambda \times \frac{V_{\text{TAG}}}{S_{\text{CS}}} \times \frac{60}{T_{\text{SAT}}}$$

Under the assumption that the  $MTR_{\text{FENSI}}$  measured *ex vivo* is similar for *in vivo* studies, quantitative flow information based on FENSI images is obtained by correcting for the magnetization transfer effect present in the tag images, according to the formula [2.3], where  $I_{\text{TAG}}$  is the uncorrected signal

and  $MTR_{FENSI}$  is the average value of the mean correction factors listed in Table 1: 0.37 and 0.26 for WM and GM, respectively.

$$I_{COR} = I_{TAG} / (1 - MTR_{FENSI}) \quad 2.3$$

The intermediate parameter  $I_{COR}$  represents the corrected signal intensity after the MT correction and is equal to  $I_{TAG \text{ without MT}}$ . In the absence of MT effects or direct saturation, only flux and static tissue affect the signal intensity of the tag image.  $I_{TAG \text{ without MT}}$  can therefore also be defined by equation [2.4]

$$I_{TAG \text{ without MT}} = I_{CTRL} - I_{STATIC} - I_{FLUX} \quad 2.4$$

Cerebral blood flux CBFlux can then be calculated using equation [2.5], by eliminating  $I_{FLUX}$  in the original flux formula [1.6] based on equation [2.4].

$$CBFlux = \left\{ \frac{I_{CTRL} - I_{COR}}{I_{STATIC}} - 1 \right\} \times \lambda \times \frac{V_{TAG}}{S_{CS}} \times \frac{60}{T_{SAT}} \quad 2.5$$

### *First quantitative cerebral blood flux maps*

We calculate the CBFlux maps of ten animals, with and without MT correction. For perfusion measurements each dataset consists of three images: a control image (3 mm thick without saturation), a tag image (3 mm thick with saturation) and a reference image.

The experimental parameters for this particular experiment are listed in **Table 2**. In particular, the effective tagging thickness (0.4 mm) is measured by acquiring MR signal from a slice orthogonal to the saturation plane. Repeated saturation of the magnetization of the spins inside a 0.3 mm thin slice is found to be equivalent to an instantaneous saturation of a 0.4 mm slice. Therefore the thickness of the reference image is chosen 0.4 mm to account for static tissue signal and direct saturation of tissues.

Segmentation of WM and GM regions is performed using an additional T<sub>2</sub>-weighted Fast SE sequence (TE = 60 ms, TR = 3000 ms, NA = 4, Rare Factor 8, FOV 30 x 30 mm<sup>2</sup>). **Figure 2.5-A** illustrates the  $MTR_{FENSI}$  masks generated to perform a pixel-by-pixel post-processing correction for MT. These masks are found to agree well with the corresponding regions as seen in a typical MTR map (**Figure 2.5-B**).

**Table 2 List of experimental parameters used for calculation of cerebral blood flux with FENSI at 7 Tesla**

FENSI-SE at 7 Tesla	CONTROL	TAG	REFERENCE
TR/TE (ms)		3000/8.3	
In-plane resolution (mm)		0.2 x 0.2	
Field of View (mm)		30 x 30	
Slice thickness (mm)	3	3	0.4
FENSI module	OFF	ON	OFF
Tag thickness (mm)	-	0.3	-
Number of 90° loops	-	150	-
Saturation time <sup>1</sup> (ms)	0	1500	0

A FENSI preparation module is implemented in front of a regular Spin-Echo sequence (with Cartesian encoding) to prepare the magnetization of the spins in the tag image. <sup>1</sup>For Control and Reference image, a delay accounts for the increase of the repetition time due to the tagging module.

As expected, the CBFlux maps calculated without MT correction do not give accurate results. Indeed, the uncorrected maps (**Figure 2.6**) behave like MTR maps (see **Figure 2.5-B**) with hyper-intense signals in the WM, blood flux value of  $3.8 \pm 0.4$  mL/min/cm<sup>2</sup>, compared with  $3.1 \pm 0.3$  mL/min/cm<sup>2</sup> in GM.

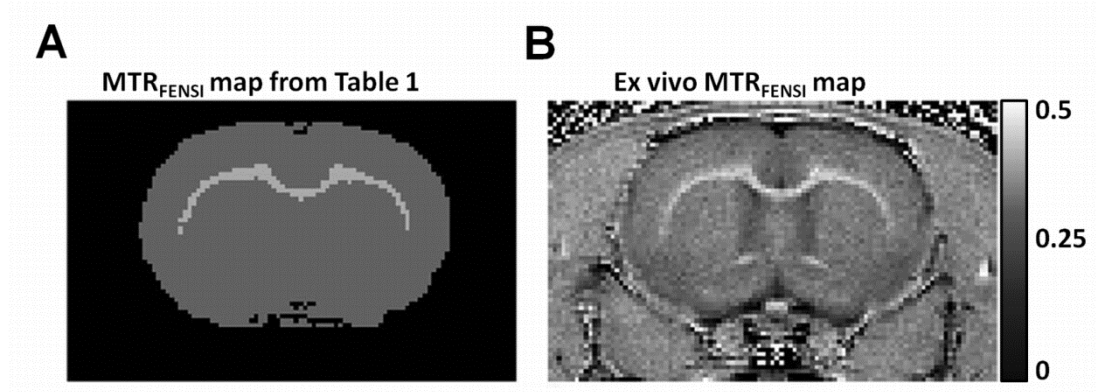


**Figure 2.5 MTR<sub>FENSI</sub> map A.** generated from **Table 1** and used for post-processing. **B.** acquired on an ex vivo rat brain.

However, the corrected maps (**Figure 2.6-B**) yield results which agree with those previously reported in the literature. Specifically, we obtain blood flux values of  $0.30 \pm 0.35/0.74 \pm 0.32$  mL/min/cm<sup>2</sup> in WM/GM, resulting in a ratio WM/GM of 0.4, in good agreement, as illustrated in **Table 3**, with the CBF ratio of obtained with other techniques such as ASL (81), DSC (82), positron emission tomography (82-83) or CT (84). Direct comparison between the measurements made with FENSI and those made with other perfusion

techniques such as ASL and DSC is complicated by the fact that ASL and DSC measure different aspects of blood flow; specifically, ASL and DSC measure bulk delivery of blood in mL/100g of tissue/min while FENSI measures localized volumetric blood flux in units of mL/min/cm<sup>2</sup>. This aspect will be further discussed later in this manuscript.

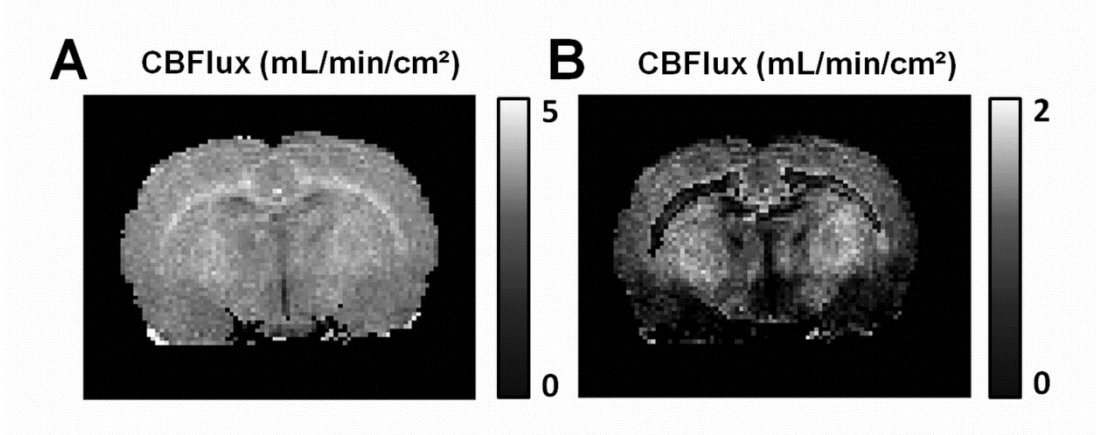


**Figure 2.6 Cerebral blood flux maps calculated with FENSI** **A.** *without MT correction. WM regions appear hyper-perfused compared to GM. This is in contradiction with literature on brain microvasculature.* **B.** *After post-processing correction for MT, the overall blood flux is lower in the rat brain. The WM/GM flux ratio (0.41) is consistent with the WM/GM CBF ratio obtained with ASL//DSC (0.33//0.37) studies (81-82).*

**Table 3 Comparison of the FENSI flux ratio WM/GM with the CBF ratio obtained with other methods**

Method	PET	CT	DSC	ASL	FENSI
<b>Flux or CBF ratio</b>	0.45	0.30	0.37	0.33	0.41

*The flux ratio obtained with FENSI is in agreement with literature on brain perfusion (see refs in text). Specifically, Regions of Interest are drawn in the cerebral cortex for GM and in the corpus callosum for WM (see **Figure 2.4-B**).*

The results presented here are the first in vivo MT free CBFlux measurements obtained with FENSI. They demonstrate the feasibility of complete and non-invasive quantification of microvascular flux dynamics with our method.



### Accuracy of the MT modelization

The question of whether the MT correction is accurate is to be assessed in this section. The  $MTR_{FENSI}$  is indeed measured *ex vivo* (in absence of flow), and the model used for flux calculation assumes that this  $MTR_{FENSI}$  is similar *in vivo*, and affects the components  $I_{CTRL}$ ,  $I_{STATIC}$  and  $I_{FLUX}$  of the theoretical tag signal intensity  $I_{TAG}$  without MT.

However, the effect of MT on flowing blood is not clear and one could consider a model where MT only applies to the static spins of the imaging slice that are not already subject to direct saturation. In this model, the measured tag signal intensity  $I_{TAG,2}$  is defined by equation [2.6]

$$I_{TAG,2} = I_{CTRL} - I_{STATIC} - MTR \times (I_{CTRL} - I_{STATIC}) - I_{FLUX} \quad 2.6$$

Under this assumption, the CBFlux used to characterize brain microvasculature according to [1.6] becomes [2.7]

$$CBFlux = (1 - MTR_{FENSI}) \times \left\{ \frac{I_{CTRL} - I_{COR}}{I_{STATIC}} - 1 \right\} \times \lambda \times \frac{V_{TAG}}{S_{CS}} \times \frac{60}{T_{SAT}} \quad 2.7$$

The WM/GM flux ratio of 0.35 based on this equation is within acceptable range compared to other CBF measurement techniques (see **Table 2.3**) and close to the flux ratio of 0.41 derived with the previous model.

Only the amount of MT relative to the flowing spins (1 to 5 % of the total number of spins) is treated differently in these two approaches. Therefore these two models still provide a first-order correction for the MT introduced by the FENSI preparation module. In reality, the  $MTR_{FENSI}$  relative to the fraction of moving spins is probably different from the  $MTR_{FENSI}$  calculated in WM or in GM, and a more complex model needs to be established in order to fully compensate for MT.

### Limitations

As illustrated by **Figure 2.4**, the  $MTR_{FENSI}$  depends on the total saturation duration. Any change of parameters on the preparation module (number of pulses, power, shape, duration) will affect the amount of MT introduced by the saturation on the tag image.

Even though the exchange rate between the macromolecular spins and the liquid pool is field independent the MTR for a tissue increases as the field strength increases due to the increase in the longitudinal relaxation time (77). Therefore, for identical FENSI modules the  $MTR_{FENSI}$  will be different at

different field strengths. As a result, the correction factor cannot be transferred from one magnetic field strength to another and should be measured in each particular case.

The main limitation associated to MT remains its variability upon different type of tissue. It is only possible to perform non-invasive quantification of the CBFlux in the WM/GM of ten healthy rats after estimation of the  $MTR_{FENSI}$  in the WM/GM on four sacrificed rats. This post-processing correction method requires a priori knowledge on the tissue. This information depends on the many parameters used in the FENSI preparation module and must be obtained on the same tissue in absence of flux or *ex vivo*.

### *Conclusion*

For the first time and based on the post-processing correction technique presented in this section, FENSI is used to perform non-invasive quantification of CBFlux in the WM and GM of the rat brain. The results obtained with this method (relative measures of CBFlux in gray and white matter) are in good agreement with the literature on rat brain perfusion, measuring CBF.

However, in regards to the limitations of this approach, this post-processing correction should only be used in situations in which the magnetization transfer is not expected to change. It is therefore not applicable to longitudinal studies in which the MTR ratio changes (e.g. angiogenesis) or clinical studies. For these situations, other correction techniques are needed.

## **II.3 MT correction within the preparation module**

In this section we will describe our developments toward another method to compensate for the MT introduced by the tag when performing FENSI, by introducing the exact same amount of MT in the control image. This technique is now used as standard for *in vivo* studies to calculate MT free flux with FENSI.

### *Pulse sequence modification*

The preparation module of the original FENSI method consists in several loops of 90° FA short pulses. The repetition of these short pulses is equivalent with a continuous saturation over a long duration and introduces

MT in the tag image. When set in control mode, the preparation module does not apply any radio-frequency pulse. Therefore no MT is introduced in the control image and the signal intensity difference between control and tag is contaminated by MT.

The FENSI preparation module is modified based on a Transfer Insensitive Labeling Technique (TILT) method (50) in order to compensate for MT effects during the acquisition.

For this purpose, the  $90^\circ$  FA pulses used in the previous FENSI sequence are replaced by pairs of  $+45^\circ+45^\circ//+45^\circ-45^\circ$  FA pulses (tag//control). In practice, every other  $45^\circ$  FA pulse of the control image is subject to a  $+\pi$  phase shift. A particular attention is given to the delay between two consecutive  $\pm 45^\circ$  FA pulses. This delay must be chosen as short as possible in order to refocus the same population of spins in the control image and to fully saturate the labeling plane in the tag image. This delay is only constrained by the gradient duty cycles.

Based on this new design, pseudo-continuous saturation of the labeling plane is achieved in the tag image, whereas the spins are regularly refocused in the control image.

Due to the application of radio-frequency pulses in the control preparation module, both control and tag image are affected by MT. However, the  $MTR_{FENSI}$  depends on the number, power, shape and duration of the pulses used in the preparation module and these parameters are identical for control and tag. Therefore the same amount of MT affects  $I_{CTRL}$  and  $I_{TAG}$ .

The FENSI pulse sequence is further modified in order to implement an additional triple- $90^\circ$ -pulse saturation module. The repeated application of  $+45^\circ$  and  $-45^\circ$  FA pulses in the control image can indeed generate a decrease of the static tissue signal in case of imperfect slice profile. We remove the contribution of the static tissue to the MR signal of both control and tag image by using this module.

After complete modification of the FENSI pulse sequence modification, the difference in signal intensity measured between control and tag can only depend on flux. Equation [2.4] becomes [2.8]:

$$I_{TAG} = I_{CTRL} - I_{FLUX} \quad 2.8$$

We can then derive the cerebral blood flux CBFlux (in mL/min/cm<sup>2</sup>) from the data acquired using the modified FENSI sequence by using the formula [2.9]:

$$CBFlux = \left\{ \frac{I_{CTRL} - I_{TAG}}{I_{STATIC}} \right\} \times \lambda \times \frac{V_{TAG}}{S_{CS}} \times \frac{60}{T_{SAT}} \quad 2.9$$

### Experimental removal of MT effects

Phantom (2 % agar gel) experiments are performed in order to verify the removal of MT effects between control and tag. An additional test is also performed on a postmortem rat brain. The  $MTR_{FENSI}$  is calculated voxel-by-voxel based on equation [2.2].

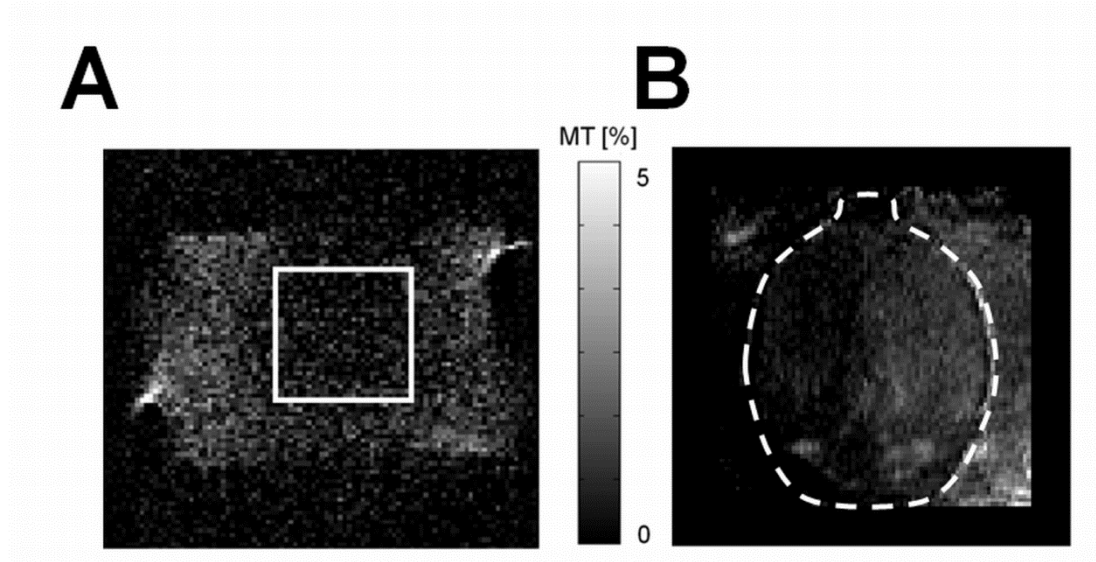


**Figure 2.7 Influence of MT effects on A. gel (2 % weighted agar) and B. post mortem rat brain. A.** The  $MTR_{FENSI}$  in gel reaches 4 % on the edges of the sample, and remains below noise level ( $0.1 \pm 0.3$  %) inside the ROI used for shimming (white box). **B.** The  $MTR_{FENSI}$  does not exceed 2.2 % in the whole *ex vivo* rat brain (white dashed line, axial view) and is negligible in the cerebral cortex ( $0.7 \pm 0.8$  %).

**Figure 2.7-A** illustrates the  $MTR_{FENSI}$  introduced on the gel sample by this new pulse sequence. The white box indicates the ROI in which the shimming was performed. The  $MTR_{FENSI}$  inside the shimmed ROI is negligible ( $0.11 \pm 0.26$  %), while at the edges of the sample can reach 4 %. This result establishes that provided good  $B_0$  homogeneity, the current FENSI implementation eliminates MT effects allowing quantitative measurements of CBFlux without post-processing correction.

Although the  $MTR_{FENSI}$  is found less homogeneous in the *ex vivo* rat brain than in phantoms, MT effects are also negligible on the post-mortem rat brain (**Figure 2.7-B**). Based on the flux map obtained on the post-mortem brain, a remaining  $MTR_{FENSI}$  of  $0.7 \pm 0.8$  % is calculated in the cortex. The  $MTR_{FENSI}$  can reach 2.2 % near cerebellar regions.

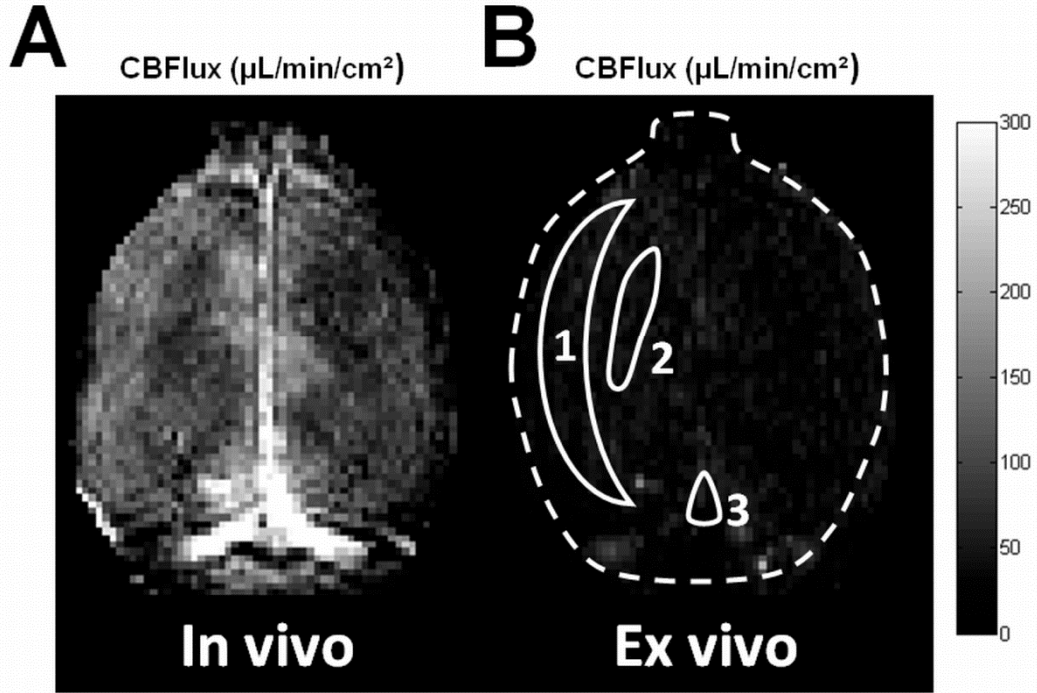


**Figure 2.8 CBFlux map ( $\mu\text{L}/\text{min}/\text{cm}^2$ ) calculated with MT-balanced FENSI (no post-processing).** **A.** *In vivo* flux map of a rat brain **B.** After sacrifice, the flux calculated in the same rat brain (dashed line) is negligible. The areas #1, 2 and 3 are the ROIs used to measure flux in the cerebral cortex, corpus callosum and major cerebral artery respectively.

**Figure 2.8** illustrates the influence of this  $MTR_{FENSI}$  on flux calculation. Indeed, the apparent flux calculated *ex vivo* (**Figure 2.8-B**) is not related to CBFlux, but reflects the overestimation of blood flux due to MT. The CBFlux results obtained in the cerebral cortex, corpus callosum and MCA are listed in **Table 4**. The *ex vivo* measurements in the cerebral cortex, corpus callosum and MCA show that MT has very little influence on flux calculations. The impact of MT on CBFlux is below noise level when performing an *in vivo* flux measurement with FENSI.

**Table 4** *In vivo* and *ex vivo* CBFlux calculated with FENSI in the rat brain

Cerebral blood flux ( $\mu\text{L}/\text{min}/\text{cm}^2$ )	In vivo	Ex vivo
cerebral cortex	$131 \pm 27$	$36 \pm 22$
corpus callosum	$66 \pm 17$	$28 \pm 13$
major cerebral artery	$308 \pm 121$	$25 \pm 21$

The measurements in the cerebral cortex, corpus callosum and MCA were respectively performed in the ROIs #1, 2 and 3 of **Figure 2.8-B**.

### Quantitative Cerebral Blood Flux maps at 7 Tesla

Based on the new  $45^\circ/\pm 45^\circ$  FA pulse design, the sequence is then optimized to perform *in vivo* studies at 7 Tesla in a reasonable amount of time. For this purpose, the FENSI preparation module is implemented on an Echo Planar Imaging (EPI) sequence, maximizing the SNR per unit of time. The k-space is segmented in 4 segments in order to avoid large distortions of the signal. The parameters used for flux calculation are listed in **Table 5**.

**Table 5 Parameters of the MT balanced FENSI Spin Echo EPI sequence at 7 Tesla**

FENSI-SE at 7 Tesla	CONTROL	TAG	REFERENCE
TR/TE (ms)		6000 / 13	
In-plane resolution (mm)		0.25 x 0.25	
Field Of View (mm)		20 x 20 <sup>1</sup> // 25 x 25 <sup>2</sup>	
Slice thickness (mm)	6.5	6.5	1
FENSI module	ON	ON	OFF
Tag thickness (mm)	1	1	-
Number of $+45^\circ/-45^\circ$ loops	147	0	-
Number of $+45^\circ/+45^\circ$ loops	3	150	-
Effective sat time (ms)	60	3000	-

<sup>1</sup>FOV used for coronal and sagittal orientation. <sup>2</sup>FOV specific to the axial orientation.

In order to increase the SNR, the initial imaging slice and saturation slice thicknesses (3 and 0.3 mm) are put to 6.5 and 1 mm respectively. We present in **Figure 2.9** the first *in vivo* quantitative CBFlux maps of the rat brain acquired along three orthogonal directions with these experimental parameters. Each orientation requires 75 repetitions of both control and tag image (acquisition time 60 min). The CBFlux values in the cerebral cortex, corpus callosum and striatum are respectively measured in the ROIs #1, 2 and 3 of **Figure 2.9-F**.

Cerebral Blood Flux ( $\mu\text{L}/\text{min}/\text{cm}^2$ )	cerebral cortex 150 $\pm$ 45	corpus callosum 46 $\pm$ 42	striatum 103 $\pm$ 34
---	---------------------------------	--------------------------------	--------------------------

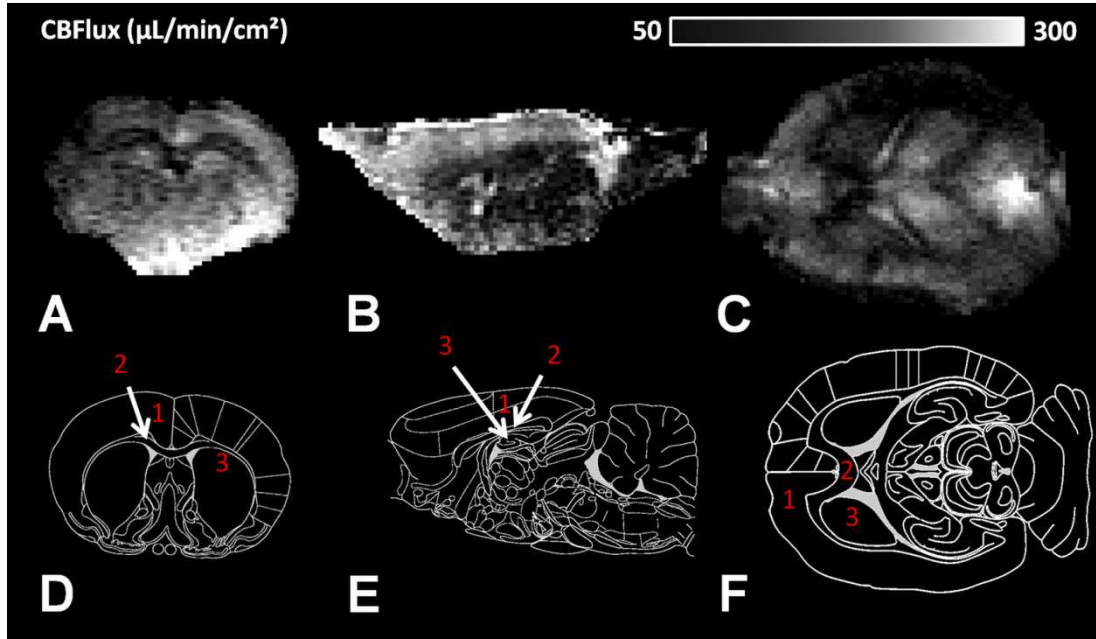


**Figure 2.9 A. coronal, B. sagittal and C. axial components of the Cerebral Blood Flux in the rat brain at 7 Tesla.** The EPI-based flux maps show little geometrical distortions compared to **D. coronal, E. sagittal** and **F. axial** views of the rat brain (The Rat Brain in stereotaxic coordinates, G. Paxinos & C. Watson, 1998). The areas 1, 2 and 3 are the ROIs used to measure blood flux in the cerebral cortex, corpus callosum and striatum respectively.

#### *Discussion and conclusion on the two correction protocols*

The CBFlux measured in the rat brain with this new method is significantly lower than the CBFlux in GM and WM obtained with the post-processing correction protocol detailed in the section of this chapter:  $740 \pm 320$  and  $304 \pm 350$   $\mu\text{L}/\text{min}/\text{cm}^2$ , respectively.

These results suggest that the post-processing protocol may not fully compensate for MT effects. The  $\text{MTR}_{\text{FENSI}}$  is indeed measured in two different 1 mm thick slices located above and below (offset  $\pm 1$  mm) the 0.3 mm thick saturation plane. As a result, the amount of MT that affects the static spins in the region  $\pm [0.15 \text{ mm} - 0.5 \text{ mm}]$  is not quantified by our model. Because MT affects the static tissues, a slight underestimation of the  $\text{MTR}_{\text{FENSI}}$  can cause a major overestimation of CBFlux (490 % in GM, 660 % in WM).

It is also possible that the newly developed technique underestimate CBFlux if the second pulse ( $-45^\circ$ ) used in the FENSI preparation module does not efficiently refocus the spins. A fraction of the flowing spins would then be labeled in both control and tag images. Such imperfections would however

affect the fastest spins first. To minimize these errors, the quality of the “tag” is checked before the beginning of the flux measurements.

As explained previously, the post-processing approach represents only a first-order correction for MT. To quantify CBFlux *in vivo*, one will prefer FENSI sequences where MT effects are fully balanced between control and tag.

The results presented in this section show that, after modification of the FENSI preparation module, the signal intensity difference between control and tag is not contaminated by MT effects anymore. Therefore flux calculation based on FENSI requires neither post processing nor *a priori* knowledge on tissue. This new FENSI method is then suitable for complete non-invasive and quantitative characterization of brain microvasculature. We will now consider this FENSI method and the imaging parameters described in this section as standard for calculation of CBFlux at 7 Tesla throughout the manuscript.

## **II.4 Discussion on CBFlux quantification**

The CBFlux quantification used in this manuscript and its potential improvements are discussed. The potential comparison of CBFlux with CBF is also considered.

### *On the removal of magnetization transfer effects*

The original FENSI technique set in tag mode introduces - via the use of repeated saturation of the labeling slice - magnetization transfer effects on the static tissue of the imaging slab. These are not compensated in the control image, resulting in a major overestimation of CBFlux due to MT. In addition, MT effects are tissue dependent and even the relative quantification of CBFlux is biased in the absence of a post-processing correction.

In this manuscript the amount of MT introduced by the tag is quantified *ex vivo* in different structures of the rat brain. A post-processing correction method is proposed to compensate for MT effects. Based on this approach, the first FENSI parametric flux maps are derived. The CBFlux ratio in white and gray matter (0.41) is consistent with that obtained in conventional perfusion MRI, PET or CT (0.30 – 0.45).

A second approach is proposed in order to balance the MT effects between the control and tag images, and calculate CBFlux without post-processing or additional knowledge on the tissues. Radio-frequency pulses are introduced in the control image and successively flip then refocus the



magnetization of the spins from 45°. In the tag image the magnetization is flipped in the transverse plane with two successive 45° FA pulses. The control/tag intensity subtraction is free from MT effects. This is verified experimentally in phantoms and *ex-vivo* studies.

Throughout the manuscript this last approach is considered standard to characterize microvascular flux dynamics during tumor growth or explore the potential of FENSI applied to fMRI. Recently, Ouyang et al. (85) used the same preparation modules and implemented the technique on a 3 T clinical scanner. Along with their study, our results suggest that robust *in-vivo* CBFlux quantification can only be achieved with the use of the MT-balanced FENSI method, also known as the “new FENSI” or “quantitative FENSI” technique (qFENSI).

### *One technique, two flux formula*

At the moment, the only two studies that use the new FENSI saturation scheme are the recent publication of Ouyang et al. (85) and this manuscript. Interestingly they use different formula to calculate blood flux. Their differences are highlighted here.

After incorporating  $T_{1b}$  and  $T_{2b}$  relaxation times, Ouyang et al. calculate the blood flux  $Q$  (in  $\mu\text{L}/\text{min}/\text{cm}^2$ ) based on equation [2.10], where  $S_{CS}$  represents the cross-sectional section of a single voxel,  $T_{SAT}$  the tagging duration,  $\lambda_1$  the water content of blood and  $\alpha$  the labeling efficiency (assumed equal to 1).  $V_{IMG}$  and  $V_{POST-TAG}$  are the imaging voxel volume and post-tag saturation volume inside the imaging voxel, respectively.  $\Delta M$  is the flux-weighted image signal,  $M_{0,CSF}$  the CSF signal at equilibrium and  $w$  the post-tag time delay between the tagging and image readout.

$$Q = \frac{60 \times 1000}{S_{CS} \cdot T_{SAT} \cdot \lambda_1 \cdot \alpha} \cdot (V_{IMG} - V_{POST-TAG}) \cdot \frac{\Delta M}{M_{0,CSF}} \cdot \exp\left(\frac{w}{T_{1b}}\right) \cdot \exp\left(\frac{TE}{T_{2b}}\right) \quad 2.10$$

On the other hand, CBFlux is quantified in this manuscript using equation [1.6]. After reorganization and change of the unities to match those of [2.10] (in  $\mu\text{L}/\text{min}/\text{cm}^2$ ), equation [1.6] becomes [2.11], where  $I_{STATIC}$  is the magnetization of the labeling slice at equilibrium and  $\lambda_2$  the brain-blood spin fraction.

$$\text{CBFlux} = \frac{60 \times 1000}{S_{CS} \cdot T_{SAT} \cdot \alpha} \cdot \lambda_2 \cdot V_{TAG} \cdot \left\{ \frac{\Delta M}{I_{STATIC}} \right\} \exp\left(\frac{T_{SAT}}{T_{1b}}\right) \cdot \exp\left(\frac{TE}{T_{2b}}\right) \quad 2.11$$

### *Labeling efficiency and blood transversal relaxation time*

In practice, both studies assumed an ideal saturation profile ( $\alpha = 1$ ). Our measurements show that this can introduce up to a 15 % underestimation of CBFlux acquired in normal conditions, i.e. little off-resonance effects and proper shim. In future studies, we suggest that  $\alpha$  is measured and accounted for in both formulas before blood flux quantification.

The blood signal decay during TE is not taken into account in the CBFlux calculation based on equation [1.7], where TE is assumed negligible compared to  $T_{2b}$ . This assumption is only valid at low field ( $T_{2b} = 275/45/30$  ms at 3/11.7/17.2 T for arterial blood) and small TEs, of the order of 10 to 20 ms. This effect can introduce a small underestimation of the blood flux (~ 20 - 30%) calculated at 7 T. Absolute quantification of CBFlux at higher fields must account for this effect.

### *Blood longitudinal relaxation time*

The  $T_{1b}$  correction factor impacts the blood flux  $Q$  calculation as the qFENSI method described by Ouyang et al. uses a delay to eliminate the intravascular component of blood flux. Instead, our FENSI implementation at 7 and 17.2 T uses control tags to label intravascular fast flow in both control and tag acquisitions. Substituting  $w = 0$  in [2.10] eliminates the need for this  $T_{1b}$  correction.

Based on our simulations, an additional correction for the  $T_{1b}$  relaxation of the tag during  $T_{SAT}$  is needed, as both clinical and preclinical implementations of FENSI use relatively large saturation times ( $T_{SAT}$  in the range 1000 – 3000 ms) compared to  $T_{1b}$ . The FENSI enhancement dependency on blood velocity was shown in the previous section. This effect has little influence on CBFlux calculation when  $T_{SAT}$  can be considered negligible compared to  $T_{1b}$ , and is reduced at high field. In practice, long  $T_{SAT}$  are necessary to accumulate slow spins within the microvascular network into the imaging slab. Depending on field strength and the particular imaging parameters, both  $Q$  and CBFlux should be adjusted to compensate for the  $T_{1b}$  relaxation of the label.

In this manuscript we chose to approximate for a given spin population the delay between the last saturation and their imaging by  $T_{SAT}$ , provided the FENSI technique is sensitized to the appropriate range of velocities.

*Which reference should we use to quantify blood flux?*

The choice of an appropriate reference signal is investigated. We assume here that the flux-weighted image (taken as the subtraction of the control and tag image intensities) is acquired. One must wonder to which value we need to normalize the signal to derive a volumetric flow rate.

The flowing spins from the label accumulate during  $T_{SAT}$  in the imaging slab. Therefore the signal enhancement obtained in the imaging slice is only relevant when compared to the blood signal from the labeling slice. This signal is also known as the blood equilibrium magnetization  $M_{0b}$ . The difficulty lies in the estimation of that quantity. From equations [2.10] and [2.11],  $Q$  and  $CBFlux$  use a different estimate of this parameter.

Blood has a proton density that differs from that of tissue. Absolute quantification of CBF in ASL (86) and blood flux in FENSI requires knowledge of the magnetization of fully-relaxed blood. Ideally one would calculate the MR signal directly in a large artery. This method is however not applicable to human studies with typical in-plane resolution of 3-4 mm. Regarding FENSI, it is likely that the  $T_{1b}$  in small capillaries and blood vessels (arterioles, venules) differs from the  $T_{1b}$  taken in large arteries (MCA) or veins (sagittal sinus).

A more common practice in ASL is to evaluate the magnetization in grey or white matter  $M_0$  and estimate the magnetization of blood using the blood-brain partition coefficient  $\lambda_2$ . In this manuscript,  $M_0 = I_{STATIC}$  is determined on a voxel-by-voxel basis to account for the spatial dependence of the coil sensitivity. For this means, an additional scan acquires the signal of the labeling slab at equilibrium. The signal is then corrected in equation [2.11] to compensate for the different amount of water molecules in blood and in tissues.

Ouyang et al. (85) use a different approach to calculate the blood flux  $Q$ . They estimate the equilibrium magnetization signal of cerebro-spinal fluid (CSF)  $M_{0,CSF}$  from the mean of CSF signal in the control image dataset, after performing a segmentation of CSF and correction for the  $T_1$  of CSF. Then the conversion factor  $K$  between the MR signal at equilibrium and the water volume can be extracted from the ratio of the true imaging slice volume by the CSF magnetization  $(V_{IMG} - V_{POST-TAG})/M_{0,CSF}$ . Blood flux  $Q$  (in ml/min/cm<sup>2</sup>) is then defined as the volume of tagged flowing spins  $\Delta M/K$  divided by the cross-section of a single voxel  $S_{CS}$  and the accumulation time  $T_{SAT}$ .

Note that the two flux formula use different partition coefficient  $\lambda_1$  (blood/water) and  $\lambda_2$  (blood/brain). Their correct utilization is controversial in literature (87-88), but necessary to compensate for the difference in proton density between an ideal reference signal (blood) and the chosen reference signal (CSF signal or local gray matter signal). The unit of the measurement

also changes (ml/min/g tissue, or ml/min), depending on whether the partition coefficient is weighted by the brain density or not.

Compared to our voxel-by-voxel correction technique, the method proposed by Ouyang et al. is advantageous in terms of acquisition time and noise as a single correction factor applies to the entire flux-weighted image. The accuracy of the absolute quantification of blood flux must however be carefully investigated, as this method can introduce a bias in relative blood flux calculations due to the coil sensitivity.

On the other hand, the CBFlux calculation does not suffer from  $B_1$  inhomogeneities. MR acquisitions performed with a surface coil (home-built 2 cm diameter single loop) show uniform flux values in the whole brain. Plus, CBFlux maps can be derived everywhere in the brain, as there is no need for a CSF ROI. Moreover, the post-processing can be performed automatically once the FENSI dataset is acquired. The drawback of the method is an extended acquisition time necessary to prevent any major decrease of the CBFlux map SNR, and an increased CBFlux sensitivity to artefacts that might contaminate the reference image, especially at UHF.

### *Blood flux and flowing spins fraction*

Both measures ( $Q$  and CBFlux) are only valid to a certain extent. As mentioned in chapter 1, two different uses can be made of the FENSI preparation module. By adjusting  $L_{\text{IMG}}$ ,  $L_{\text{SAT}}$ ,  $L_{\text{PS}}$  and  $T_{\text{SAT}}$ , the technique can be sensitized to very small flows in the range  $[v_{\text{MIN}} - v_{\text{P}}]$ .  $Q$  and CBFlux provide an accurate measure of blood flux for velocities below  $v_{\text{P}}$ .

For large velocities ( $v > v_{\text{P}}$ ) the spins escape the imaging slice before the end of the saturation period. They are replaced in the image by newly labeled spins. All large velocities contribute equally to the tag image. Therefore the signal enhancement obtained at the position  $(x,y)$  in the imaging plane will only depend on the number of flowing spins in the voxel of coordinates  $(x,y)$  inside the labeling plane, regardless of their velocity. In that particular case, FENSI can be used to probe the local properties of blood volume, but will not reflect blood flux at capillary level.

### *CBF, CBFlux and $Q$*

It is possible to provide a rough estimation of CBF based on our FENSI measurements, to verify the agreement of both models and the accordance of the orders of magnitude that defines perfusion. We assume here that the

CBFlux calculated in cortical gray matter using our usual FENSI parameters (CBFlux  $\sim 150 \mu\text{L}/\text{min}/\text{cm}^2$ , see previous section) approximates the cortical cerebral blood flow through the tagging plane (effective thickness  $L_{\text{SAT}} \sim 2.5 \text{ mm}$ ). The volumetric flow is approximated by  $\text{CBFlux}/L_{\text{SAT}}$ . To convert in ASL units, we assume a tissue density of  $1 \text{ g}/\text{cm}^3$ . A CBF measure of the order of  $70 \text{ mL}/\text{min}/100\text{g}$  of tissue is in good agreement with literature on perfusion MRI using PASL and VS-ASL (59).

This also corroborates the results of Ouyang et al. (85) that calculated blood flux  $Q$  in the human brain based on equation [2.10] and derived a similar estimation of CBF around  $75 \text{ mL}/\text{min}/100 \text{ g}$  tissue in cortical gray matter. This illustrates the concordance of both flux formulas.

### *On the comparison between FENSI and ASL*

It should however be emphasized that direct comparisons between CBF and CBFlux must be avoided in general. ASL methods investigate the blood in-flow after the labeling of a major artery, and FENSI examines the capillary outflow of a slice of interest in a specific direction. The characterization of microvasculature is based on two different blood flow mechanisms and cannot be directly compared. FENSI and ASL are two distinct tools to probe the inner mechanisms of microvasculature that can provide complementary information.

### *Conclusion*

After implementation of the new MT-balanced preparation module, the new FENSI technique (or qFENSI) is shown suitable to investigate the brain microvasculature. Despite minor differences in the blood flux formulas, the quantification approach chosen in this manuscript is in good agreement with literature on FENSI and ASL. It is shown here that the FENSI technique is successfully implemented on both preclinical and clinical MR systems. The next chapter will inquire about the first preclinical application of FENSI: its potential to investigate and quantify the development of brain tumor at microvascular level.

### **III. Quantifying brain tumor microvascular flow dynamics using FENSI**

**W**e investigate in this chapter the use of the Flow Enhanced Signal Intensity method to characterize tumor microvasculature at different steps of glioma development. The context and mechanisms of tumor growth and angiogenesis are introduced in a first section. The role of FENSI compared to other perfusion studies is also discussed.

The main characteristics of the precise rat brain tumor model chosen in this study (9L gliosarcoma) are presented. The evolution of tumor growth suggests evidence of two distinct phases of medium and fast tumor expansion.

Absolute quantification of tumor blood flux is performed on five rats between 5 and 15 days after glioma (9L) cells inoculation. No significant difference emerges from the group analysis performed on the data collected at early stage (tumor size  $< 3$  mm): two/three rats exhibit a significant increase/decrease in tumor blood flux (paired t-test,  $p < 0.05$ ), respectively. At a late stage (tumor size  $> 3$  mm) we observe a significant decrease of the cerebral blood flux inside the gliosarcoma ( $-40\%$ ,  $p < 0.01$ ).

In addition, we characterize the late stage 9L gliosarcoma tumor compartmentalization and neo-vascularization based on microvascular flux dynamics. Our flux measurements corroborate literature on perfusion, 9L tumor morphology studies and concentration of blood microvessels obtained with immunohisto-chemistry.

We show that absolute quantification of flux at microvascular level is suitable to detect several compartments in tumor regions and characterize angiogenesis and perivascular invasion at late tumor stage.

### **III.1 Glioblastoma Multiforme and perfusion MRI**

In this first section we introduce the most common family of brain neoplasms and the mechanisms of angiogenesis associated with high grade brain tumors. The role of perfusion MRI is highlighted and the use of FENSI justified compared to classical ASL techniques.

#### *Glioblastoma*

Glioblastoma Multiforme (GBM; World Health Organization, Grade IV astrocytoma) represent today the most common type of malignant brain tumors (and 40 % of primary CNS tumors) with very poor prognosis (89-90). Despite recent advances in treatment (chemotherapy, radiation, surgery) and multiple modality therapies (91-92), the overall survival time for patients has not changed since the 1970s (1 to 2 years). These infiltrative CNS tumors are characterized by microvascular proliferation associated with endothelial hypertrophy and hyperplasia, glomeruloid vessels and occasional necrosis (93).

#### *Angiogenesis & Tumor Grading*

The mechanism of angiogenesis (growth of blood vessels) is essential for organ growth and repair. However, misregulation of pro- and anti-angiogenic molecules can induce metastasis and tumor growth in cancer (94). In particular, members of the vascular endothelial growth factor (VEGF) and angiopoietin (Ang) families are known to play a predominant role in tumor vascular growth (95-96). The balance between the different factors influencing tumor angiogenesis is poorly understood and the angiogenic switch can be turned 'on' by various stimuli, such as metabolic or mechanical stress, or oncogenes activation among others.

Angiogenesis and microvascular proliferation are important biomarkers of Grade IV tumors. GBM can develop from lower grade tumors or appear *de novo* without clinical history. Lower grade CNS neoplasms (II and III) are also fatal but present longer survival times (3 to 8 years). Therefore it is crucial to detect any physiological evidence of microvascular proliferation suggesting an increase in tumor malignancy.

## *Perfusion MRI*

In this context, Magnetic Resonance Imaging (MRI) represents a powerful tool for the diagnosis and characterization of the response to therapy in tumors in non- or minimally- invasive ways (97-100). Perfusion-MRI techniques (22,101-104) are particularly useful as they provide not only anatomical information but also physiological data. For instance, detection of hypoxic regions in GBM (poor oxygen supply due to low perfusion) is of prime interest as they are severely proangiogenic and contribute extensively to tumor growth (105). As discussed in chapter 1, there are two main classes of perfusion MRI methods currently used: bolus tracking after an injection of exogenous contrast agent and labeling of water protons as an endogenous contrast agent. We only consider the latter here.

### *Characterizing tumor microvasculature with FENSI*

The MR methods which use water as endogenous contrast agent include ASL techniques (50,59,86,106) and FENSI (1,74-75). ASL is performed in numerous studies to assess tumor perfusion in a non-invasive way (21,107-109). FENSI presents several advantages compared to ASL. First, as only the saturated spins still located in the imaging slice contribute to the final flow map FENSI is less sensitive to flow coming from large blood vessels (velocity  $> 10$  mm/s), and reflects mainly the microvascular flux (velocities: 0.5 – 2 mm/s in a rat brain) (110-111), assuming the appropriate acquisition parameters. Second, because the spins imaged are those in the saturation slice, no delay is necessary between saturation and imaging modules, which makes FENSI less sensitive to  $T_1$  effects and to blood delivery pathways. These characteristics make FENSI suitable for a complete and non-invasive characterization of tumor microvascular flux dynamics. One disadvantage of FENSI is that, due to the imaging geometry, it is limited to single slice acquisitions.

## **III.2 The 9L gliosarcoma rat brain tumor growth**

In this section we describe the glioma model chosen in our study, the protocol used to implant the cells, and evaluate tumor growth using MR at different times after 9L glial cells implantation.



### *The 9L gliosarcoma*

GBM regroups three morphologic variants recognized by the World Health Organization: conventional GBM, giant cell GBM and gliosarcoma (93). Representing 2 % of GBMs, gliosarcoma are characterized by biphasic growth pattern (glial/mesenchymal components).

The 9L gliosarcoma has been one of the most widely used rat brain tumor models. It was produced in 1971 by Brenda and Schmidek (112-113) by repeated intravenous injection of MNU (N-methyl-N-nitrosourea) in Fischer rats. The tumor can be easily propagated *in vivo* and *in vitro*, which makes it suitable for a large variety of studies. Extensive research has been performed on tumor responses to radiation (114-115), chemotherapy (116-117), combination of radio- and chemotherapy (117-118), immunotherapy (119-120), or gene therapy (121-123) based on the 9L gliosarcoma model.

Although the 9L gliosarcoma is not a good model to study therapeutic efficacy of gene therapy due to immune amplification (124), it presents important morphological and histological similarities with human GBM. In particular, highly vascularized hypercellular tumors with evidence of necrosis and newly developed blood vessels have been reported (125). 9L studies report also a typical growth pattern characterized by a solid tumor mass surrounded by peripheral invasion (126) presenting high vascular tortuosity (127).

### *Animal Experiments*

300 g Fischer male rats are obtained from Janvier (Saint Isle, France). All experiments comply with French legislation and guidelines for animal research. The animal protocol used was approved by the Comité d'Éthique en Expérimentation Animale Commissariat à l'Énergie Atomique et aux énergies alternatives Direction des Sciences du Vivant Ile de France (CETEA CEA DSV IdF).

### *Cell implantation*

The cells are implanted in the striatum of eight male Fisher 344 rats (Janvier, Saint Isle, France) anesthetized using ketamine (100 mg/kg i.p.) and xylazine (10 mg/kg i.p.). Put in a stereotaxic frame, the skull is exposed after a skin incision. A hole is drilled 3 mm lateral of the bregma. A 10 µL Hamilton syringe containing cell suspensions in a 5 µL DPBS is inserted 5 mm into the left striatum.  $1 \times 10^5$  9L glial cells are injected over a 5 min period of time

(1  $\mu\text{L}$  steps at 2  $\mu\text{L}/\text{min}$  injection rate). The needle is then slowly removed and the skull sealed with bone wax.

### *Imaging protocol*

MRI acquisitions start five days after the inoculation of the 9L gliosarcoma cells (tumor size approximately 1-1.4 mm). Four rats are imaged at six different time points between Day 5 and Day 15. One rat (#4) is only imaged at three time points and is sacrificed at Day 9, due to loss of mobility. In addition, we perform histology on a single animal to finely probe intra-tumor heterogeneity and compare to FENSI flux maps. For all MR acquisition, the animals are anesthetized with 2 % isoflurane in air administered using a nose cone. The rats are maintained still in the magnet using ear bars and a bite bar connected to the nose cone. We monitor the respiration rate and maintain the body temperature at 37°C throughout the experiment.

### *Tumor Growth*

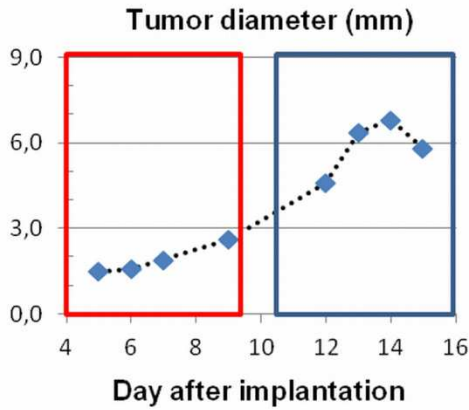


**Figure 3.1 Temporal evolution of tumor diameter (mm).** Based on tumor size, we distinguish two different tumor stages (early/late = red/blue ROI) separated by the threshold diameter / day after implantation:  $\varnothing = 3 \text{ mm} / \text{D}+9$ .

Out of the eight implanted rats, only five develop tumors. In these five rats, the tumors develop mainly around the needle path used for the 9L glioma cells injection. The tumors grow from  $1.5 \pm 0.2 \text{ mm}$  at Day 5 to  $2.5 \pm 0.2 \text{ mm}$  at Day 9. The rat #4 is sacrificed at Day 9. Starting at Day 9, 9L glioma sizes increase more rapidly and reach  $4.6 \pm 0.3 \text{ mm}$ ,  $6.2 \pm 0.2 \text{ mm}$  and  $6.5 \pm 0.5 \text{ mm}$  at Day 12, 13 and 14-15, respectively. The four remaining rats are sacrificed at Day 15. Tumor growth (**Figure 3.1**) exhibits two main stages of tumor development. The following group analysis will focus on cerebral blood flux during the stages of medium (early stage, tumor size < 3 mm) and

fast tumor expansion (late stage, tumor size > 3 mm, usually associated with angiogenesis).

### **III.3 CBF<sub>flux</sub> quantification at early and late tumor stage**

In this section are presented the FENSI acquisition parameters used in this study and the cerebral blood flux maps acquired on rats induced with 9L glial cells. Blood flux results are examined to assess tumor microvasculature at different steps of tumor development.

#### *Acquisition parameters*

The pulse sequence used is a standard Spin-Echo EPI sequence (axial view, 4 segments, TE = 13 ms, TR = 6000 ms, in plane resolution 250 x 280  $\mu\text{m}^2$ , FOV 25 x 28 mm<sup>2</sup>, slice thickness 6.5 mm, NR = 150) preceded by a preparation module (FENSI module) set on “control” or “tag” mode every other TR. The FENSI module repeatedly saturates the spins in the slice of interest (150 loops separated by gradient spoilers) in the “tag” mode or produced no excitation in the “control” mode. To eliminate MT effects we use pairs of 45°+45° // +45°-45° FA pulses (tag//control), as discussed in chapter 2. The FENSI module consists of 0.8 ms long sinc pulses which saturated spins in a 1 mm thick slice for 3 s. The slice thickness and saturation duration are chosen to sensitize the acquisition to velocities down to 0.5 mm/s, and thus to blood flux in cerebral capillaries (110). In order to eliminate possible direct saturation effects generated by the FENSI module (75) we use an additional saturation block covering 1.8 mm around the center of the slice. As seen in Chapter 2, there is no decrease of the tag signal intensity due to the repeated saturation of the static tissue with the FENSI preparation module. The thickness of this last saturation dictates the inferior limit of the velocities we can detect. During the acquisition, only the labeled spins having escaped the 1.8 mm thick slice and remaining in the imaging slice contribute to the flux measured (0.5–10 mm/s). Cerebral blood flux maps are calculated using 150 scan repetitions (75 pairs of control/tag images, TA = 60 min). As reference we perform a SE-EPI acquisition of the FENSI saturation slice (same imaging parameters, 1 mm slice thickness without saturation, NR = 20).

T<sub>2</sub>-weighted images are also acquired using a Fast Spin-Echo sequence (TE<sub>eff</sub> = 56 ms, acceleration factor 8, TR = 3000 ms, FOV 2.56 x 2.56 cm<sup>2</sup>,

matrix size 128 x 128, NA = 4, TA = 3 min 12 s) to localize the tumor and the slice of interest.

Before the beginning of FENSI acquisitions, we ensure the quality of the “tag” and the “control” modules by acquiring a pair of SE-EPI images oriented perpendicular to the tag plane. For these acquisitions the FENSI modules are identical to the “control” and “tag” modules used for flux measurements, but consist of only one pair of pulses (+45/-45 or +45/+45°) instead of 150. We consider the “tag” and “control” satisfactory if they show complete saturation (dark band in the image) or no visible signal loss, respectively.

### *Cerebral blood flux map*

Before averaging, we realign scans from the different FENSI repetitions of “control” and “tag” using Matlab (MathWorks, Natick, Massachusetts) in-house programs. The cerebral blood flux, CBFlux (in units of mL/min/cm<sup>2</sup>) is calculated voxel-by-voxel, using formula  $CBFlux = (I_C - I_T) / I_0 * \lambda * V_{TAG} / S_{CS} * 60 / T_{SAT}$  (see Chapter 2), where  $I_0$  is the signal intensity from the reference image (1 mm thin slice),  $V_{TAG}$  is the volume of one saturation voxel (ml),  $S_{CS}$  the cross-section of a voxel (in cm<sup>2</sup>),  $T_{SAT}$  the total saturation time (3 s) and  $\lambda$  the blood tissue partition coefficient (considered constant across the brain (87)).

Parametric maps of the cerebral blood flux ( $\mu$ L/min/cm<sup>2</sup>) obtained on rat #2 5 days, 9 days and 12 days after glioma cells injection (**Figure 3.2-A**) reveal major vascular changes with tumor growth. The tumor region appears brighter in corresponding T<sub>2</sub>-weighted images (**Figure 3.2-C**).

### *ROI in tumor/healthy region and data analysis*

Tumor ROIs are manually delineated on the T<sub>2</sub> weighted images. For the calculation of mean tumor blood flux, we try to cover the whole tumor region (**Figure 3.2-B**), hence a large variability between the number of pixels used to characterize tumor vasculature at early stage (Day 5,  $22 \pm 2$  voxels) and late stage (Day 14-15,  $395 \pm 90$  voxels). Manual ROI delineation is necessary as in some cases the tumor border is not well defined (**Figure 3.2-A**; rat #2 at Day 9). For each session, an additional ROI is drawn in the striatum of the contralateral hemisphere of the rat brain to calculate cerebral blood flux in healthy tissue. When possible, we choose ROIs of sizes similar to that of tumors in contralateral subcortical regions. This is however not possible for very large tumors (**Figure 3.2-B**). The average voxel number per healthy ROI is  $67 \pm 15$  voxels.

In all analyses errors indicate the standard deviations of the mean ( $\pm \sigma$ ). Student's t-tests are performed to calculate probability (p) values.  $p < 0.05$  is regarded as statistically significant.

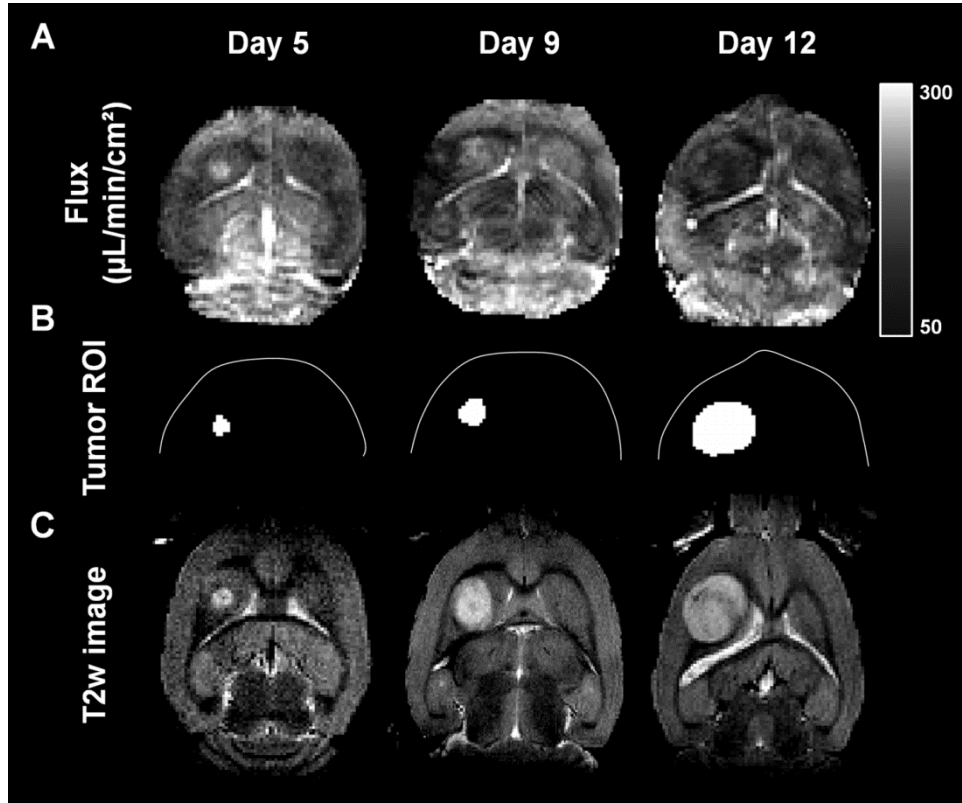


**Figure 3.2 A. Cerebral blood flux ( $\mu\text{L}/\text{min}/\text{cm}^2$ ) maps of the brain (rat #2) acquired at Day 5, Day 9 and Day 12 after 9L glioma cell implantation. B. ROIs used for flux calculation in the tumor and regular subcortex. C.  $T_2$  weighted images of the rat brain used for tumor localization at Day 5, 9 and 12, respectively.**

#### *Early stage tumor blood flux*

The cerebral blood flux measurements in tumor and control regions (mean  $\pm$  standard deviations) calculated for rats #1 to #5 at different time-points, are presented in **Figure 3.3**.

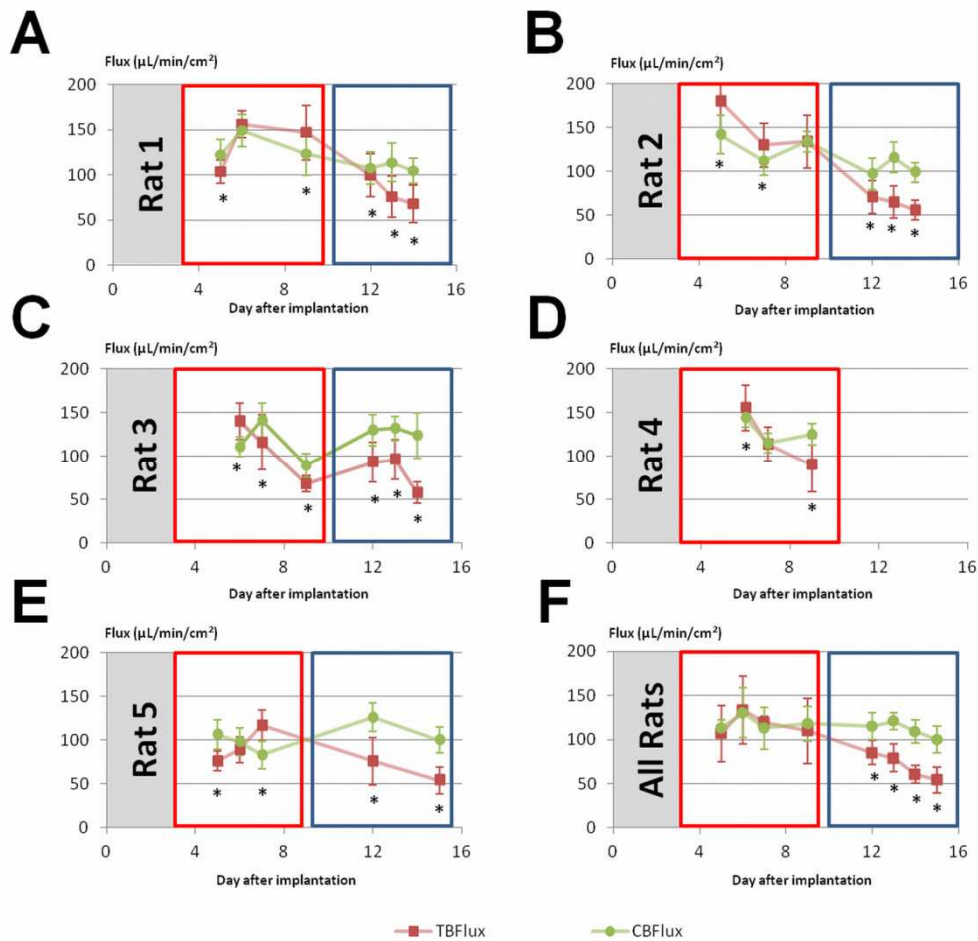


**Figure 3.3 Temporal evolution of tumor blood flux (TBFlux, red squares) and normal cerebral blood flux (CBFlux, green circles) in the striatum of rats #1 to #5 A-E.** Rats #1 and #5 exhibited a significantly lower TBFlux at Day 5 than Day 9 (-32 %,  $p < 0.05$ ). On the other hand the TBFlux of rats #2, #3 and #4 was found significantly higher (+ 62 %,  $p < 0.05$ ) at Day 5 than Day 9. **F.** The results averaged over all the rats show no statistical difference between TBFlux and CBFlux for small tumors (size < 3 mm, delimited by red ROI) and significant lower TBFlux than CBFlux at late stage (tumor size > 3 mm, blue ROI). Rat #4 was sacrificed at Day 9, no data for late stage flux measurements. \* $p < 0.05$

Individual analysis (15 measurements, 5 rats, 3 time points): Intra individual analysis performed at early tumor stage showed a significant difference in the blood flux distribution inside the tumor (TBFlux) and contralateral cortex (CBFlux) in 11 cases (red ROI,  $p < 0.05$ ). As seen in the red ROI in **Figure 3.3-A to 3.3-E**, six measurements (rat#1 D+9; rat#2 D+5 and D+7; rat#3 D+6; rat#4 D+6 and rat#5 D+7) indicate a significant

increase of TBFlux compared to CBFlux (unilateral t-test,  $p < 0.05$ ). Five measurements at different time-points (rat#1 D+5; rat#3 D+7 D+9; rat#4 D+9 and rat#5 D+5) highlight however a decrease of TBFlux, reflecting heterogeneity of tumor development between individuals. Four measurements show no significant difference in TBFlux compared to CBFlux ( $p > 0.12$ ). All the results obtained at early tumor stage ( $n = 15$ ) show higher flux variability in the tumor regions ( $STD_{TBFlux} = 22 \pm 8 \mu\text{L}/\text{min}/\text{cm}^2$ ) than in contralateral subcortex ( $STD_{CBFlux} = 16 \pm 4 \mu\text{L}/\text{min}/\text{cm}^2$ ).

Group Analysis (15 measurements, 5 rats, 3 time points): No significant difference is found in the average blood flux (**Figure 3.3-F**, red ROI) calculated between Day 5 and at Day 9 in the tumor region. No significant difference is observed (**Figure 3.4**,  $p = 0.83$ ) between the mean TBFlux and CBFlux averaged over five rats and five days (early tumor stage).

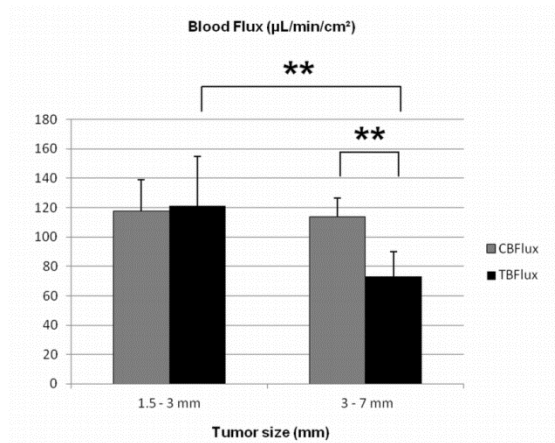


**Figure 3.4 Mean CBFlux and TBFlux (in  $\mu\text{L}/\text{min}/\text{cm}^2$ ) at early and late tumor stage** (tumor size  $> 3 \text{ mm}$ ,  $n = 5$  rats). For small tumor sizes (1.5 – 3 mm), we find no significant difference in the tumor region compared to normal striatum ( $121 \pm 32 // 120 \pm 20 \mu\text{L}/\text{min}/\text{cm}^2$ ,  $p = 0.83$ ). The late stage measurements (tumor size 3 to 7 mm) show a significant lower flux (-40 %) in the tumor compared to early stage TBFlux or late stage CBFlux.  $**p < 0.01$

#### Late stage tumor blood flux

Individual analysis (11 measurements, 4 rats, 3//2 time points for rats #1-3//5): All the intra individual blood flux measurements (blue ROIs in **Figures 3.3-A to 3.3-E**) performed at late tumor stage (tumor size  $> 3 \text{ mm}$ ) show significantly lower flux in tumor than in contralateral striatum ( $p < 0.05$ ). The maximum decrease in microvascular blood flux (-53 %) is found for rat #3 at Day 14 ( $58 \pm 12 // 124 \pm 26 \mu\text{L}/\text{min}/\text{cm}^2$  in TBFlux // CBFlux).

Group Analysis (11 measurements, 4 rats, 3//2 time points for rats #1-3//5): Inter individual analysis on 4 rats (tumor size  $> 3 \text{ mm}$ ) show major vascular changes in the tumor (**Figure 3.4**). At late stage, the TBFlux is significantly lower than the CBFlux (-40 %,  $p < 0.01$ ). No significant difference

can be obtained between the data from two consecutive dates (Day 12 - Day 13, Day 13 - Day 14, Day 14 - Day 15).

### *Imprecision on flux calculations*

MT and direct saturation effects are negligible in the current FENSI implementation. However, it should be noted that the radio-frequency concatenation scheme used to remove MT effects is very sensitive to magnetic field inhomogeneities. In the absence of a sharp label, direct saturation will lead to CBFlux overestimation. This phenomenon is observed in phantom samples (4 % magnetization decrease between control and tag) as well as in the cerebellar regions which lie outside the shimmed volume (+ 90 to 120 % overestimation of flux). The opposite phenomenon can occur. When the spin population is not efficiently refocused by the second  $-45^\circ$  FA pulse in the control image, CBFlux is underestimated due to poor labeling efficiency. Although the analysis of the cerebral blood flux in those regions is not the purpose of our study, special attention must be given to shimming in order to perform flux measurements of the entire brain.

For large tumors, one should bear in mind that the disruption of the BBB (128-130) can lead to imprecision on FENSI flux measurements. The influence of BBB disruption on FENSI is not investigated experimentally in this study.

Regarding the intra-individual comparison, TBFlux and CBFlux are compared on a pixel-by-pixel basis when applicable. For large tumors, the ROI size exceeds however the maximum ROI size of striatum with this orientation. Comparison is then performed by considering an ideal normal distribution inside the healthy striatum, defined by the mean and standard deviation of the CBFlux calculated in the subcortex.

### *Choice of axial orientation*

One of the specificities of FENSI when compared to ASL is that it is sensitive to only the velocity component perpendicular to the tagging plane (axial component in the current study). Our choice of slice orientation is motivated by the fact that it is found to be the most advantageous in terms of  $B_1$  homogeneity across the tumor given the surface coil used. Moreover, FENSI experiments performed on healthy rats along three orthogonal orientations (sagittal, coronal and axial, see **Figure 2.9**) show no influence of slice orientation on the flux measured in subcortical regions, suggesting isotropic



sanguine flux. As this type of gliosarcoma (and Glioblastoma in general) exhibits high vascular tortuosity (127), it is very likely that the microvascular tumor flux has a isotropic character as well. Given these considerations we assume that, for the present study and given our particular regions of interest, the FENSI flux measurements were orientation independent.

#### *Consistency with literature on 9L perfusion*

Our results highlight two distinct stages of tumor development. No general trend can be obtained from the longitudinal evolution of tumor blood flux in small tumors (size < 3 mm), reflecting highly heterogeneous vascular development at this early stage. The late 9L gliosarcoma developmental stage is characterized by a fast expansion, large tumor size and significant decrease in microvascular blood flux in the whole tumor region (-38 to -52 %). These results are consistent with perfusion measurements of TBF (Tumor Blood Flow) performed with ASL (107), DSC-MRI (131) or autoradiography (126); reporting respectively 53, 42 and 60 % lower blood flow in 9L gliosarcomas compared to normal CBF. Typical patterns of 9L gliomas growth (112-113,132-133) are encountered in this study. No necrosis is observed in small vascularized tumors (134), and the gliosarcomas eventually invade all the available intra-cerebral structures around the initial 9L injection site (135).

### **III.4 Compartmentalization of tumor at late stage**

We evaluate in this section the heterogeneity of microvascular blood flux inside the tumor region. These are segmented using an automatic algorithm. The positions of low and high tumor blood flux regions are compared with immunohisto-chemistry on a single animal.

#### *9L glioma segmentation based on microvascular flux calculation*

All measurements performed at late tumor stage show reduced TBFlux compared to CBFlux. Moreover, within the tumor, different compartments present distinct microvascular characteristics (**Figure 3.5-A**; rat #2 at Day 12, tumor size 4.4 mm) according to the tumor flux distribution (**Figure 3.5-C**). Tumors are segmented into two compartments based on flux level and minimum within-class variance: the core and the peripheral region of the

gliosarcoma (rat #2, **Figure 3.5-B**). In these two regions the flux measurements follow two normal distributions (**Figure 3.5-D**; solid // dashed line) which differ significantly ( $p < 0.05$ ). The average TBF<sub>flux</sub>, TBF<sub>flux<sub>LOW</sub></sub> and TBF<sub>flux<sub>HIGH</sub></sub> calculated on the four rats at late tumor stage (**Figure 3.6**;  $n = 11$  measurements) highlight a significant difference between the vascular properties of the two tumor compartments ( $60 \pm 13$  /  $88 \pm 19$   $\mu\text{L}/\text{min}/\text{cm}^2$ ,  $p < 0.05$ ).

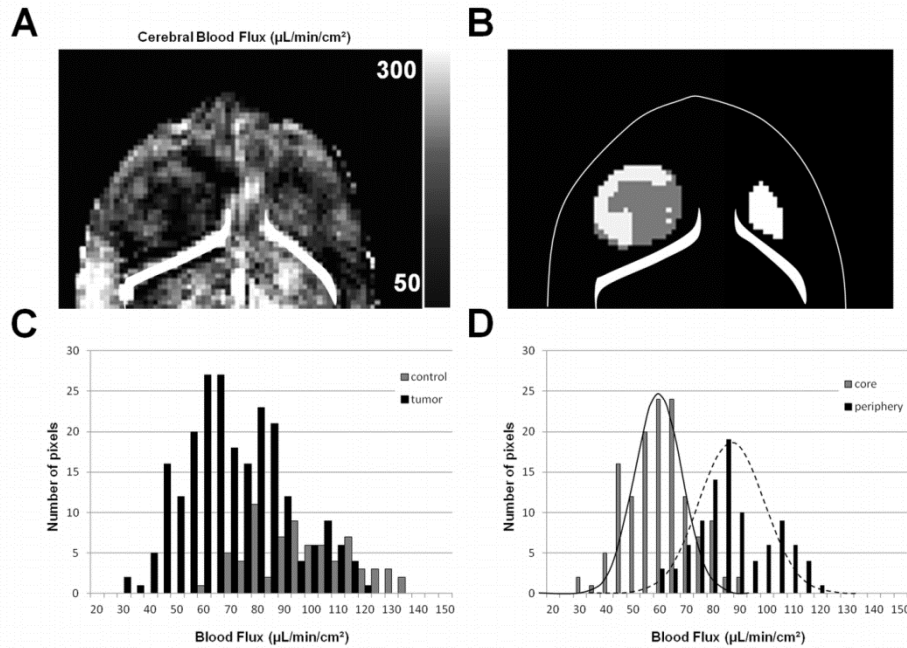


**Figure 3.5 Flux distributions inside the tumor and normal tissues ROIs.**

**A.** Cerebral blood flux map ( $\mu\text{L}/\text{min}/\text{cm}^2$ ) obtained in rat #2 at Day 12. **B.** Positions of the different regions used for flux calculation in the tumor (light/dark gray ROI) and contralateral healthy tissue (white ROI). The ventricles are also shown for registration with flux map. **C.** The flux in the whole tumor region (black histogram) does not follow a single-mode normal distribution. Segmentation of the tumor using minimum within-class variance exhibits two regions (dark/light gray) of low/high flux around the core/periphery of the tumor, whose **D.** flux distributions significantly differ ( $p < 0.05$ ) and match the normal distributions superimposed in plain line // dashed line ( $60 \pm 13$  //  $89 \pm 14$   $\mu\text{L}/\text{min}/\text{cm}^2$ ).

Both mean blood flux values calculated in tumor core and periphery are significantly lower than those obtained in the contralateral subcortical regions ( $-23$  to  $-48\%$ ,  $p < 0.05$ ).

The segmentation of the tumor based on blood flux intensity reveals specific vascularization patterns inside the glioma (**Figure 3.7**). The ROIs presenting low flux are not located at the center of the tumor but match the position of the original 9L cell suspension implantation (tumor core, indicated

by the white cross), suggesting a preferential tumor expansion direction towards the bregma.

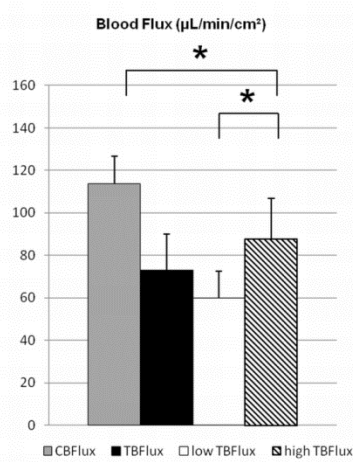


**Figure 3.6 Mean CBFlux and TBFlux in the different tumor compartments at late stage.** Inside the tumor, our data highlight a significant difference of blood flux (~30 %,  $p < 0.05$ ) between the two compartments (white / hashed). In all cases ( $n = 11$ ) the blood flux measured in healthy tissue was higher than cerebral blood flux measured in the high flux tumor region (+20 %,  $p < 0.05$ ).

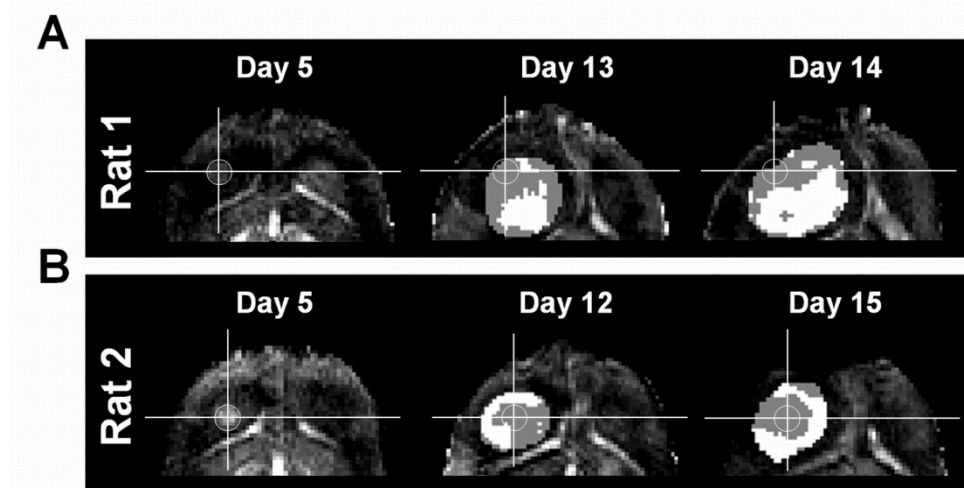


**Figure 3.7 Late stage flux-based tumor compartmentalization.** The white cross delineates the position of the 9L cell suspensions implantation that can be observed at Day 5 on **A.** rat #1 and **B.** rat #2. At late stage different compartments can be segmented within the tumor, based on flux level. The regions of low and high flux are superimposed in gray and white, respectively. These ROIs exhibit on the cerebral blood flux maps acquired at Day 13 and Day 14 on rat #1 a higher vascularization of the tumor near the ventricles. The compartmentalization of the tumor of rat #2 **B.** at Day 12 and Day 15 reveals a peripheral vascular invasion.

*Immunohisto-chemistry and microvessel concentration*

We perform immunohisto-chemistry on rat #2, presenting a distinct pattern in the blood flux maps measured with FENSI (low flux in tumor core located at the center of the whole tumor ROI and higher flux in tumor periphery). At Day 15, the brain of the rat is perfused with a saline solution enriched with 4 % paraformaldehyde (PFA) and extracted. For cryo-protection, it is successively kept in PFA for 24 h, in 15% sucrose solution for 12 h and in 30% sucrose solution for 24 h. Fluorescence microscopy is performed on an Axio Observer Z1 microscope (Carl Zeiss MicroImaging GmbH, Germany). In order to assess tumor vasculature, we analyze CD31 immuno-positive vessels, as in (127,129,136). We examine the blood vessel concentration on the images obtained on the tumor core and edges at zoom x 20. A DAPI staining is also performed in order to co-register the microvessel position with the nuclei concentration. The tumor is delimited by the red arrows in a zoom on the cerebral blood flux map obtained at Day 12 (**Figure 3.8-A**). **Figure 3.8-B** presents superimposition of DAPI (nuclei) and CD31 (endothelial cells) staining on histological slice (Day 15). We zoom on a ROI covering one edge of the tumor (RED box). We observe a higher concentration of endothelial cells at the periphery of the tumor (region 2) than in surrounding healthy tissue or more central parts of the tumor (regions 1 and 3). A more central part of the tumor show evidence of cellular necrosis (low concentration of nuclei) matching areas of hypo-intense signal revealed with  $T_2$  weighted MR images.

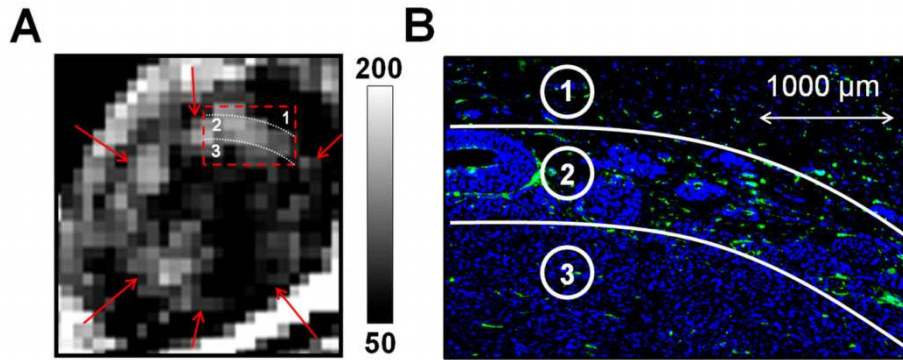


**Figure 3.8 Tumor microvasculature assessed with Fluorescence microscopy.** **A.** Zoom of the tumor region in the cerebral blood flux map (in  $\mu\text{L}/\text{min}/\text{cm}^2$ ) from rat #2 at Day 12 (**Figure 3.5-A**). The tumor is delimited by the red arrows. **B.** Immunohisto-chemistry of vessels (anti CD31, green) and cell nuclei (DAPI, blue) from white matter (ROI #1), tumor edge (ROI #2) and 9L gliosarcoma brain tissue (ROI #3) on rat #2 at x20 magnification. Fluorescence microscopy highlights high concentration of blood vessels on the periphery of the tumor.

## *Discussion*

Inside the tumor, regions of low blood flux co-register with the initial 9L glial cells implantation position. The identification of the two distinct developmental stages, as well as the presence of the two tumor regions in the advanced stage, is consistent with literature results on 9L characterization (137-138) and several studies that mention a recognizable growth pattern with the presence of a solid mass surrounded by extensive perivascular invasion (126,139). Moreover, hyper- and hypo-perfused tumor regions revealed by FENSI correlate well with regions of high and low concentration of blood microvessels observed with immunohisto-chemistry (CD31 staining). This suggests that the hyper-intense flux regions in the tumor reflect the neo-vascularization associated with grade IV tumors. Immunohisto-chemistry revealed a hypercellular tumor with spindle-shaped morphology and evidence of newly formed blood vessels, in good agreement with other studies on the subject (125-126,129,134-135). Our data also exhibit a necrotic area in the central part of the tumor, as previously reported on this model (125,134). Hypercellular zones surrounding small necrotic foci also suggest pseudopalisading (105,140) areas at the very edges of the tumor.

Immunohisto-chemistry is only performed on rat #2 in this study, due to technical limitations at the time of the experiment. Given that a single slice of FENSI is acquired for each rat, comparison with histological slides would benefit from an increased statistical power. In addition, CBFlux maps are based on EPI encoding schemes that can suffer from signal distortions. Because the thickness of the FENSI labeling slice (1 mm) exceeds from two orders of magnitude that of immunohisto-chemistry (10  $\mu$ m), the registration of both images is also challenging. It is possible that FENSI and immunohisto-chemistry do not reflect the same very local alterations of the brain microvasculature inside the tumor.

Future investigations on the angiogenesis mechanism will focus on an extensive comparison of CBFlux (acquired with smaller labeling thickness) with endothelial cell staining. We also intend to incorporate an injection of Gd to the experimental protocol and derive additional correlations of CBFlux with CBV, CBF, mean vessel diameter and density and size index.

## *Conclusion*

In this chapter we demonstrate the use of FENSI for the investigation and quantification of microvascular changes associated with tumor growth in the 9L rat brain tumor model. In addition to the microvascular flux measurements consistent with other perfusion techniques, FENSI flux maps delineate, at late stage, two regions with different vascular contents: a hypo-perfused core and a peripheral region presenting regular blood flux. We show that absolute quantification of flux with FENSI at microvascular level is suitable to detect several compartments in tumor regions and characterize angiogenesis and perivascular invasion at late tumor stage. The FENSI technique can help quantifying cerebral blood flux at capillary level and revealing the areas of high microvessel proliferation associated with the angiogenic process.



## IV. Towards FENSI functional MRI

In this chapter is investigated the possibility to perform functional MRI experiments with the FENSI technique, and its potential advantages and pitfalls compared to the conventional Blood Oxygen Level Dependent (BOLD) imaging based on  $T_2^*$  contrast.

In the first section we describe the principles and mechanisms of BOLD contrast characterizing brain activity in response to a stimulus. Compared to BOLD, perfusion fMRI can in theory provide a more localized and quantitative measure of neuronal activation.

A robust BOLD fMRI protocol dedicated to rodent is first set-up on the 7 T preclinical MRI scanner. Various stimulation, anesthesia and imaging parameters are optimized in order to ensure a reliable and constant detection of brain activity during three hours. Measurements of CBFlux at 7 T during a hypercapnic challenge illustrate a relatively poor SNR obtained with dynamic FENSI images, i.e. single control-tag intensities subtractions, compared to BOLD fMRI. As a result, no significant difference can be found between the FENSI data acquired during electrical forepaw stimulation and at rest.

The fMRI protocol is implemented at UHF. At 17.2 T and in the absence of stimulation, the influence of different commonly used anesthetics on the BOLD contrast is quantified. The feasibility to perform GE-EPI fMRI at UHF is shown.

FENSI gains in SNR at UHF. It offers interesting perspectives to compare in the future the hemodynamic and microvascular responses to stimulation, based on BOLD and CBFlux contrast, respectively. Despite a great potential for fMRI and a highly localized quantitative measurement of brain metabolism, FENSI seems more suited for treatment follow-up, cancer and pharmacological studies and not adapted to resolve the mechanism of neurovascular coupling.



## IV.1 fMRI, BOLD, CBF and CBFlux

In this section we introduce functional MRI and explain how neural activity is classically characterized using MRI. We discuss the limitations of the BOLD technique, and the potential advantages of ASL and FENSI.

### *Mapping cerebral activity with MRI*

Belliveau et al. performed in 1991 the first human functional MRI experiment by injecting a Gd-based contrast agent in a patient (141). As in DSC-MRI, the integral of the Gd concentration over time during the first passage of contrast agent in the tissues is proportional to the CBV. Performing the experiment twice (once at rest and once under a visual task), the local CBV changes observed in the brain directly reflect brain metabolism and glucose consumption. In parallel, Turner et al. investigated the dynamic changes in blood oxygenation induced by anoxia in the cat brain using BOLD contrast associated with fast imaging (EPI) (142).

Since the early 1990's, the number of studies using MRI in order to assess the brain activity in response to a specific task has increased exponentially. A query on an up-to-date database (Pubmed) using the keywords 'fMRI' or 'functional MRI' reports more than 27000 peer-reviewed publications with more than 3000 only in 2011. Currently, fMRI is mainly used to explore functional localization and physiological properties of specific regions of the brain. Due to the strong response of the BOLD signal to any stimulus, the large majority of human and preclinical functional neuroimaging studies uses BOLD contrast, rather than DSC-MRI or perfusion MRI techniques. The mechanisms of BOLD fMRI are detailed in the next paragraph.

### *The BOLD signal*

In 1990, Ogawa et al. reported evidence of MRI contrast generated at 7 T on rats by changing the venous blood oxygenation level (143-144), making functional brain mapping feasible without the need of an exogenous contrast agent. The principle of BOLD contrast lies at microvascular level and uses deoxyhemoglobin as an endogenous contrast agent through the venous network.

BOLD contrast relies on two factors. First,  $T_2^*$ -weighted imaging (typically using Gradient Echo sequences) is very sensitive to local magnetic field inhomogeneities, particularly at high field. Second, the hemoglobin molecules present different magnetic properties, whether carrying oxygen (oxyhemoglobin,  $\text{Hb}(\text{O}_2)_4$ , diamagnetic) or not (deoxyhemoglobin, Hb, paramagnetic). Therefore any local change in the concentration of oxy/deoxyhemoglobin (oxyHb/Hb) will affect the MR signal and give rise to the BOLD contrast.

### BOLD fMRI

At cellular level, neuronal activity is accompanied by an increase of  $\text{K}^+$ ,  $\text{Na}^+$  and  $\text{Ca}^{2+}$  flux. The ATP concentration increases as glucose is consumed. The neurons and astrocytes at stake call for an elevated blood supply through vasoactive signals and CBF increases in the local vasculature (at microvascular, venous and arterial level). Both CBV and CBF increase in response to neuronal activity (**Figure 4.1**). However, the oxygen supply exceeds the consumption rate and the additional oxyHb content is not fully transformed. In the capillary and venous structures, the oxyHb level increases as that of Hb decreases. Because the susceptibility disturbance due to the intravascular compartment is reduced, the local magnetic susceptibility decreases, leading to a signal increase in susceptibility-weighted ( $T_2^*$ -weighted) images.

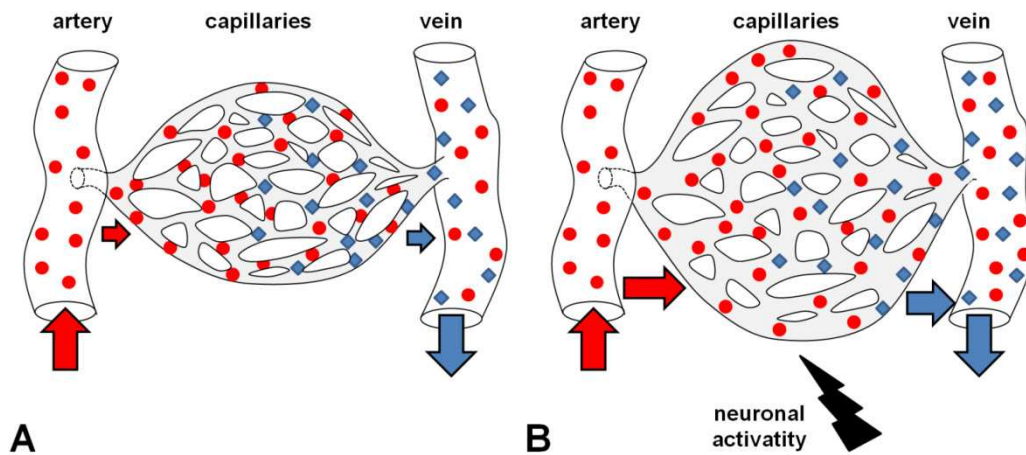


**Figure 4.1 Functional vascular response.** **A.** Capillary network at rest with baseline CBF (red arrow) and CBV (gray surface). **B.** The CBV and CBF increase in response to a stimulus. The excess of oxyhemoglobin (red circles) compared to oxygen consumption lead to a decrease of the relative Hb/oxyHb concentration. The capillary and venous oxygenation level increase and generate BOLD contrast.

Functional experiments consist usually in short continuous MRI acquisitions using fast imaging schemes (EPI, Spiral) while a series of block stimuli is applied. Functional mapping is obtained from the correlation of the BOLD signal change (on the order of 1-10 %) with the stimulus paradigm (**Figure 4.2**). Compared to other functional methods, this technique is very sensitive to small changes and can achieve high spatiotemporal resolution. Typically, a clinical BOLD fMRI experiment at 1.5 T lasts 2-3 min and can detect brain activity at millimeter resolution.

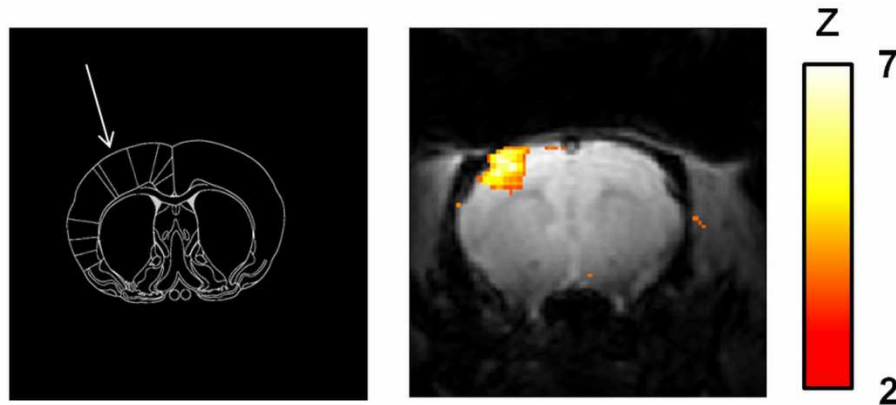


**Figure 4.2 Brain activity in the rat primary somatosensory cortex S1 (white arrow) is detected during forepaw electrical stimulation.** *The statistical Z-score (unilateral student's t-test, calculated voxel-by-voxel) is superimposed on the  $T_2^*$ -weighted image of the rat brain (axial view, resolution  $250 \times 250 \times 1200 \mu\text{m}$ ). Z-score  $> 1.95$  is equivalent to  $p < 0.05$ . The position of the neuronal activation matches the primary somatosensory cortical area S1 (The Rat Brain in stereotaxic coordinates, G. Paxinos & C. Watson, 1998).*

### *Perfusion fMRI versus BOLD fMRI*

However common, BOLD is not the only type of contrast capable of mapping the brain activity. Soon after the first discovery of fMRI, studies report detection of the neural response based on CBF measurements (47,145). We will detail here the potential advantages of FENSI and ASL techniques compared to conventional BOLD fMRI.

First, BOLD contrast suffers from lack of spatial specificity. Both intravascular (veins) and extravascular (capillary network) oxyHb/Hb levels change during neural activity. By targeting the tracer (Hb) in the venous system, the BOLD contrast is contaminated by signal fluctuations and delayed responses coming from the large vessels. This phenomenon has been well studied (146-147) and can be avoided by the use of Spin-Echo (SE) sequences

(along with small diffusion gradients), instead of the common Gradient-Echo (GE). The sensitivity to magnetic susceptibility changes is however reduced when using SE, and one will in practice only choose to perform SE BOLD fMRI at sufficiently high magnetic field. On the other hand, ASL and FENSI techniques can be sensitized to the capillary bed and reflect microvascular dynamics only. Using two-photon microscopy, Chaigneau et al. showed in 2003 that the capillary network directly outlines the areas of neural activity near the rat olfactory bulb (148). Potentially the brain activity can be mapped at sub-millimeter level (100  $\mu\text{m}$ ) using the appropriate sequences.

Second, differences in onset times are commonly observed when performing BOLD fMRI, in both rodent and human studies. The local hemodynamic response depends indeed on the precise contribution of pial veins which drain oxygen through the capillaries. In practice, the cortical venous distribution belongs to a complex architecture well described in literature (149-150). As a consequence, BOLD signal changes (delay and amplitude) must not be compared between different spatial locations. At microcapillary level (e.g. FENSI), the common response to a particular stimulus is expected to be simultaneous. Differences in onset times can be correlated to neural inference.

Last but not least, the BOLD contrast is an indirect marker of the brain activity. It relies on the mismatch between CBF and  $\text{CMRO}_2$  (oxygen uptake by the tissues). As a result, BOLD depends on CBF, CBV, and  $\text{CMRO}_2$  at rest and during stimulation. The comparison of brain metabolism with BOLD under different pharmacological states is biased by changes of the baseline CBF and CBV, that directly impact the dynamics and magnitude of the BOLD signal change. The exact relationship between BOLD and neural activity is complex and still debated at the moment. The interested reader can refer to recent reviews presenting a clear overview on the subject (151-152). To summarize, BOLD fMRI requires knowledge on physiological parameters typically hard to determine in order to quantify brain activity. On the other hand, CBF (or CBFlux) and brain metabolism are strongly coupled (**Figure 4.1**). Moreover, CBF and CBFlux represent direct quantitative markers of the microvascular response, and can detect both arterial and venous flow. In particular, FENSI is capable of probing CBFlux at microcapillary level, where oxygen is delivered and exchanged with the tissues. It is expected that ASL and FENSI techniques can estimate more efficiently the brain response, by calculating a more localized and quantitative measure of the neural activity.

These potential advantages must be carefully investigated while also keeping in mind the pitfalls of perfusion fMRI compared to BOLD fMRI. First, FENSI and ASL techniques suffer from a lower temporal resolution because they require acquisition of two sets of images ("control"/"tag") with an efficient saturation/inversion (FENSI/ASL). They can also lack of sensitivity as they only label 1-5 % of the total population of spins (see Chapter 1). Luckily, the

first CBF and CBFlux signal changes reported under stimulation were on the orders of +50 % to +100 % compared to baseline (up to 10 % of the reference signal i.e. control image).

In this chapter, we present several experiments performed at high and ultra high field in order to investigate the brain hemodynamics and the potential of FENSI fMRI. Being the gold standard, the implementation of a robust BOLD fMRI protocol at 7 T is of prime interest to detect reliable neural activity in the rat brain. The potential of FENSI fMRI is explored at 7 and 17.2 T, and we report our preliminary findings on CBFlux changes during electrical stimulation. The influence of brain hemodynamics and anesthetics on BOLD contrast is also examined at UHF.

## **IV.2 Preclinical BOLD and FENSI fMRI at 7 T**

In this section we describe the different parameters that can influence the BOLD response and detail the particular set of parameters used to obtain a robust functional MRI protocol in the rat brain at 7 T. The BOLD response to a forepaw stimulus is characterized. The FENSI technique does not detect significant CBFlux changes during stimulation at 7 T.

### *The fMRI set-up*

Many parameters can influence the brain hemodynamic response and its detection using MRI. Any modification of the imaging parameters, the rat physiological condition or the stimulation paradigm will affect the BOLD contrast and prevent direct comparison of signal changes. In practice, changes of temperature and respiration rate can reflect changes in the rat condition and one must carefully monitor all the available physiological parameters when performing fMRI. During our experiments we maintain the temperature of the rat constant (37°C) using a feedback controlled MR-compatible air heater. The animal breaths a mixture of air/oxygen (2/1 L.min<sup>-1</sup>) delivered through a nose cone. The set-up also incorporates a bite bar in order to maintain the rat in a stable position. The next paragraphs describe the path used to determine the best set of parameters to obtain reproducible brain activation on our 7 T MRI scanner.

### *Functional MRI parameters: starting point*

The neurovascular coupling is similar in human and animals, making the rat an interesting choice to perform fMRI experiments on preclinical scanners. Numerous paths have been investigated to characterize the rat brain response to specific stimuli on forepaw (153-154), hindpaw (155), whiskers (156) or tail (157) using MRI. In our set-up we choose to study the brain response to electrical stimulation of the rat forepaw given the extensive literature on the subject (153,155,157).

Animals are difficult to train, and fMRI studies on awake monkeys, rats or rabbits report major motion artefacts, evidence of stress and motor cortical activation unrelated to the stimulus induced (158-159). Therefore the large majority of the preclinical fMRI studies are performed under general anesthesia. The choice of the anesthetics used has a major influence on the strength, shape and quality of the response. General anesthetics are known to induce reduced respiration rate, blood pressure, heart rate and brain metabolism compared to conscious state (160). Specific anesthetics can increase (161) or decrease (160) basal CBF and directly impact the sensitivity of BOLD fMRI to neural activity. Commonly used anesthetics for fMRI include alpha-chloralose, isoflurane, urethane, propofol and medetomidine.

We perform BOLD fMRI at 7 T using repetitions of a GE-EPI sequence (1 segment, 3 slices, slice thickness 1.2 mm, resolution 250 x 250  $\mu\text{m}^2$ , FOV 2 x 2 mm) sensitized to  $T_2^*$  (TR/TE = 1500/10 ms). These sets of parameters are commonly used when performing fMRI at 7 T (162-163) and 9.4 T (164-166). In particular, the echo time must be chosen close to the  $T_2^*$  of the tissues to increase the MR sensitivity to the BOLD signal. MRI signal is acquired at rest and during electrical stimulation.

Several studies have tried to investigate the influence of the stimulation parameters on BOLD response (164-165,167-168). In literature on rat forepaw fMRI, depending on the type and dose of anesthetics used, different stimulation durations (10 to 50 s), amplitudes (0.5 to 2 mA) and frequencies (1 to 12 Hz) are optimal for a particular set-up (165). Therefore the choice of stimulation is closely related to the choice and level of anesthetics.

To establish our fMRI set-up, we decided to start from the stimulation and anesthesia parameters described in 2008 by Zhao et al. (164). Robust contralateral activations were reported at 9.4 T. BOLD signal changes were found maximal in S1 regions (+2 % peak,  $1.25 \pm 0.17$  % in average during stimulus) for the following parameters:

Stimulation duration (s)	Pulse width (ms)	Frequency (Hz)	Amplitude (mA)
20	0.3	9	4

### Parameters optimization

The fMRI protocol is implemented on the 7 T Bruker PharmaScan MRI scanner. An initial anesthesia with isoflurane (5 % induction, 2 % stabilization) is performed in order to insert a catheter in the rat tail vein. A bolus of medetomidine (0.05 mg/kg) is injected through the catheter, isoflurane is disconnected and the freely breathing rat is installed in the magnet (no need of intubation). To maintain sedation throughout the experiment, an intravenous continuous infusion of medetomidine (0.1 mg/kg/hr) was used.

As previously reported (164), neural activity could not be detected immediately after sedation of the rat: a delay time of 45 min is needed. In practice, it is used to perform calibration of the MR system, proper shimming around the slice of interest, acquire anatomical data and adjust the GE-EPI trajectory to minimize image distortions.

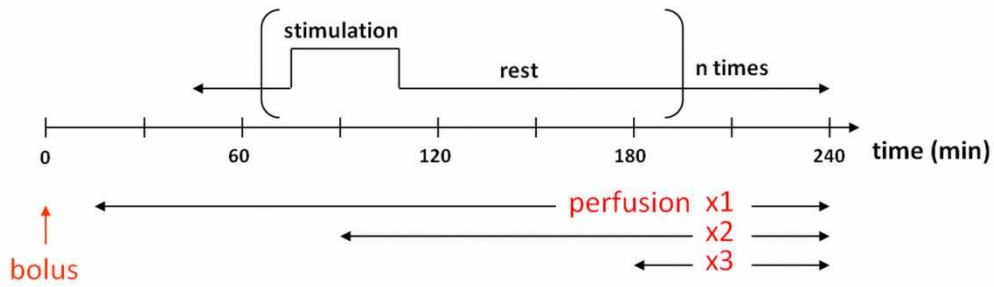


**Figure 4.3 Modification of the anesthesia infusion protocol** in order to minimize habituation of the rat. The medetomidine dose is doubled (0.2 mg/kg/hr) after 90 min and tripled (0.3 mg/kg/hr) after 180 min.

A change of the physiological condition is regularly observed 90 to 120 min after the medetomidine bolus injection when using the sedation protocol previously described. The number of activated pixels ( $p < 0.05$ , SPM8) slowly decreases between 45 and 120 min as the heart rate increases (from 40 to 90 bpm), suggesting habituation of the rat to the anesthesia dose. To avoid this problem, we modify the infusion rate according to **Figure 4.3**. Reproducible activation can be obtained between 45 min and 240 min after medetomidine induction, using two and three times increased infusion rates. To ensure minimal habituation, the delay between two consecutive fMRI experiments is also increased (from 5 to 10 min) and used to process data.

Electrical stimulation is performed by sending current through two electrodes implanted between digits two and four of the rat forepaw. The

paradigm consists in series of square pulses (width 0.3 ms) of amplitude I (4 mA) and applied at frequency f (9 Hz) for a duration  $\Delta T$  (20 s). The parameters I, f and  $\Delta T$  were tuned in the usual ranges (0-5 mA, 1-10 Hz and 10-30 s respectively) to increase the BOLD signal change detected (using SPM8) in the S1 region of the rat brain (**Figure 4.2**). After optimization, the final sets of stimulation parameters (**Table 6**) used in a single fMRI experiment at 7 T are slightly different from those described by Zhao et al.

**Table 6 List of optimized stimulation parameters to perform BOLD fMRI using medetomidine at 7 T**

Number of epochs	Stimulation duration $\Delta T$ (s)	Rest duration (s)
5	30	30
Pulse width (ms)	Frequency f (Hz)	Amplitude I (mA)
0.3	7	2

*5 epochs (stimulation units) are used to match the total scanning time (30 s baseline + 5 x [30 s stimulation + 30 s rest] = 330 s = 220 x 1.5 s TR). The experimental optimal frequency, current and stimulation duration differ from those detailed in the original implementation of BOLD fMRI using medetomidine at 9.4 T (164).*

#### *The BOLD response to electrical stimulation at 7 T*

Using the optimized stimulation parameters, a significant change in signal was observed in the rat primary somatosensory cortex S1 during forepaw electrical stimulation (**Figure 4.4**). The results obtained on 8 rats and at different times after medetomidine injection (60/165 min after bolus injection for rat #4/#6) show reliable activation in the rat S1 area.

In order to detect the activated pixels, a student t-test is performed between the data-points acquired at rest and during stimulation. The statistical t-value is calculated voxel-by-voxel. Activation maps are drawn by overlaying the t-value (thresholded to display only the significant signal changes,  $p < 0.05$ ) on the average brain signal acquired with the GE-EPI (**Figure 4.4**).

For each rat, the ROI presenting significant activation ( $p < 0.05$ ) and located in S1 is automatically extracted from the t-value maps using SPM 8 software. The BOLD signal (**Figure 4.5-A**) is averaged over the five stimuli in all the activated voxels (**Figure 4.5-B**, 8 rats, 2400 voxels). The time course obtained reveals a maximum +2.6 % increase of signal 4.5 s after beginning of the stimulation. After the first peak, the BOLD signal slowly decreases and reaches a plateau 1.4 % above the baseline signal (**Figure 4.5-B**). A faster decrease accompanies the end of the electrical stimulation and return to



baseline. We do not observe the controversial post-stimulation BOLD undershoot reported and debated in literature on fMRI (169).

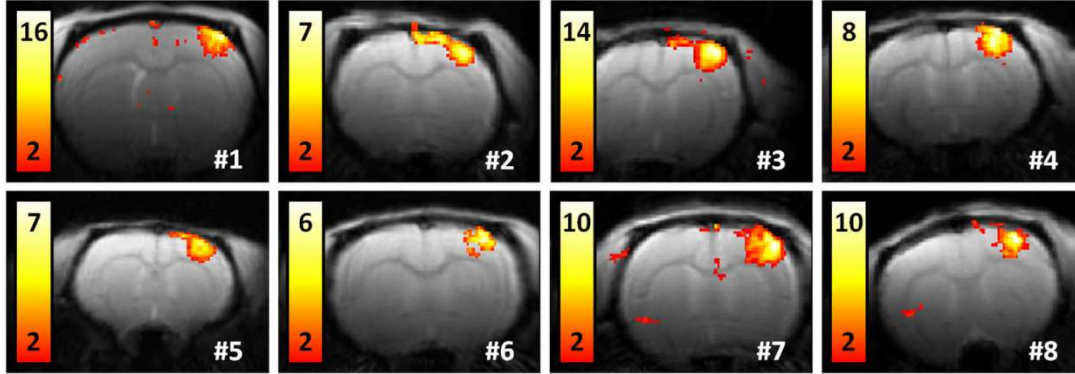


**Figure 4.4 Left-forepaw electrical stimulation-induced BOLD response in eight animals at 7 T** displayed as the *t*-value maps on the mean GE-EPI signal (only one slice per animal is shown). The spatial resolution is  $200 \times 200 \mu\text{m}$  for rat #1 and  $250 \times 250 \mu\text{m}$  for rats #2 to #8. All rats show reliable activation ( $p < 0.05$ ) in the contralateral primary somatosensory cortex in response to left forepaw electrical stimulus. The activation is less pronounced for rat #6, where imaging suffers from onion rings artefacts that might reflect eddy currents. Rats #1 and #7 exhibit also activated voxels on the edge of the brain, due to animal motion during the acquisition.

These results (shape, delayed response and time-to-peak) are in good agreement with literature on rat fMRI using forepaw electrical stimulation (163-165,170). Moreover, the +1.6 % average signal increase in the primary somatosensory cortex region is higher than the +0.6 % increase obtained in the same conditions (anesthesia, stimulation, field strength and echo time) by other groups and published in 2012 (163). The high sensitivity of our measurements (**Figure 4.5**) associated with the reproducibility of the detection of the brain activity (**Figure 4.4**) suggests that the fMRI protocol is properly calibrated at 7 T.

Because of the reproducibility of the measurements, the rat physiological condition is assumed stable throughout the experiment. Therefore the sets of stimulation and anesthesia parameters optimized for 7 T will be considered standard when performing fMRI at 7 T or higher magnetic fields, and only the imaging parameters will be adapted in order to maximize image quality and detection of neural activity. This fMRI protocol was presented to the MR community in summer 2010 (171).

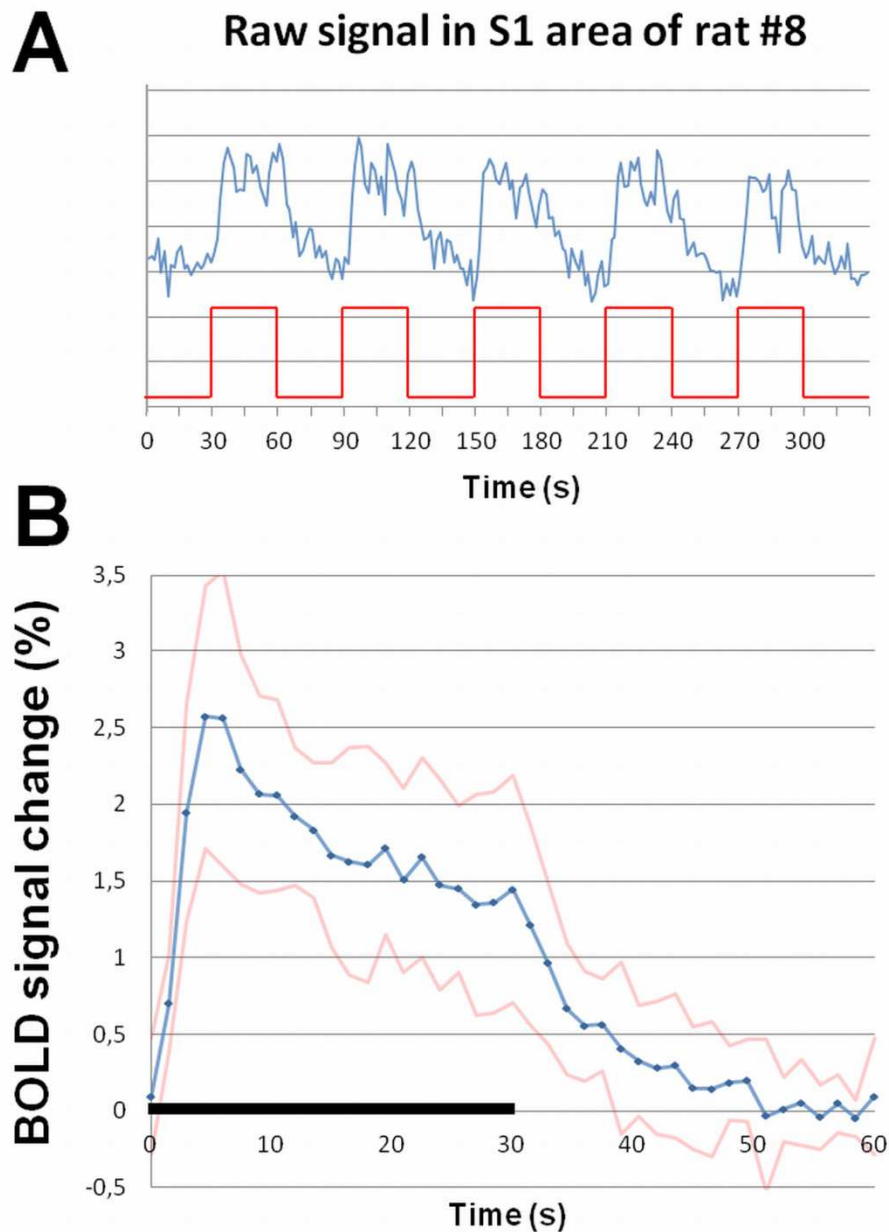


**Figure 4.5 A. BOLD time course** (arbitrary units) in the contralateral primary somatosensory cortex of rat #8 during stimulation. The paradigm is shown in red. Classical fMRI analysis correlates the BOLD data with the stimulation paradigm (multiple blocks, total scan time 5 min 30 s) in order to minimize noise on MR signal. **B.** BOLD response (%) to an electrical forepaw stimulus under medetomidine anesthesia at 7 T. The blue curve represents the BOLD response, averaged over 8 rats (~300 voxels per rat) and 5 stimulations units (indicated by the black line). The two red curves reflect the standard deviation on the BOLD response.

As seen in chapter 1, the FENSI technique repeatedly saturates a slice of interest and acquires signal from all the spins that escape the tagging plane but remain in the imaging plane. In order to obtain a significantly flow-enhanced image, the total saturation period must be long enough to allow for a large number of spins to travel from the labeling to the imaging slice. In practice, minimum saturation times on the orders of 1 s are needed to observe signal coming from the capillary bed. Moreover, two sets of images ('control'/'tag') are required to obtain a single flux weighted FENSI image. In addition to that, the repetition time must be large enough to make sure that the labeled magnetization grows back between two consecutive 'tag' and 'control' images. All these factors limit the temporal resolution achievable with FENSI.

In FENSI the intensity difference between a 'control' and a 'tag' image is directly proportional to the fraction of flowing spins per voxel (1 to 5 % of the total population of spins, see chapter 1). Although FENSI can gain signal through repeated saturation, experiments at 7 and 17.2 T show in normal cortical regions 4 to 5 % maximal signal enhancements using FENSI. The baseline flux signal when performing FENSI fMRI is only a fraction of the total MR signal.

The lack of SNR and relatively poor temporal resolution can prevent detection of rapid flux changes when performing in vivo FENSI experiments. Therefore the first attempt to perform fMRI with FENSI is the study of the response to a long stimulus (i.e. minutes) whose impact on brain metabolism is well documented.

### *FENSI fMRI: the hypercapnia challenge at 7 T*

The influence of hypercapnia (or elevated CO<sub>2</sub> level) on CBF has been extensively studied (166,172-173). In animal studies (166,173), the inhalation of a gas mixture containing a relatively small CO<sub>2</sub> level (typically 1-3 %) induces vasodilation and an increase of CBF and CBV according to Grubb's law (173). This can be used to probe cerebrovascular reactivity and reserve, two physiological parameters that can be strongly affected by many cerebral diseases (174-175). In fMRI, the hypercapnia challenge models cerebral metabolism and is used for fMRI calibration and estimation of the maximum achievable BOLD signal (176-177). In the rat cortical and subcortical regions, our previous measurements show that the microvascular CBFlux does not have any preferred direction (see Chapter 2). In those areas, CBFlux is proportional to CBF and the expected FENSI response to hypercapnia is

known. For FENSI, the long hypercapnia challenge is a first functional test and will be used for the calibration of FENSI fMRI.

During 5 minutes, the rat is exposed to normocapnic conditions (air + 2 % isoflurane). This provides the baseline CBFlux signal. The CO<sub>2</sub> level is then set to 2 % for 5 minutes and turned off for 5 minutes; this is repeated twice. MR signal is acquired during a total scan time of 25 minutes. The stimulation paradigm and FENSI results at 7 T are illustrated in **Figure 4.6**. As illustrated, the BOLD dependence of the two FENSI ‘control’ and ‘tag’ datasets can be observed (bilateral t-test,  $p < 0.05$ ), due to changes in  $T_2$  relaxation time. An average 12 % signal intensity decrease is measured in the entire brain 4 to 5 minutes after beginning of the hypercapnia challenge (**Figure 4.6-A**). However, no significant difference in CBFlux can be observed from the temporal evolution of the difference of two consecutive ‘control’ and ‘tag’ images (**Figure 4.6-B**,  $p = 0.4$ ).

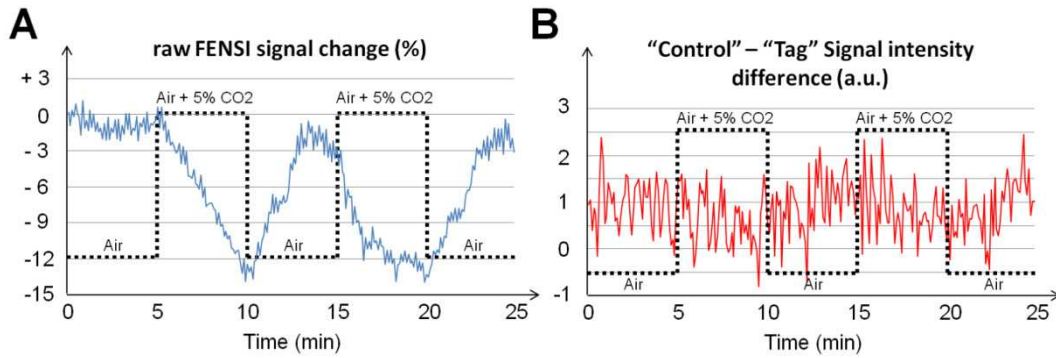


**Figure 4.6 Dynamic evolution of FENSI signal at 7 T during hypercapnia challenge** **A.** ‘Control’ and ‘tag’ datasets are interleaved during FENSI acquisition. The signal intensity (averaged on the entire brain) significantly decreases during CO<sub>2</sub> challenge (-12 %,  $p < 0.05$ ). **B.** Flux-weighted signal is obtained by the subtraction of two consecutive FENSI images. We report no significant difference ( $p = 0.4$ ) between the CBFlux calculated under normocapnic and hypercapnic conditions.

A possible explanation for this is the low temporal SNR obtained with FENSI. In addition, the stimulation blocks are too short to induce stabilization of the cerebrovascular response, as illustrated by the slow increase/decrease of BOLD signal during air/CO<sub>2</sub> inhalation (**Figure 4.6-A**). Based on the shape of the BOLD response, the use of an appropriate General Linear Model (GLM) could favor the detection of continuous signal changes between control and tag images. To ensure hypercapnic stabilization, the hypercapnia challenge is repeated with another stimulation paradigm. This time, a large FENSI dataset (150 repetitions of control and tag, TA = 30 min) is acquired after complete stabilization of the monitored physiological conditions under normal or hypercapnic conditions. The CBFlux calculated in the rat brain subject to 5 %

CO<sub>2</sub> is higher ( $p < 0.05$ ) than normal CBFlux (measured on the same rat) in cortical (+73 %), subcortical (+142 %) and highly vascularized areas (+136 %), in good agreement with literature on hypercapnia (173,176).

Based on this dataset and assuming an instantaneous stabilization of the CBF after the switch to hypercapnia, a minimum of 68 FENSI repetitions are needed in order to detect a significant change in flux in a single voxel located near the MCA. This is to be compared with the 76 FENSI images (i.e. 38 flux weighted images) acquired during the whole 5-epochs hypercapnia challenge previously detailed. In the current implementation of FENSI at 7 T, dynamic measurements cannot be characterized below 10 minutes temporal resolution.

#### *CBFlux changes during forepaw electrical stimulation at 7 T*

The same electrical stimulation parameters optimized for BOLD and previously detailed (5 epochs, 30 s stimulation/rest, pulse duration = 0.3 ms, frequency / amplitude = 7 Hz / 2 mA) are used to conduct FENSI fMRI experiments at 7 T in response to forepaw stimulus. The FENSI imaging parameters are modified in order to shorten the acquisition time and match the stimulation paradigm (TR is set to 1.5 s, and the total saturation time  $T_{SAT}$  reduced to 500 ms). 220 FENSI acquisitions (110 pairs of control/tag images) cover the 330 s stimulation paradigm. The reference image necessary for flux calculation (static tissue contribution, see Chapter 1) is approximated by the control image multiplied by the ratio  $L_{SAT}/L_{IMG}$  to obtain the FENSI signal enhancement.

Six rats were used to investigate possible changes in CBFlux when stimulating the rat left forepaw. High resolution CBFlux maps (200 x 200 x 1000  $\mu\text{m}$ , TE = 32.6 ms) were acquired on three rats. No significant changes were observed in the rat brain during stimulation ( $p = 0.6$ ), although BOLD fMRI detected an average +2 % signal increase in the primary somatosensory cortex. Lower resolution images (400 x 400 x 2000  $\mu\text{m}$ , TE = 18 ms) were acquired on the other three rats to increase SNR. Still, no changes were observed during electrical stimulation ( $p = 0.2$ ). This is in agreement with our previous results obtained during the hypercapnia challenge: rapid CBFlux changes cannot be detected at such a high temporal resolution.

Due to SNR and temporal resolution constraints, the robust fMRI protocol implemented with BOLD cannot be used in association with FENSI at 7 T. After calibration of the fMRI parameters at 7 T, the protocol was implemented at 17.2 T, where FENSI can gain signal due an increase in the  $T_1$  relaxation time, SNR and labeling efficiency.

### **IV.3 UHF, BOLD contrast and CBFlux**

We describe in this section our progress towards preclinical fMRI at 17.2 T. We quantify the influence of the type of anesthetics used on the BOLD contrast at UHF and compare the results at 7 and 17.2 T. The BOLD fMRI protocol is implemented and tested at 17.2 T. The feasibility of performing FENSI fMRI at UHF is discussed.

#### *Increased sensitivity to anesthesia at UHF*

Although numerous drugs are used in clinical surgery, their effect on brain metabolism is not well established and literature on the subject is often conflicting, suggesting a strong dependence to dosage, ventilation and other experimental parameters (178). Our objective is to monitor and try to quantify the changes in BOLD contrast induced by different anesthetics commonly used in clinical or preclinical MRI. Because magnetic field inhomogeneities have a stronger impact  $T_2^*$ -weighted images at higher magnetic field, UHF imaging is theoretically a good candidate to assess the effects of the drugs (medetomidine, ketamine/xylazine and isoflurane) on the brain blood oxygenation level.

#### *Imaging the venous system at 7 and 17.2 T*

During general anesthesia, animals are mechanically ventilated (Bioseb, Vitrolles, France) and receive a mixture of air/oxygen (similar to the fMRI experiment). All available physiological parameters (blood pressure, respiration rate, expired  $\text{CO}_2$ ,  $\text{O}_2$  saturation, temperature) are monitored and kept constant through the experiment to ensure normocapnic and normoxic conditions (for the experiments performed on the 17.2 T the  $\text{O}_2$  saturation is not monitored due to the incompatibility of the monitoring system with the strong magnetic field). Arterial blood gases (pH,  $\text{paO}_2$ ,  $\text{paCO}_2$ ) are sampled after the intubation but before the beginning of the acquisition and immediately at the end of the MRI measurement for each anesthesia condition and analyzed using a blood gas analyzer (Radiometer Copenhagen). There are no significant differences in arterial blood-gas values between different types of anesthesia protocols:  $\text{PaCO}_2$  is measured in a range of 41 – 46 mmHg,  $\text{PaO}_2$  is > 200 mmHg and pH is maintained in a 7.30 - 7.45 range. During the experiments the ventilation parameters are adjusted to maintain constant exhaled  $\text{CO}_2$ . The mean arterial systolic blood pressure is  $80.0 \pm 3.6$  mmHg under isoflurane,

69.9 ± 3.6 mmHg under ketamine/xylazine and 87.0 ± 9.3 mmHg under medetomidine.

**Table 7 Set of imaging parameters used to probe blood oxygenation level.**

Field Strength (T)	7	17.2
Field of View (mm)	25.6 x 25.6	
Matrix Size	256 x 256	320 x 320
Resolution (μm)	100 x 100	80 x 80
Slice thickness (μm)	250	200
TR / TE (ms)	300 / 12	350 / 8
Number of averages	20	14
Total scan time	25 min 36s	

*Because  $T_2^*$  is shortened at higher magnetic fields, we adjusted TR and TE to obtain comparable contrast between the tissues at both fields. After averaging, the two sets of images have similar SNR.*

Initially, the animals are anesthetized and maintained under isoflurane (2 % inspired isoflurane) during which time a series of gradient echo images is acquired. Next the animals are injected with a bolus of medetomidine (0.3 mg/kg, i. v.) or of ketamine-xylazine (100/10 mg/kg, i.p.) and the isoflurane is discontinued. A new set of gradient echo images is acquired 30 minutes after isoflurane was turned off. 6/4 animals are imaged at 17.2/7 T, 3/2 under the each of the two anesthesia conditions.

$T_2^*$ -weighted imaging is performed at 7 and 17.2 T using a gradient-echo FLASH sequence with the parameters described in **Table 7**. The gain in SNR at 17.2 T is used to enhance the spatial resolution, from 100 μm to 80 μm. The slice thickness is also reduced.

#### *Influence of magnetic field on BOLD contrast during general anesthesia*

We notice a slight change in contrast at 7 T after the injection of ketamine/xylazine or medetomidine compared to isoflurane. On the other hand, at 17.2 T the change in contrast is substantial. Coronal magnitude images obtained under the same anesthesia protocol at two different magnetic field strengths, 7 T (**Figure 4.7-A**) and 17.2 T (**Figure 4.7-B**) show higher vein-parenchyma contrast at 17.2 T. Quantitatively we can define a threshold and count the number of pixels whose magnitude on the  $T_2^*$ -weighted images are below that level (chosen 75% of average signal in the cortex). Using that criterion and for the rat imaged in **Figure 4.7**, the number of hypo-intense pixels counted at 7 T and 17.2 T are respectively 197 and 516 for the ketamine/xylazine anesthesia. Similar results are obtained under medetomidine anesthesia: we count 158 hypo-intense pixels at 7 T and 419 at

17.2 T. The number of hypo-intense pixels is not representative when comparing isoflurane at both fields, as there is almost no pixel in the cortex below that threshold at 7 T.

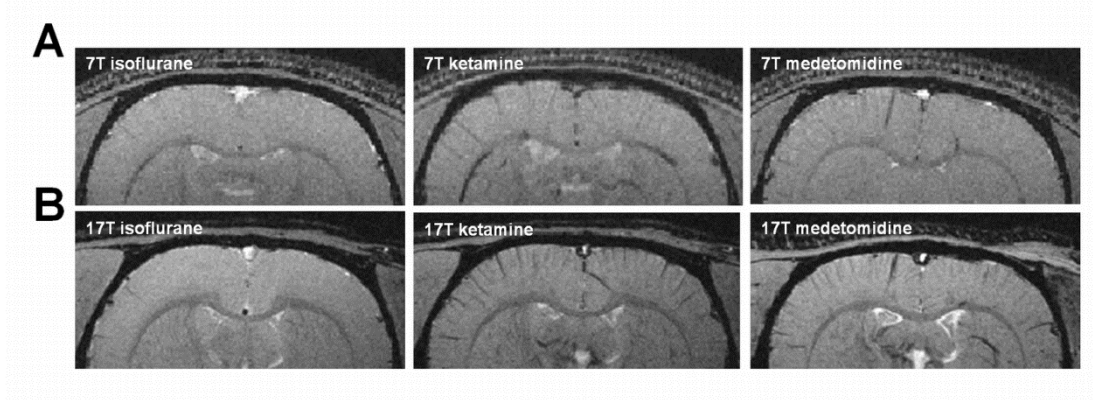


**Figure 4.7 Effect of the magnetic field strength on  $T_2^*$  contrast in rat brain images acquired in vivo under isoflurane, ketamine/xylazine and medetomidine anesthesia.** Representative FLASH images, coronal sections acquired at **A.** 7 T (100 x 100 x 250  $\mu\text{m}$  resolution) and **B.** 17.2 T (80 x 80 x 200  $\mu\text{m}$  resolution).

#### *Quantification of anesthesia effect on BOLD contrast at 17.2 T*

Coronal magnitude  $T_2^*$  images obtained on the same rat under the two different types of anesthesia (isoflurane and ketamine/xylazine) at 17.2 T are shown in **Figure 4.8-A**. The vein-parenchyma contrast under ketamine/xylazine anesthesia is higher compared to isoflurane anesthesia. Being oriented parallel to the slice plane, the blood vessels appear as dark lines. The analysis performed on the 17.2 T magnitude data reveals a dramatic contrast increase. Specifically, in analysing the signal intensity in the cortex we find 5.4 times (average over 16 slices, in 3 animals) more pixels corresponding to blood vessels, when using ketamine/xylazine anesthesia versus isoflurane anesthesia (**Figures 4.8-B**). The results obtained for each animal are shown in **Table 8**. To ascertain which anesthetic agent is mainly responsible for the difference in contrast described above we perform a second set of experiments in which we compare isoflurane with medetomidine. **Figure 4.8-C** shows the images acquired at 17.2 T, under the two conditions:  $T_2^*$  contrast obtained under medetomidine is very similar to that with the contrast obtained under ketamine-xylazine. Image analysis shows a 4.8 times increase in the number of the blood vessels counted (**Figure 4.8-D**) under medetomidine compared to isoflurane (average over 16 slices in 3 animals, see **Table 8**).



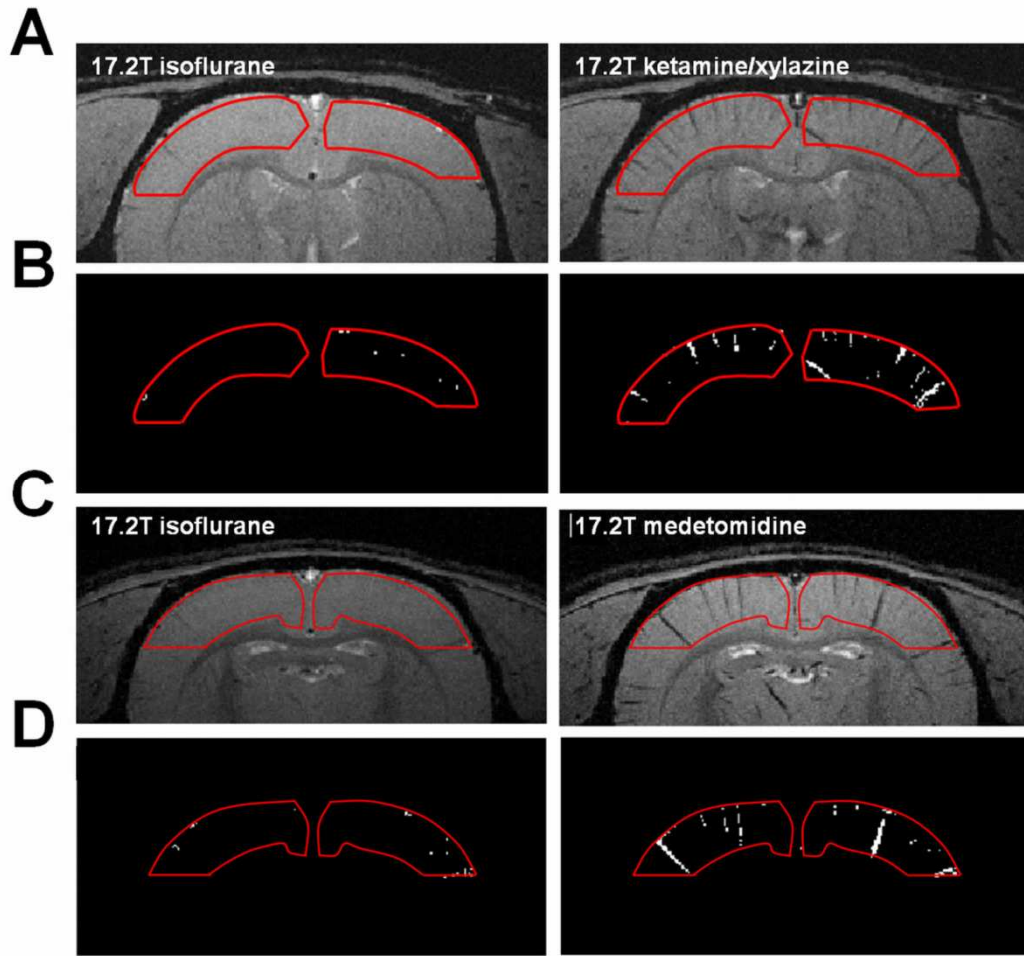


**Figure 4.8 Effect on the anesthetic agent on  $T_2^*$  contrast in rat brain images at 17.2 T: ketamine-xylazine versus isoflurane and medetomidine versus isoflurane.** Images are coronal sections (**A**, **C**) acquired at 17.2 T acquired in vivo under general anesthesia. The red ROIs show the regions used to calculate the number of pixels corresponding to visible blood vessels at 17.2 T. The pixels below the 75 % intensity threshold corresponding to these ROIs are clearly visible (**B**, **D**).

We limit our image analysis to cortical regions; however, blood vessels are also visible in sub-cortical regions, including the thalamus and hippocampus (see **Figure 4.8**). 3D acquisitions are also possible as illustrated in **Figure 4.9**, which displays the difference between images acquired under isoflurane and medetomidine anesthesia overlaid over the medetomidine image (**Figure 4.9-A**) and the 3D renderings of the difference images between isoflurane – ketamine/xylazine (**Figure 4.9-B**) and isoflurane – medetomidine (**Figure 4.9-C**). Veins and their ramifications are clearly visible on the brain surface.

**Table 8 Ratio of the number of hypo-intense pixels counted for different anesthesia conditions at 17.2 T**

Anesthetic	Rat #	Hypo-intense pixels under isoflurane	Ratio of hypo-intense pixels
Ketamine-xylazine / isoflurane	1	225	4.1
	2	238	4.4
	3	180	7.7
Medetomidine / isoflurane	4	196	7.2
	5	134	4.0
	6	241	3.4

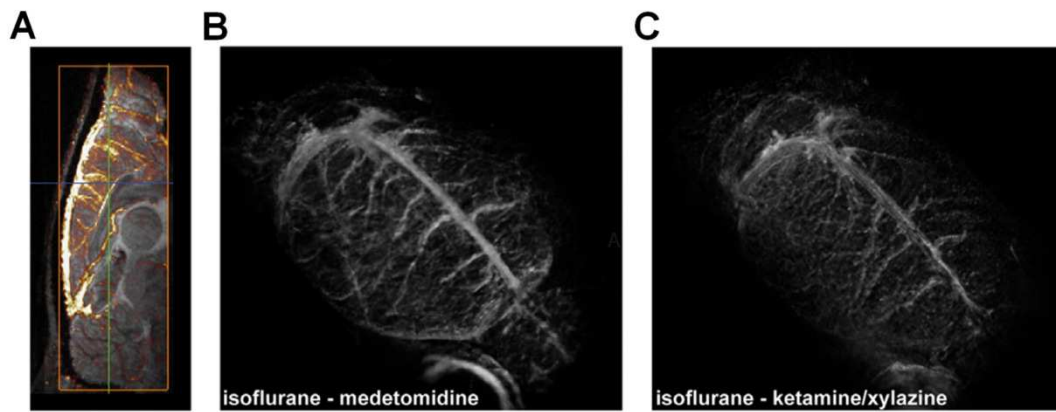


**Figure 4.9** Difference images obtained by subtracting images acquired under two anesthesia conditions at 17.2 T. **A.** isoflurane – medetomidine, sagittal plane (the image difference is superimposed on the image acquired under medetomidine) **B.** isoflurane – medetomidine 3D rendering (using Amira software) **C.** isoflurane – ketamine/xylazine 3D rendering. Acquisition parameters: FLASH flip angle 40°, TR/TE = 200/8 ms, spatial resolution 120  $\mu\text{m}$  isotropic.

#### *Anesthesia: a contrast agent at UHF*

Here we establish that the brain/vessels contrast in  $T_2^*$ -weighted images at UHF directly depends on the anesthetic agent used. Stemming from magnetic susceptibility differences between the blood in the vessels and the surrounding tissue, this phenomenon is visible to a much smaller extent at lower field strengths (7 T). Published in 2012 (178), this is the first experimental observation of this effect.

**Table 9 Effect of isoflurane, ketamine-xylazine and medetomidine on different physiological parameters**

Anesthetic agent	CBF	CMRO <sub>2</sub>	PtO <sub>2</sub>	vasodilation
<b>isoflurane</b>	+	-	+	++
<b>Ketamine-xylazine</b>	-	0	-	-
<b>medetomidine</b>	-	0	NA	--

+/-/0 = increase/decrease/no variation.

Because anesthetic agents induce profound changes in general and local brain hemodynamics and metabolism, a plausible explanation for these results is the difference in deoxyhemoglobin brain vascular content induced by the anesthesia. This difference is caused by changes in different physiological parameters (CBF, CMRO<sub>2</sub>, PtO<sub>2</sub>, vasodilatation) generated by the three anesthetics used in this study (isoflurane, ketamine/xylazine, medetomidine, see **Table 9**). The modifications observed in the vessel-tissue contrast in the UHF T<sub>2</sub>\* images are induced by changes in blood oxygen level produced by an altered metabolic load or altered CBF. Under normoxic conditions arterial blood is fully oxygenated and does not contribute to blood oxygenation level dependent (BOLD) contrast, while venous blood vessels containing de-oxygenated blood shows hypo-intense regions in the image. BOLD image contrast is enhanced at high magnetic fields, with the hypo-intense lines better visible at 17.2 T then at 7 T. BOLD contrast can be used to monitor non-invasively the blood oxygenation levels of the brain in response to central nervous system drugs that affect basal metabolism or CBF, like the anesthesia agents used in this study. Isoflurane resulted in a low contrast between cortex and venous blood vessels as seen on the 17.2 T image, probably because of CBF increase, cerebral glucose uptake decrease and decrease of deoxygenated blood in the venous blood vessels. Ketamine/xylazine and medetomidine resulted in a high contrast between cortex and venous blood vessels, probably because of CBF decrease and cerebral glucose utilization increases in some limbic structures, leading to an increase of deoxygenated blood in the venous blood vessels.

#### *Future use of UHF*

The visualization of small venous structures is very useful for studying neurological diseases in relevant preclinical animal models. A few studies demonstrated the non-invasive detection of rodent brain vasculature in magnitude T<sub>2</sub>\*-weighted images at high magnetic fields (144,179). More recent studies report high resolution imaging of brain microvasculature in rodents using susceptibility weighted imaging (180) or phase imaging (181). As shown here, due to the extreme sensitivity to Brain Blood Oxygenation Level changes

induced by anesthetic agents, UHF MR studies have the potential to screen future anesthesia drugs for their action on cerebral blood oxygenation. More generally, UHF may also play a role during preclinical screening of new pharmacological agents for their potent effect on brain oxygenation on a local basis.

Further studies are needed to establish this dependence and to fully understand the relationship between the anesthetic agent used and the vessel-tissue contrast observed. One of the main remaining questions is which anesthetic agent is the most appropriate when performing fMRI under anesthesia in rodents and non human primates, because signal intensity in  $T_2^*$  images in very high magnetic field is very variable with the anesthetic agent used.

### *BOLD fMRI: Echo Time and magnetic field dependence*

As previously detailed, the changes in BOLD signal come from the changes of the transverse relaxation time  $T_2^*$  (or the transverse relaxation rate  $R_2^*$  defined by  $R_2^* = 1/T_2^*$ ). These parameters,  $T_2^*$  and  $R_2^*$ , are field dependent and the BOLD response is very likely to change with the magnetic field. Therefore the imaging parameters must be carefully calibrated in order to improve BOLD contrast optimization during stimulation.

In a simple model assuming mono-exponential decay, the MR signal  $S$  is described by equation [4.1], where  $S_0$  can depend on the repetition time  $TR$ , the longitudinal relaxation time  $T_1$ , inflow effects and motion.

$$S = S_0 \exp(-TE * R_2^*) \quad 4.1$$

During stimulation and assuming a small change of relaxation rate  $\Delta R_2^*$ , the variation of signal  $\Delta S/S$  varies linearly with  $TE$  and becomes [4.2]

$$\frac{\Delta S}{S} = \frac{\Delta S_0}{S_0} - TE * \Delta R_2^* \quad 4.2$$

The first term  $\Delta S_0/S_0$  reflects signal changes due to artefacts (motion, flow) that are non-related to BOLD, and independent of  $TE$ . The second term is characteristic of the BOLD signal. Based on this model, several studies have tried to observe the  $TE$ -dependent changes in functional brain mapping (182). Recently, it has been used in association with multiple echo sequences to fit the variations of signal during fMRI and efficiently eliminate the non-BOLD components (183). This model also shows that the percentage signal change obtained with BOLD fMRI linearly increases with  $TE$  (184). The trade-off is a lower global SNR, according to [4.1]. In practice, the rule “ $TE \sim T_2^*$ ” is usually applied when performing BOLD fMRI. First suggested in 1994 by Menon et al.

(185) from multiple echo fMRI data acquired at 4 T, it has become a standard in fMRI experimental design.

It is also expected that high field will help increase the sensitivity to BOLD contrast. The higher the magnetic field, the higher the intrinsic SNR and the BOLD contrast, as seen in our previous anesthesia experiment. This increase has been experimentally demonstrated in 1993 at 1.5 T and 4 T by Turner et al. (186), and extended to higher fields (187-188).

*The experimental BOLD response at 17.2 T*

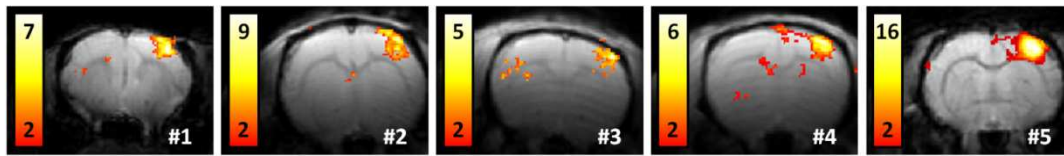


**Figure 4.10 Left-forepaw electrical stimulation-induced BOLD response in five animals at 17.2 T** displayed as the *t*-value maps on the mean GE-EPI signal (only one slice per animal is shown). The spatial resolution is 200 x 200  $\mu\text{m}$ . All rats show reliable activation ( $p < 0.05$ ) in the contralateral primary somatosensory cortex S1 in response to left forepaw electrical stimulus. Similar to fMRI studies at 7 T, several rats (#3 and 4) exhibit activated voxels in wrong locations due to motion of the animal.

$T_2^*$  dramatically decreases as the field strength increases, and the optimized TE ( $\sim T_2^*$ ) must be shortened when performing fMRI at 17.2 T. Therefore, we choose for starting point in our experiment to minimize TE (to 10 ms) once the bandwidth, FOV and matrix size are fixed. Using the stimulation and anesthesia parameters described previously, the fMRI protocol is implemented at 17.2 T.  $T_2^*$ -weighted imaging is performed using repetitions of a GE-EPI sequence (1 segment, 3 slices, slice thickness 1.2 mm, resolution 200 x 200  $\mu\text{m}^2$ , FOV 2 x 2 mm, TR/TE = 1500/10 ms). BOLD signal is acquired at rest and during electrical stimulation (five blocks constitute the stimulation paradigm).

Five rats are used to characterize the BOLD response at UHF. They all show reliable activation (**Figure 4.10**,  $p < 0.05$ ) in the S1 area, consistent with literature and with our previous fMRI data obtained at 7 T. The BOLD response is averaged in the ROIs presenting significant activation in the primary somatosensory cortex (threshold:  $p < 0.05$ ), over five rats and five stimulation blocks. The BOLD response calculated on 5 rats at UHF does not significantly differ from the BOLD response previously obtained at 7 T. In

particular, the average amplitude of the BOLD signal change (peak//plateau) is similar at 17.2 T (2//1.4 %) and 7 T (2.5//1.4 %). Only one rat (#5, see **Figure 4.10**) presented a significantly different ( $p < 0.05$ ) and stronger response to stimulation (peak: +3.4 %, plateau: +2.5 %).

This is to our knowledge the first experimental implementation of BOLD fMRI at such a high magnetic field, and further investigations are needed to study in depth the contributions of the different spin populations (venous/cortical) to the observed signal change at 17.2 T. Recent studies report direct imaging of microvascular responses in the rat whisker-barrel cortex using high resolution fMRI at 11.7 T (170). UHF fMRI is expected to help resolve the spatial heterogeneities of the hemodynamics response function.

### *SNR, temporal SNR and discussion on FENSI fMRI*

The FENSI SNR represents the relevance of the information that is extracted from the FENSI data. This parameter can be sensitized to either spatial or temporal variations.

The spatial SNR - or simply SNR - is calculated as follows. A flux map is usually generated from the FENSI dataset (N repetitions of control minus tag images are averaged). Assuming homogeneous flux, the flux-weighted signal can be averaged in a ROI. The SNR in that ROI is defined by equation [4.1]. The higher the SNR, the more homogeneous the flux in that particular area. This parameter was for instance used to compare flux distributions in the gliosarcoma and normal striatum during tumor growth.

$$SNR_{ROI} = \frac{CBFlux_{ROI}}{STD_{CBFlux \text{ in } ROI}} \quad 4.1$$

Repeating the experiment will decrease the impact of motion or physiological noise on the flux-weighted image and increase the SNR. However, the assumption that the flux is homogeneous *in vivo* is difficult to verify. Comparison of SNR might be biased by a true spatial dependence of cerebral blood flux. Also, the temporal flux dynamics are lost, and this estimator is a poor indicator of the goodness of FENSI or ASL sequences applied to fMRI.

In practice one will rather calculate (for FENSI as well as for ASL) the temporal SNR (or tSNR). To do so, N flux maps are generated (one for each repetition/time-point). The tSNR is calculated voxel-by-voxel, and is defined by the time-averaged flux signal divided by the temporal standard deviation in that voxel, as seen in equation [4.2].

$$tSNR = \frac{CBFlux(x,y)}{tSTD_{CBFlux(x,y)}} \quad 4.2$$

Increasing the number of repetitions will only increase the accuracy of the term CBFlux (x,y) in [4.2]. As opposed to the SNR, the tSNR reflects the real-time flux-weighted signal variations and is a good indicator of the number of control/tag repetitions required in order to obtain a relevant flux measurement. At 7 T, our experimental FENSI data indicate for instance a tSNR of  $0.4 \pm 0.2$  in GM, which is not sufficient to detect CBFlux changes during electrical stimulation. Increasing the duration of the stimulation (as in the hypercapnia challenge) can make the FENSI technique suitable to quantify the blood flux changes in the brain.

The implementation of FENSI at UHF enhances significantly (+160 %) the temporal SNR of the technique, indicating that fewer repetitions are needed to obtain a proper estimation of the true CBFlux at 17.2 T than at 7 T. After optimization of the FENSI imaging parameters at 17.2 T, the temporal SNR can reach up to 1.2 in the cortex. This is similar to temporal SNR values obtained with VS-ASL, PASL and CASL techniques (59,106,189). All of these methods were proven capable of detecting reliable activation during stimulation based on CBF measurements.

These results are also consistent with the work of Ouyang et al. who recently implemented the FENSI technique on a 3 T clinical scanner and performed quantification of the cerebral blood flux change in response to a visual task (85). They report a temporal SNR on the order of 0.8 in GM, in good agreement with our findings. Their results, averaged over four subjects and five stimulation blocks (8 Hz checkerboard, TA = 5 min), indicate a  $+73 \pm 13$  % flux increase in the activated V1 region.

### *Perspectives on the use of FENSI fMRI at UHF*

In this chapter we have shown that the FENSI technique is suitable to detect and quantify flux changes in response to an extended hypercapnic challenge. Our findings indicate that the SNR obtained with FENSI (even at ultra high field) is not enhanced compared to conventional ASL methods (PASL, CASL, VS-ASL). Additional work on technical and methodological developments is needed to investigate in depth the mechanisms of neurovascular coupling underlying BOLD and perfusion fMRI. Future developments at NeuroSpin include the conception and realization of an actively decoupled transmit-receive system to further enhance the SNR at UHF. Regarding the FENSI technique, background suppression pulses are currently being investigated to reduce the impact of physiological noise and

motion. Based on the tSNR calculated with FENSI at UHF, we believe that the characterization of the CBFlux changes in response to short forepaw electrical stimulation and direct comparison with BOLD fMRI is within reach.

The lack of accurate measurements at high temporal resolution suggests that the method would benefit from longer acquisition times, preventing however dynamic measurements. At longer time scales, CBFlux maps can provide quantitative and precise intelligence on brain metabolism at capillary level, which cannot be obtained with BOLD studies. This is of prime interest for pharmacological, cancer and metabolism studies which do not require instantaneous measurements of brain activity but need to quantify in a reliable way the local changes induced by a drug, a treatment or a tracer. The CBFlux is indeed a true quantitative physiological marker of the brain activity.





## V. Mapping brain microvasculature and its orientation with FENSI

The interested reader will refer to this chapter as a guide to the implementation of the Flow Enhanced Signal Intensity method. Here are discussed the influence of the different relevant imaging parameters on the signal enhancement, and how to sensitize the method to the appropriate range of velocities.

In the first sections we remind of the difficulties encountered by non-invasive arterial spin labeling techniques to accurately assess the brain vasculature at capillary level, in cases of elevated or undetermined transit times. As opposed to conventional PASL or CASL, VS-ASL methods can encode flux based on blood velocity rather than spatial location, such as the circle of Willis or the MCA.

With FENSI the signal enhancement depends on four main parameters detailed in this chapter. Adjusting these different parameters can help sensitize the FENSI flux-weighted image to slow flows, and provide quantitative intelligence on the inner mechanisms of the microvascular network by removing the intravascular component of blood flow from the control/tag subtraction image.

In addition, the blood longitudinal relaxation  $T_{1b}$  of the labeled spins during  $T_{SAT}$  will prevent an accurate detection of the very small flows and must be kept in mind when performing FENSI. We also suggest a different use of the FENSI technique that can be sensitized to the regional flowing spins fraction, when all the spins equally contribute to the signal enhancement, regardless of their velocity.

In the second part of this chapter, the directionality of microvascular blood flow is investigated, as ideal flux quantification assumes a plug flow orthogonal to the labeling plane. Different problems can arise with FENSI, depending on the microvessels orientation and spatial resolution.

Our measurements indicate that the FENSI technique is able to detect preferential flow directions near large blood vessels and suggest that microvasculature can be considered isotropic elsewhere. The possibility to map the precise orientation of microvascular flux with FENSI is considered.

## **V.1 Velocity range and microvasculature**

We detail in a first section the range of velocities to which conventional ASL sequences and FENSI can be sensitized, and its dependency on the different FENSI imaging parameters. The influence of flow orientation on CBF<sub>Flux</sub> calculation is discussed in a second section.

### *Clinical standards using conventional ASL and limitations*

Classically, PASL, CASL and PCASL sequences used on routine on 1.5 or 3 T clinical scanners label the blood while in the arteries at the level of the circle of Willis and quantify the loss of signal introduced by this inversion of magnetization in a slice of interest in the brain. Therefore, to maximize the perfusion-weighted contrast, acquisition timings must be finely tuned.

In particular, the delay between the labeling of blood and the MR signal acquisition must match the blood transit time from the circle of Willis to the capillary network. This delay depends on the blood velocity in the vascular network, but also on the distance between the labeling and imaging slabs and on the particular path taken by the blood molecules.

In practice, this delay is optimized to maximize the perfusion-weighted signal in the gray matter. Depending on the study, these delays vary from 1 to 1.5 s (189-190) in order to allow the blood that has been labeled in the neck to enter the imaging slice (typical distances label/image = 6-10 mm). A correction factor must also be inserted in the CBF calculus formula when performing multi-slice ASL, and can introduce a quantification bias when the blood velocity has not been properly estimated.

The necessity to introduce these delays prevents accurate measurements of slow or collateral blood flows in pathological cases, such as stroke or dementia. In healthy subjects, CBF calculations can also be made difficult for older individuals or in particular regions of slow flow, such as white matter (13,191). These problems can be bypassed by using multiple inversion times ASL sequences such as Hadamard-encoded CASL (192) to estimate the bolus arrival times prior to the ASL acquisition and/or acquire CBF maps at various post-labeling delays. These processes are however time consuming and the common practice consists in increasing the labeling durations and post-labeling delays when willing to quantify slow flow.

## Velocity-Selective ASL

Velocity-selective ASL (59-60) was first proposed to answer the problem of quantification of perfusion in the particular conditions of slow and collateral flow. The technique labels all the spins flowing above  $v_c$  (cut-off velocity) without any spatial selection, and acquires signal from the spins with velocities below  $v_c$  (see Chapter 1). VS-ASL was successfully applied at 3 T (60), and provides CBF maps with a SNR similar to PASL or CASL methods.

Quantification of CBF with VS-ASL necessitates however a fine tuning of the parameter  $v_c$  (59). Therefore multiple sets of acquisitions are required to accurately calculate perfusion in regions of both normal and slow flow. The same imaging parameters cannot accurately describe the cases of slow and regular blood flows.

### *The FENSI enhancement versus blood velocity*

As for the other techniques, the flux-weighted signal obtained with FENSI depends on many parameters, including blood velocity  $v$  and saturation duration  $T_{SAT}$ . The relationship between the FENSI signal enhancement  $E$  and the blood velocity  $v$  is described by equations [1.2] and [1.5] in Chapter 1 and illustrated in **Figure 5.1**. For a given velocity, four imaging parameters have a direct impact on the enhancement  $E$  obtained with FENSI. These are the saturation duration  $T_{SAT}$ , the imaging slice thickness  $L_{IMG}$ , the FENSI saturation slice thickness  $L_{SAT}$ , and the post-FENSI saturation slice thickness  $L_{PS}$ .

The trapezoidal shape of the enhancement versus velocity ( $E/v$ ) curve remains unchanged when tuning  $L_{IMG}$  and  $L_{PS}$  (**Figure 5.1-A**). Increasing the imaging slice thickness  $L_{IMG}$  allows for the fastest spins to remain longer in the imaging slice and build up additional saturation before they escape: the maximum enhancement  $E_{MAX}$ , defined by equation [5.1], is increased. This does not affect spins with low velocity.

$$E_{MAX} = \frac{L_{IMG} - L_{PS}}{2 * L_{SAT}} \quad 5.1$$

When  $L_{PS}$  increases, the effective imaging slice thickness  $L_{IMG,eff} = (L_{IMG} - L_{PS})$  diminishes and less saturation is built up in the tag image. Some of the spins with low velocity do not reach the imaging slice. The result is an overall lower FENSI enhancement and a reduced range of velocities (**Figure 5.1-A**). One will in practice choose  $L_{PS}$  as small as possible to maximize the SNR of the flux-weighted image. However, this parameter must be chosen large enough to

eliminate the static tissue contribution to flux that can be caused by direct saturation, imperfect saturation profiles or diffusion.

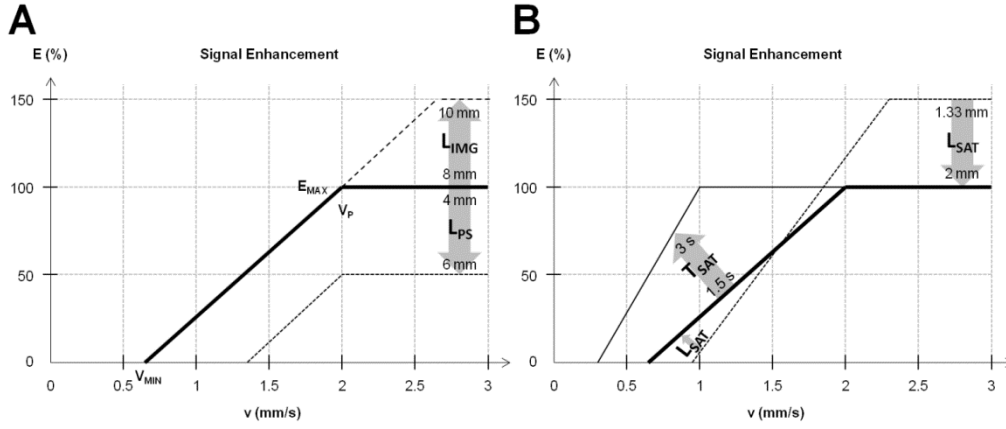


**Figure 5.1 Influence of  $L_{IMG}$ ,  $L_{PS}$ ,  $T_{SAT}$  and  $L_{SAT}$  on the theoretical enhancement  $E$  (%) obtained with FENSI for different blood velocities  $v$  (mm/s).** The bold line represents the theoretical enhancement calculated with the following imaging parameters:  $T_{SAT} = 1.5$  s,  $L_{SAT}/L_{IMG}/L_{PS} = 2/8/4$  mm. **A.** After  $T_{SAT}$ , only the spins located in the effective imaging slice thickness ( $L_{IMG} - L_{PS}$ ) contribute to the control/tag signal. Increasing  $L_{IMG}$  to 10 mm (dashed line) allows for more spins to accumulate and increases  $E_{MAX}$ . On the contrary, increasing  $L_{PS}$  to 6 mm (dotted line) reduces  $E_{MAX}$  and prevents slow spins from reaching the imaging slice in time. **B.** Increasing  $T_{SAT}$  to 3 s (plain line) will allow for slower spins to reach the slice.  $E_{MAX}$  remains unchanged, but is reached for smaller velocities. Increasing  $L_{SAT}$  from 1.33 mm (dotted line) to 2 mm (plain bold line) shifts the velocity range  $[V_{MIN} - V_P]$  towards slow flows, but reduces  $E_{MAX}$ .

Keeping all the other parameters constant, increasing the labeling duration  $T_{SAT}$  makes the FENSI sequence sensitive to the spins traveling at low velocity that now have the time to enter the imaging slice (**Figure 5.1-B**). For these spins to contribute to the FENSI signal loss, the minimum distance to travel  $L_{MIN}$  is defined by  $(L_{PS} - L_{SAT})/2$ , from the edge of the FENSI saturation slice to the edge of the post-FENSI saturation slice. And the minimum velocity that can be detected with FENSI can be calculated via equation [5.2].

$$V_{MIN} = \frac{L_{MIN}}{T_{SAT}} = \frac{L_{PS} - L_{SAT}}{2 * T_{SAT}} \quad 5.2$$

Similarly,  $T_{SAT}$  affects the threshold velocity  $v_P$  where the  $E/v$  plot reaches the plateau, defined by equation [5.3]. The fastest spins on the edge of the saturation slice escape indeed the imaging slice after having traveled  $(L_{IMG} - L_{SAT})/2$ , and are being replaced by new spins. Therefore only a fraction of the spins flowing with velocity  $v > v_P$  contribute to the FENSI enhancement.

$$V_P = \frac{L_{IMG} - L_{SAT}}{2 * T_{SAT}} \quad 5.3$$

Finally, increasing  $L_{SAT}$  will decrease both  $v_{MIN}$  and  $v_P$ , and sensitize the sequence to low velocities. The trade-off is a decrease of the maximum enhancement  $E_{MAX}$  (**Figure 5.1-B**). In addition, FENSI measures the quantity of spins flowing through the saturation slice, and  $L_{SAT}$  reflects the transverse size of a single voxel in the final CBFlux map. Increasing  $L_{SAT}$  will degrade the resolution of the flux image. **Table 10** summarizes the different effects and side-effects of tuning  $L_{IMG}$ ,  $L_{PS}$ ,  $T_{SAT}$  and  $L_{SAT}$  when trying to sensitize the FENSI method to slow flows (high  $E_{MAX}$  for small  $v_{MIN}$  and  $v_P$ ).

**Table 10 Methods to improve the detection of slow flows with FENSI**

	$v_{MIN}$	$v_P$	$E_{MAX}$	Drawbacks
<b>Increasing <math>L_{IMG}</math></b>	0	+	+	Artefacts (ears), Resolution
<b>Reducing <math>L_{PS}</math></b>	-	0	+	Direct saturation, diffusion, motion, noise
<b>Increasing <math>T_{SAT}</math></b>	-	-	0	Longer acquisition time, $T_1$ relaxation
<b>Increasing <math>L_{SAT}</math></b>	-	-	-	Loss of spatial resolution

*The four parameters have to be carefully tuned in order to obtain a significant signal enhancement without suffering from direct saturation ( $L_{PS}$ ), blurring ( $L_{IMG}$ ,  $L_{SAT}$ ) and within reasonable acquisition times ( $T_{SAT}$ ).*

In practice, one will first choose  $T_{SAT}$  to be sensitive to the appropriate range of velocities.  $L_{SAT}$  is dictated by the resolution of the final parametric flux map. Depending on the brain geometry and precise locations of the FENSI flux measurements, the imaging slice thickness  $L_{IMG}$  will be chosen 3 to 4 times larger than  $L_{SAT}$  in order to obtain a significant FENSI enhancement but small enough to avoid contamination of the flux-weighted image by artefacts.  $L_{PS}$  must account for imperfection of saturation and can be chosen 1.2 to 1.8 times larger than  $L_{SAT}$ .

### Microvascular flux

**Figure 5.1** illustrates how FENSI can be sensitized to slow velocities and access microvasculature (with typical blood velocities on the orders of 1-2 mm/s). The presence of a plateau also indicates that FENSI is equally sensitive to all the spins that flow through the saturation slice with a velocity whose longitudinal component is above the threshold  $v_P$ . Without any correction, it is therefore likely that flux-weighted images are contaminated by

macrovasculature and intravascular signals, and do not reflect the microvascular network.

In this manuscript, we use a simple method to sensitize our signal to microvasculature only, by introducing several saturation pulses inside the preparation module of the control image (or control tags, see **Figure 5.2-A**). By doing so, fast flows are labeled in both control and tag images. The maximum enhancement  $E_{MAX}$  is not affected by  $T_{SAT}$  (see **Table 10** and equation [5.1]) and the signal intensity difference control – tag (proportional to  $E_{TAG} - E_{CONTROL}$ ) characterizing flux is not sensitive to the fast spins (**Figure 5.2-B**).

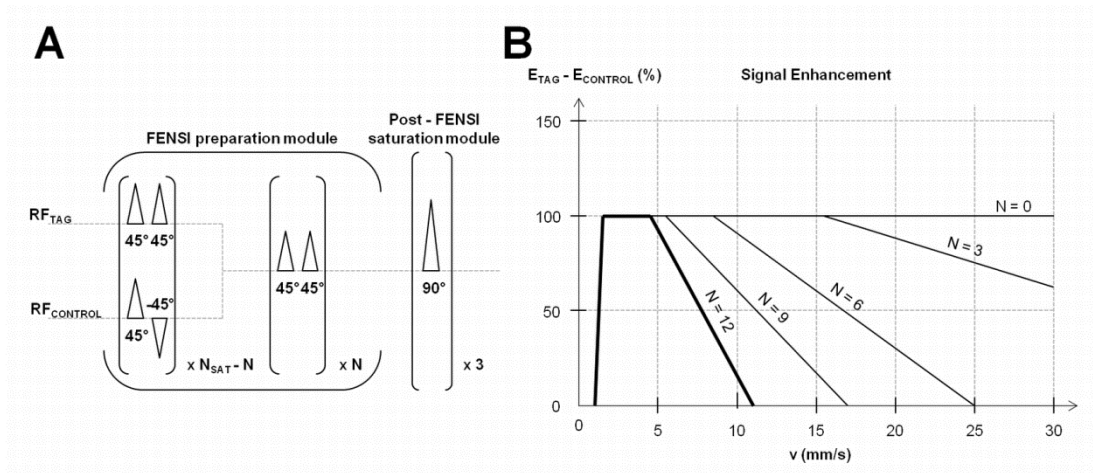


**Figure 5.2 Influence of the number of  $45+45^\circ$  FA pulses  $N$  introduced in the control image on the  $E/v$  plot. A. Diagram of the radio-frequency pulse sequence of the FENSI preparation module set in tag and control mode. The module set in tag mode applies  $N_{SAT}$  pairs of  $45^\circ+45^\circ$  FA pulses on the labeling slab. In control mode, only the last  $N$  pairs of pulses (named control tags) are conserved and pairs of  $45^\circ-45^\circ$  FA pulses are used to 1.balance MT effects and 2.immediately refocus the  $45^\circ$  flipped spins. The total duration  $T_{SAT}$  of the FENSI preparation module is unchanged between control and tag. B. The  $E/v$  plot highlights the impact of a few number of control tags on the theoretical FENSI enhancement.**

Our calculations show that only a few pulses are required in the control image in order to account for flows on the order of 10-30 mm/s corresponding to the spins located in the large arteries and veins. In practice, one can estimate the desired velocity cut-off threshold  $V_C$  and calculate the corresponding saturation time  $T_{SAT-CONTROL}$  based on equation [5.4].

$$T_{SAT-CONTROL} = \frac{L_{IMG} - L_{SAT}}{2 * V_C} \quad 5.4$$

Based on the duration  $\Delta T$  of a single pair of  $45^\circ/45^\circ$  FA pulses (typically 15-20 ms), one can adjust the FENSI parameters, so that the number of control tags  $N$  closely matches the ratio  $T_{\text{SAT-CONTROL}} / \Delta T$ .

This number depends via [5.4] on the imaging and labeling slice thicknesses, but also on the velocity cut-off. It can be reduced when going from preclinical to clinical research, decreasing the amount of energy deposited on the human brain.

### *Blood longitudinal relaxation time $T_{1b}$ and FENSI*

$T_{1b}$  plays an important role in ASL and FENSI techniques as it provides an estimate of the time the labeling remains efficient. In ASL sequences, quantification of CBF requires knowledge on  $T_{1b}$  to compensate for the blood transit time between the labeling and imaging positions. The correction factor varies with the specific location of the slice when performing multi-slice ASL. FENSI is by design dedicated to single-slice imaging. For FENSI,  $T_{1b}$  has a major impact on different imaging parameters, such as TR and  $T_{\text{SAT}}$ .

The introduction of the parameter  $T_{1b}$  in the Bloch equations affects the CBFlux calculation presented in Chapter 1. The radio-frequency concatenation used to label blood in the FENSI technique mimics a continuous saturation of length  $T_{\text{SAT}}$ . Depending on the blood velocity, the spins that contribute to the FENSI signal enhancement have been labeled at different times before MR acquisition, and have relaxed differently. The influence of  $T_{1b}$  on the theoretical FENSI enhancement  $E$  versus blood velocity  $v$  is illustrated in **Figure 5.3** for different  $T_{1b}$  and  $T_{\text{SAT}}$  values. Large velocities are not affected by  $T_{1b}$  relaxation. However, the FENSI sensitivity to slow flows can be greatly diminished when  $T_{\text{SAT}}$  approaches  $T_{1b}$ . Going to higher magnetic fields will increase  $T_{1b}$ , and increase the sensitivity of the FENSI technique to slow flows (achievable with long  $T_{\text{SAT}}$ ).

The increase in  $T_{1b}$  has also an influence on the repetition time TR separating two successive repetitions. FENSI acquisitions are usually interleaved between control and tag mode to minimize physiological noise. TR must be chosen large enough so that the blood labeled during the tag acquisition does not contaminate the signal from the control image, resulting in an overall lower flux-weighted intensity.



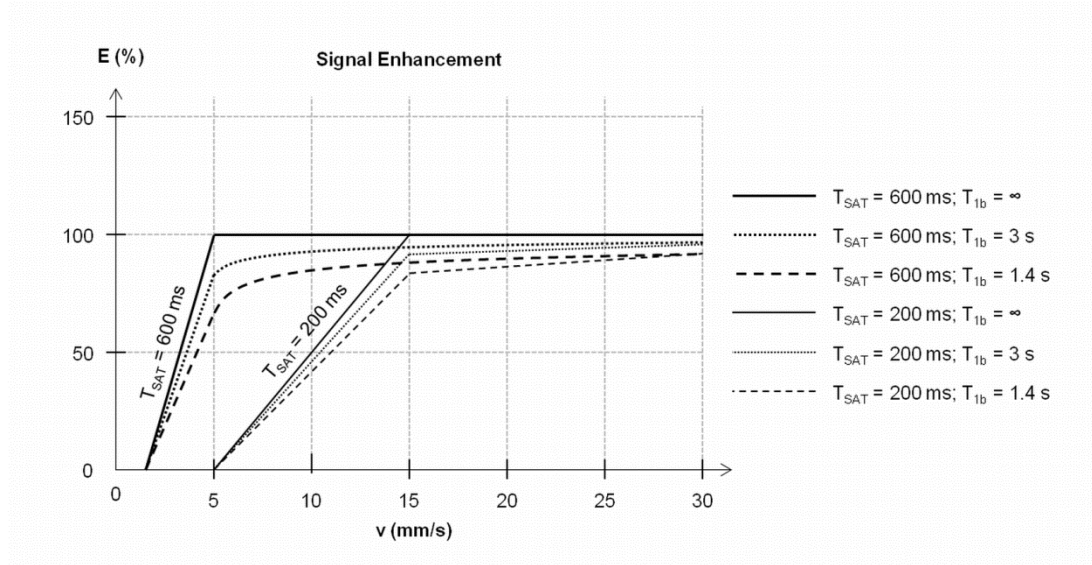


**Figure 5.3 Influence of  $T_{SAT}$  and  $T_{1b}$  on the FENSI signal enhancement** obtained with  $L_{IMG}/L_{SAT}/L_{PS} = 8/2/4$  mm. There is almost no  $T_{1b}$  effect for large velocities ( $v > 30$  mm/s). The enhancement plateau (plain line,  $E = 100\%$ ) is reached and its magnitude does not depend on  $T_{1b}$ . Relaxation of spins with  $T_{1b}$  mainly impacts slow velocities, as fast spins are continuously replaced in the imaging slice by new spins recently labeled. The influence of  $T_{1b}$  on slow flows increases with  $T_{SAT}$  (see bold lines). The FENSI enhancement diminishes with  $T_{1b}$ , suggesting FENSI benefits from the use of UHF.

### Utilization of the FENSI method

We have shown here how the FENSI method can be sensitized to various blood velocities. These results suggest that the FENSI parameters can be adapted for the experiment to answer a specific question (or pathology) regarding slow flows. Compared to ASL, FENSI can access smaller velocities and obtain signal from microvessels, such as arterioles, capillaries and venules.

As discussed in chapter 1, FENSI can be easily sensitized to the flowing spin fraction by tuning  $L_{IMG}$ ,  $L_{SAT}$  and  $T_{SAT}$ . The maximum signal enhancement  $E_{MAX}$  is reached for all velocities above the plateau defined by [5.3]. Above this threshold, the flux-weighted image will not reflect flux but differences in the local flowing spins fraction.

On the other hand, it is possible to adjust the FENSI parameters to make the signal enhancement depend with the velocity  $v$ .  $E$  varies indeed linearly with  $v$  on the range  $[v_{MIN} - v_P]$ . This range of velocities can be

maximized by tuning  $L_{IMG}$ ,  $L_{PS}$  and  $T_{SAT}$  based on equation [5.5] and centered on the position  $v_L = v_{MIN} + (v_P - v_{MIN})/2$  that depends on  $L_{SAT}$  via [5.6].

$$V_P - V_{MIN} = \frac{L_{IMG} - L_{PS}}{2 * T_{SAT}} \quad 5.5$$

$$V_L = \frac{L_{IMG} + L_{PS} - 2 * L_{SAT}}{4 * T_{SAT}} \quad 5.6$$

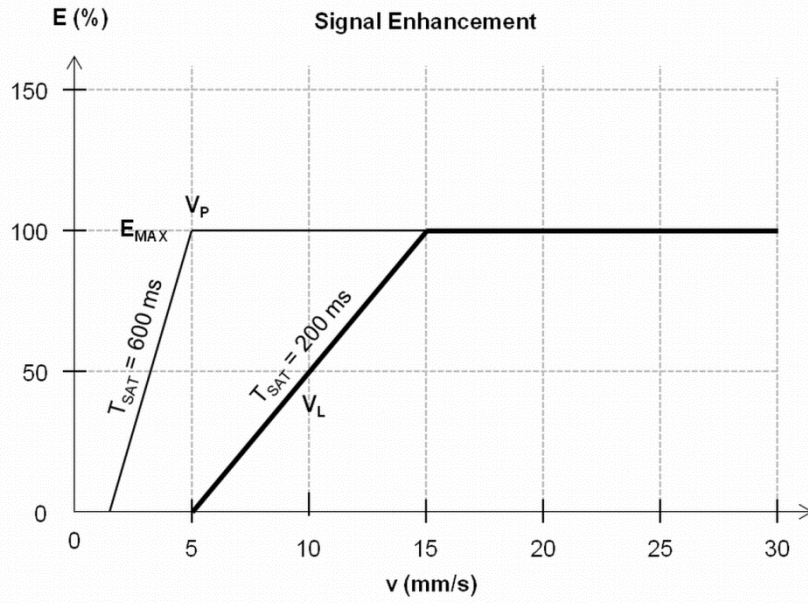


**Figure 5.4 FENSI enhancement versus blood velocity with the following parameters:  $L_{SAT}/L_{IMG}/L_{PS} = 2/8/4$  mm.** Assuming relevant blood velocities in the range  $[5 - 15 \text{ mm/s}]$ , using a 200 ms labeling duration (bold line) will sensitize the FENSI sequence to the spin velocity differences around  $V_L = 10 \text{ mm/s}$ . By increasing  $T_{SAT}$  to 600 ms, all the spins flowing above  $V_P = 5 \text{ mm/s}$  equally contribute to the signal enhancement. The method is then sensitive to the local flowing blood volume (or flowing spins fraction).  $T_{1b}$  was considered infinite in these simulations.

Based on equations [5.5] and [5.6] and provided a constant flowing spins fraction on the range  $[v_{MIN} - v_P]$ , the Flow Enhancement Signal Intensity method can be used to detect and quantify small velocity changes around  $v_L$  (Figure 5.4).

FENSI differentiates from PASL, CASL and VS-ASL sequences by saturating all the spins in the slice of interest. It labels static tissue as well as arteries, veins and the whole capillary network. Depending on the particular

set of imaging parameters (see previous section), FENSI can then be sensitized to: large velocities (small  $T_{SAT}$ ), small velocities (long  $T_{SAT}$  in association with some saturation pulses in the control image) or regional CBV through a wide range of velocities (long  $T_{SAT}$ ).

## V.2 Probing flow orientation

In this section we investigate the possibility to obtain directionally-sensitive flux measurements using the FENSI sequence, and to probe the orientation of the microstructures of interest. The development of a FENSI flux tensor is discussed.

### *Influence of blood flow orientation on flux measurement*

Flux calculation with FENSI is illustrated in Chapter 1 based on the ideal case of plug flow oriented orthogonal to the labeling plane (**Figure 1.6**). Experimental protocols deal however with tissues, tumors and tortuous media. In a given voxel, vessels, micro-vessels and capillaries do not necessarily share the same orientation. There might not be any privileged direction to CBFlux. For instance, microvasculature can be considered isotropic in most of the brain tissues. Even in the particular case of a large vessel, it is likely that its orientation is not perpendicular to the saturation.

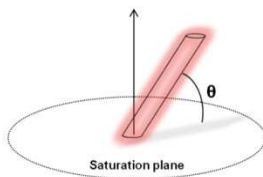


**Figure 5.5 Influence of microvessel orientation and spatial resolution on CBFlux. A.** *Illustration of the angle  $\theta$  between the blood flow and the FENSI labeling plane. Only velocity components orthogonal to the saturation plane contribute to the FENSI signal enhancement.*

This has a direct impact on the calculation of CBFlux. We consider here the case of blood flow uniformly oriented with an angle  $\theta$  with regards to the labeling plane (**Figure 5.5**). Equation [1.5] is easily modified in order to introduce the longitudinal component of blood velocity  $v_z$  given by  $v_z = v \cdot \sin \theta$ . The blood velocity  $v$  is replaced by its longitudinal component  $v_z$  in all the following equations, modifying therefore the range of velocities FENSI is sensitive to.

Due to symmetry of the problem, we will only investigate here half of the velocity space:  $\theta \leq 90^\circ$ . Intuitively, if the blood remains inside the labeling plane ( $\theta = 0^\circ$ ), there is no possibility to detect its contribution to the signal acquired in the imaging slice, regardless of its velocity.

On the other hand,  $\theta = 90^\circ$  is the ideal case. All the spins are flowing orthogonal to the labeling plane. The imaging slice acts as an extension of the labeling plane where labeled spins can accumulate. The signal obtained from the thick imaging slab (8-10 mm) perfectly reflects the vasculature from the labeling slice (0.5 – 2 mm). Similarly, blood flows with relatively large angles ( $60^\circ < \theta < 90^\circ$ ) do not cause major perturbations on CBFlux calculation ( $0.85 < \sin \theta < 1$ ).

Problems can arise from vessels and microvessels oriented with low and medium angles ( $15^\circ < \theta < 60^\circ$ ). First, calculation of CBFlux is not accurate because the FENSI enhancement vary with the orientation of blood flow ( $0.25 < \sin \theta < 0.85$ ). In addition, two phenomena can occur, depending on spatial resolution. When the voxel size is larger than the vessel/microvessel diameter (most common case in practice), spins accumulate within the voxel. The FENSI signal enhancement exceeds the theoretical predictions, introducing an overestimation of CBFlux. If the voxel size is close to the diameter of the structure of interest, the flux-weighted image will reflect hyperperfused areas in the voxels where labeled spins have flown. These areas do not necessarily match the position of the original labeling. Instead, the CBFlux map reflects the projection of the flow extension through the imaging slice. High resolution FENSI acquisitions do not help resolving microstructures in anisotropic media.

In theory, the vessels and microvessels oriented at very low angle ( $\theta < 15^\circ$ ) with regards to the labeling plane can induce major distortions in the flux-weighted images. In practice, these do not contaminate the signal. The labeling efficiency of such structures is very poor and the post-FENSI saturation pulses used to eliminate static tissue ensure a minimum gap between the labeling and imaging slices.

#### *In vivo CBFlux measurements in multiple directions*

The directionally sensitive character of FENSI is investigated experimentally in two different regions of the rat brain. One Volume of Interest (VOI) contains cortical gray matter only. The other VOI is deeper in the brain and crossed by a large artery. Six CBFlux maps of a rat brain are acquired along 6 equally distributed orientations in the plane ( $0^\circ - 180^\circ$ , see **Figure 5.6-A**). Imaging and labeling planes are rotated ( $30^\circ$  steps) around the z-axis but all contain the same VOI at their intersection for meaningful

comparison, as illustrated by the yellow box in **Figure 5.6-A**. Angiography (FLASH, TE/TR = 2.4/15 ms, NA = 2, res. 120 x 120 x 400  $\mu\text{m}^3$ , matrix 256 x 192 x 80) is also performed to determine the orientation of the blood vessels crossing the labeling plane.

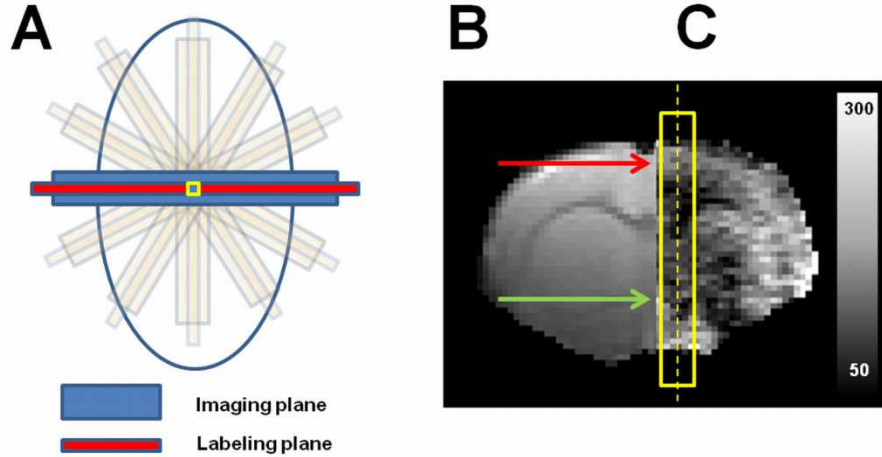


**Figure 5.6 FENSI imaging protocol implemented to probe the directionality of microvascular flux in the rat brain.** **A.** The experiments measure the blood flux passing through the labeling plane rotated around the z-axis (0;30;60;90;120;150°). Comparison provides information on the microvasculature orientation in the yellow VOI. **B.** Reference image and **C.** CBFlux map [ $\mu\text{L}/\text{min}/\text{cm}^2$ ] calculated with FENSI (coronal view, 0° angle). The yellow axis and box represent respectively the rotation axis and VOI used for comparison of flux in different orientations. The red/green arrows indicate the regions of the VOI containing gray matter/a large vessel.

**Figure 5.6** shows the reference image (**B**) used for FENSI calculation and the corresponding CBFlux map (**C**, coronal view). The yellow axis and box represent the rotation axis and VOI used for comparison, respectively. Red/green arrows indicate the regions containing gray matter/a large vessel (based on angiography). Mean CBFlux values and standard deviations in these regions for the six slice orientations chosen are displayed in **Figure 5.7-A**. Results show non-significant changes in CBFlux calculated in gray matter along different orientations, indicating isotropic cortical microvasculature. In the region containing the vessel, a significant increase in CBFlux (+136 %,  $p < 0.05$ ) is highlighted for three orientations around 90°. Angiography confirms the orientation of the large vessel (in green in **Figure 5.7-B**), orthogonal to the sagittal plane when it passes through the VOI. The changes in blood flux measured near a large vessel correlate well with the orientation of the vessel observed with MRA. However, it should be noted that the experiments described in this section are performed by rotating the labeling plane around

the same axis (see **Figure 5.6-A**). Therefore the CBFlux component along this particular axis is not probed, but kept constant in all the FENSI measurements.

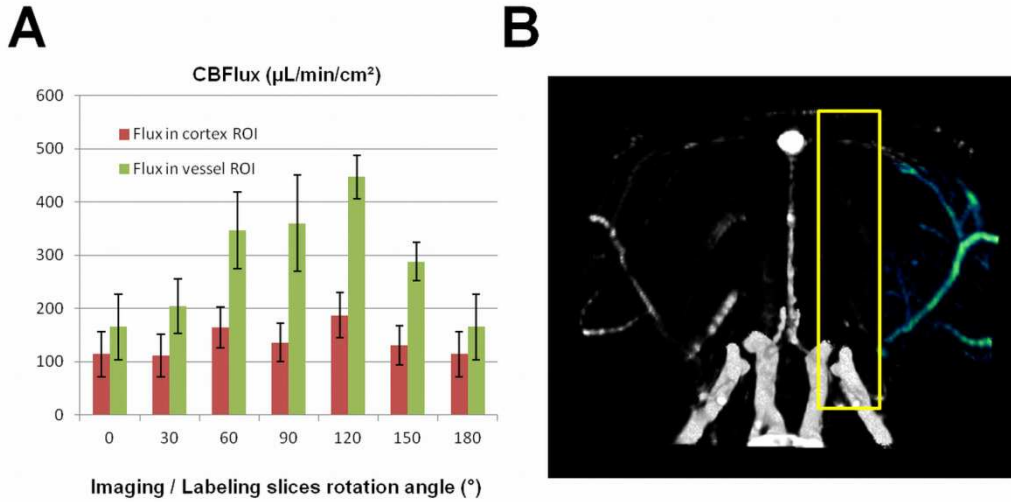


**Figure 5.7 Impact of slice orientation on CBFlux calculated in the cortex and near a large artery.** **A.** Mean blood flux values in regions containing cortex (red) / large vessel (green). **B.** MR Angiography results on the same rat (maximum intensity projection). The increase in flux observed in the sagittal orientation (coronal= $0^\circ$ , sagittal = $90^\circ$ ) is in agreement with the orientation of the blood vessel (in green) crossing the VOI (yellow box).

#### *Non-directionality of microvascular blood flux*

The previous preliminary results confirm that the FENSI method is sensitive to the directionality of blood flow. In order to probe the directionality of flux at capillary level, several CBFlux measurements are performed in different structures in four rats, such as cortical gray matter, cerebellar gray matter, striatum and corpus callosum. Based on the angiograms, the VOIs contaminated by arteries are excluded from the FENSI dataset. The calculated CBFlux is not found significantly different for any particular direction in the remaining structures.

This suggests that cerebral blood flux can be considered isotropic at capillary level. Its value is however different in different microstructures, and can reflect changes of the local cerebral blood volume, tissue permeability or blood velocity. Variations of these different parameters can be used to detect

alterations of the microvascular network in the presence of cerebrovascular diseases and other brain pathologies.

In addition, CBFlux measurements can in principle be correlated to the CBF estimates performed with conventional perfusion MRI techniques, such as ASL or DSC. In isotropic media, CBFlux and CBF both reflect local perfusion, and do not depend on the tracer path. Only the high sensitivity of ASL to blood transit times can however induce substantial differences when comparing CBF to CBFlux.

### *Feasibility of a flux tensor*

In order to assess more precisely the orientation of flow, one could consider probing CBFlux in a specific set of directions, similarly to tractography using Diffusion Tensor Imaging (DTI). Depending on the finesse and precision wanted on the fiber orientation, DTI protocols include between 6 and 200 acquisitions with different gradients inputs, each of them probing molecular diffusion in a particular direction. Combined with an EPI read-out, 6 to 200 scans are required per slice.

Similarly, we can assume that we want to probe CBFlux directionality using FENSI in a single slice. The position of the labeling plane will depend on the position of each particular voxel. Considering that a choice of 6 directions is sufficient to probe the orientation of flow in a given voxel and that the tSNR is high enough to detect significant changes from a single control-tag signal intensity subtraction,  $2 \times 32 \times 32 \times 6 = 12288$  acquisitions are needed to establish a single two dimensional ( $32 \times 32$ ) directionally-dependent flux map, making the technique - in its current implementation - in practice unsuitable for *in vivo* experiments. One needs to think of a better strategy than the voxel by voxel FENSI imaging suggested here in order to probe microvascular flow directionality.

### *Potential applications*

Our preliminary measurements indicate that CBFlux at capillary level can be considered isotropic and does not require a multi-directional approach. Considering higher blood flows, the structures that possess a well-defined orientation are likely to be relatively large blood vessels, whose orientation can be determined easily without the use of the “fancy” FENSI technique. The utility of targeting the orientation of microstructures using FENSI lies in-

between. Further studies should be performed to investigate the case of early formation of small blood vessels usually associated with tumor growth.

Due to time considerations, we suggest that the use of the FENSI method to probe the directionality of microvascular flow must be exclusively kept to detect very local changes of CBFlux. The use of ASL techniques incorporating flow-encoding gradients modules seems more suited than FENSI to map the directionality of the local brain perfusion. Perfusion Tensor Imaging (PTI) was recently achieved in the human brain and leg based on a VS-ASL technique (193). FENSI can however be used as a complement to ASL as it provides different information. FENSI and ASL techniques are indeed only sensitive to the blood outflow and inflow, respectively. These two components can substantially differ in the studies of brain tumors, and/or in case of BBB disruption.





## **VI. Gains, pitfalls, perspectives and applications**

**W**e discuss here the specific strengths and weaknesses of FENSI compared to conventional perfusion MRI. Our objective is to assess when CBFlux should or should not be quantified instead of CBF. The perks of performing FENSI at UHF are detailed. Based on the specificities of flow enhanced MRI, we propose a specific range of research fields and pathologies that can considerably gain from the use of FENSI.

In a first section we remind the alert reader that FENSI can provide compared to DSC-MRI a completely non-invasive and quantitative measure of brain metabolism. Compared to ASL, CBFlux quantification at capillary level does not suffer from elevated transit times and does not require the precise localization of a feeding artery.

It can however be inconvenient to use FENSI in some situations. The sequence is indeed dedicated to single slice imaging by design. Long saturation durations constrain the minimal temporal resolution achievable, preventing as a result the characterization of fast CBFlux changes in fMRI. In addition the FENSI tSNR does not meet our initial expectations. All of these features make of FENSI a poor choice to perform a quick characterization of brain vasculature with good coverage.

The performances of FENSI are investigated at UHF. The arterial blood longitudinal relaxation time and tSNR are evaluated at 17.2 T. Moreover, the effects of susceptibility artefacts and off-resonance effects, which increase with the magnetic field, on CBFlux quantification are discussed.

We suggest that FENSI can be used in specific situations where the other perfusion MRI techniques cannot accurately quantify CBF, such as muscular diseases and cerebrovascular disorders with collateral flow. Its comparison with BOLD fMRI and DWI is also of major importance to study the neurovascular coupling and IVIM model, respectively.

## **VI.1 The perks of using FENSI**

In this section are detailed the advantages of the FENSI technique compared to conventional perfusion MRI, represented by ASL and DSC-MRI.

### *FENSI versus DSC-MRI: non-invasiveness*

DSC-MRI methods are often considered minimally-invasive as they require the put of a catheter in the patient's arm (or the rodent's tail). The real danger comes however from the injection of the exogenous contrast agent. Gadolinium is indeed toxic under its ionic form and must be embedded into chelates to allow its safe use in hospitals. Causing no harm for most people, some patients can develop allergies and/or violently react to the gadolinium-based compounds.

Nephrogenic systemic fibrosis is for instance a progressive disease affecting patients suffering from renal insufficiency exposed to gadolinium based contrast agents (37). Symptoms vary from mild to fatal and include swelling and tightening of the skin and extremities. For individuals presenting a risk due to renal dysfunction, contrast agent injection is not recommended, or at extremely low dosage and cannot be repeated.

On the other hand, the FENSI technique (along with ASL) uses flowing blood as an endogenous contrast agent, guaranteeing the safety of the patient during the whole acquisition time and the absence of complications due to the MRI procedure. As in ASL (194), future studies should extensively investigate the potential of FENSI to detect or characterize cerebrovascular diseases such as stroke in patients with contraindications to gadolinium.

### *FENSI versus DSC-MRI: absolute quantification*

"Absolute" quantification of CBF with DSC-MRI suffers from several pitfalls. These are detailed in the first chapter and are briefly reminded here. First, CBF, MTT and CBV estimations are based on the tracer kinetics model (33-34). This model is only valid in case of an intact BBB, negligible bolus dispersion and delay, and negligible effect of the Gadolinium chelates on CBV,  $T_{1b}$  or CBF.

Second, knowledge on the AIF is required to derive true quantitative CBV, MTT and CBF parametric maps and conventional DSC-MRI protocols really estimate relative estimates of these different parameters. A rough

estimation of the AIF can be performed using MRI but is subject to flow turbulence, partial volume effects, delay and dispersion due to the distance between the artery and ROI (40-41). Absolute and reliable quantification of CBF is hardly achievable using DSC-MRI.

FENSI and ASL techniques benefit from the use of an endogenous tracer to fulfill the assumptions of the tracer kinetics model on CBV, CBF and  $T_{1b}$  by measuring a steady-state delivery/circulation of blood through the vascular network without injection. The FENSI technique does not require any external information on the AIF to quantify flux as blood is labeled at capillary level and provides a true quantitative marker of the brain metabolism through CBFlux.

### *On ASL & FENSI*

It has been shown here that FENSI and ASL techniques share several advantages compared to DSC-MRI. Both methods are however different in substance. The major distinction between FENSI and ASL is the position of the tagging plane. Whereas the blood magnetization inside a major blood vessel is inverted with PASL, CASL and PCASL; FENSI saturates locally the blood inside the microvasculature within a slice of interest.

### *FENSI versus ASL: slow flows and transit time effects*

One of the first implications is the increased sensitivity of FENSI to slow flows. ASL techniques are limited by transit times due to the tracer path from the label to the imaging slice. It is possible to investigate micro-perfusion and transit time dependence using ASL at different time-points. These techniques (time-encoded CASL, Hadamard-ASL) are discussed in chapter 5 and are in practice time-consuming. Another solution is to use VS-ASL that can encode flux regardless of its position, but remains in its current implementation dedicated to arterial blood flow characterization, rather than micro-perfusion. One will also mention FAIR-ASL that can, especially under its single-slice implementation, estimate the precise blood in-flow following a non-selective inversion slab (49).

By labeling blood inside the imaging plane, FENSI can provide highly localized flux information on microstructures presenting odd delivery pathways. This can be of prime interest when studying arteriovenous malformation, chaotic and tortuous microvascular structures during tumor growth, or collateral flow during acute or chronic stroke. FENSI provides

through localized tagging an insight into microvasculature. This is only accessible with ASL at the cost of extended transit times leading to major imprecision on CBF quantification.

### *FENSI & ASL: arbitrary tagging*

The position of the ASL label has to be oriented orthogonal to one or several major artery. The position of the tag in the FENSI technique is independent of the position of major vessels and depends on the particular ROI where microvasculature must be characterized. In practice, the tag position is limited by the extent of the imaging slab that is positioned around it which has to remain far from major susceptibility artefacts sources. FENSI can be used to characterize vasculature far from large blood vessels. Typically, ASL techniques cannot access muscular micro-perfusion due to poor labeling efficiency. Future studies should inquire on the reliability, reproducibility and accuracy of non-cerebral blood flux measurements with FENSI.

### *Conclusion*

Compared to DSC-MRI and ASL, the FENSI method is better suited to characterize vasculature when:

- patients have a contraindication for gadolinium based contrast agents
- absolute blood flux quantification is required
- vasculature must be assessed very locally or at capillary level
- measuring slow flows
- expecting elevated transit times
- arteries cannot be found or tagged efficiently with ASL.

## **VI.2 The FENSI technique: pitfalls and limitations**

However tempting to perform, the FENSI technique does not always meet the clinician's expectations. We present here the major drawbacks of the sequence, along with different leads to help resolve these problems.

### *Single Slice Imaging*

The FENSI technique is limited by design to single-slice imaging since its first implementation, making the method very inefficient compared to multi-slice DSC-MRI, ASL flow imaging techniques (86,195) or the recent development and clinical implementation of the whole-brain 3D-GRASE ASL technique (56,65,196) that combines a GE and SE acquisition.

During this PhD we have hoped to come out with a brilliant idea to overcome this problem, without success. We suggest here that the interested reader willing to orient his research towards multi-slice microvasculature characterization uses modified FENSI schemes.

An interesting alternative to FENSI called “pseudo-continuous Transfer Insensitive Labeling Technique” (pTILT) (197) has for instance been implemented on a clinical scanner. This method uses a preparation module similar to that of qFENSI (with balanced MT effects between control and tag) but acquires the MR signal sequentially in slices positioned only on one side of the tag. pTILT is a compromise between ASL and FENSI. As in ASL, it uses the blood in-flow to characterize perfusion inside different slices of interest. The directionality of flow is lost. As in FENSI, the position of the label is flexible and can be made very close to one or several of these slices in order to access micro-perfusion. FENSI can even be considered a particular case of pTILT, where the label is located between two consecutive imaging slices on which the MR signal is averaged.

### *Temporal resolution*

Large saturation durations are needed with FENSI in order to accumulate saturated spins (flowing with small blood velocities) into the imaging slice. In addition, two consecutive acquisitions (control/tag) are needed to quantify microvasculature.

Finally, one often chooses to interleave control and tag acquisitions to prevent a possible contamination of the flux-weighted by artefacts or changes in the static tissue  $T_2$  contrast. As a result, the TR is constrained by the  $T_1$  relaxation of the tag to prevent contamination of the control image by the previous tag.

All of these effects constrain the minimum TR of the sequence. This suggests that FENSI is not well suited to detect fast CBFlux changes, as seen in chapter 4. Because FENSI provides an absolute measure of CBFlux, the sequence represents however an excellent choice when performing

longitudinal characterizations of the brain microvasculature, as illustrated in chapter 3.

### *Contamination by macrovasculature*

The Flow Enhanced Signal Intensity method had been implemented to characterize blood flux at microvascular level. Provided the appropriate imaging parameters, our simulations show that the FENSI sequence is capable of detecting slow outflows on the order of 1 – 2 mm/s, matching the blood velocity at the capillary level. To accurately assess microvasculature, it is necessary to characterize the potential contamination of the FENSI flux-weighted image by arterial and/or venous blood in the macrovascular network.

In order to investigate the contamination of the FENSI data by large arteries and veins, we perform a blood flux measurement at ultra high field (17.2 T) under two different anesthetics: isoflurane and medetomidine (**Figure 6.1**). The anesthesia protocol is described in Chapter 4. Aside from CBFlux measurements,  $T_2^*$ -weighted images are acquired under both anesthetic states (**Figure 6.1-A**).

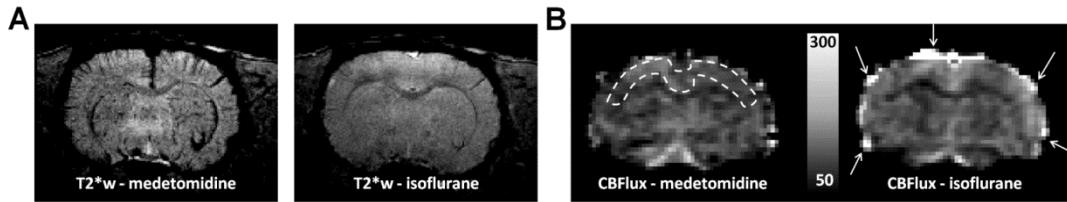


**Figure 6.1 A.  $T_2^*$ -weighted images of the rat brain (arbitrary units, axial view, spatial resolution 125 x 125 x 400  $\mu\text{m}$ ) and B. CBFlux maps ( $\mu\text{L}/\text{min}/\text{cm}^2$ , axial view, 300 x 300 x 2000  $\mu\text{m}$ ) acquired under medetomidine and isoflurane.** The white arrows indicate regions of hyper-perfusion due to contamination of the flux-weighted image by intravascular signal (CBFlux > 400  $\mu\text{L}/\text{min}/\text{cm}^2$ ) and/or susceptibility artefacts. The region of cortical gray matter used for flux calculation is delineated by the dashed ROI.

The  $T_2^*$ -weighted images acquired under medetomidine reflect the venous vascular network. Compared to isoflurane, the potential contribution of macrovasculature to the MR signal decreases dramatically under medetomidine, due to a decrease of the relaxation times  $T_2$  and  $T_2^*$  (**Figure 6.1-A**). During isoflurane anesthesia, the CBFlux map highlights several areas of hyper-perfusion (+100 % CBFlux compared to normal cortex) in the periphery of the cortex and near the sagittal sinus (**Figure 6.1-B**, white

arrows). This phenomenon remains however localized in the vicinity of large vessels (group 5; important cortical depth, vessel diameter 80 to 125  $\mu\text{m}$ ) as defined by the classification of Duvernoy et al.(149).

In the cortex (**Figure 6.1-B**, dashed ROI) and in the presence of moderately large vessels (**Figure 6.1-A**), the choice of anesthetic agent has little influence on the calculated CBFlux, despite a decrease of the macrovascular network contribution due to increase of susceptibility. The 15 % CBFlux decrease under medetomidine is expected as medetomidine/isoflurane anesthetics are known to induce a decrease/increase of the local perfusion, respectively.

These results suggest that the FENSI cerebral blood flux maps can be contaminated by intravascular signal, at the proximity of large vessels. The introduction of saturation pulses in the control image might not be sufficient to remove the intravascular flux component as spins can flow through the macrovasculature in a wide range of velocities (5-30 mm/s). In addition, the FENSI sensitivity range is based on blood velocity weighted by the flowing spins fraction. It is likely that the high concentration of flowing spins per voxel will be detected in the FENSI flux-weighted image.

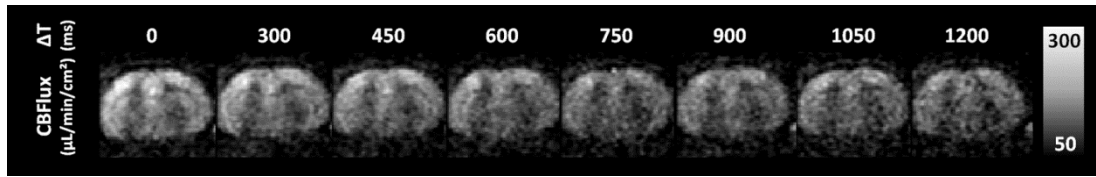


**Figure 6.2 Influence of the labeling - acquisition delay  $\Delta T$  (ms) on the CBFlux contamination by intravascular signals.** *Intravascular signals can be observed for small delays ( $\Delta T < 600$  ms) near the sagittal sinus. The macrovascular component of flux vanishes for post labeling delays larger than 600 ms. The SNR decreases as  $\Delta T$  increases. In order to calculate CBFlux, an additional correction that compensates for  $T_1$  relaxation effects during  $\Delta T$  is performed.*

At UHF, the use of an appropriate anesthetic agent can help compensate for such effects. As in ASL, the introduction of a transit time between the labeling and the MR signal acquisition might also help remove the vascular component of CBFlux, but can impact the SNR and the minimum velocities  $v_{\text{MIN}}$  that FENSI can detect. Our measurements at 17.2 T (**Figure 6.2**) show that a delay of 600 ms between labeling and acquisition is sufficient to remove completely the intravascular component of CBFlux, in association with  $N = 6$  control tags that strongly decrease the sensitivity of FENSI to the spins flowing above the velocity cut-off  $v_c = 10$  mm/s.



### *Temporal Signal-to-Noise Ratio*

The tSNR obtained with FENSI is compared, after optimization of the sequence, to that of qFENSI and conventional ASL techniques. As discussed in chapter 4, the traditional method to evaluate the mean temporal SNR in ASL consists in dividing the calculated CBF by the temporal standard deviation voxel-by-voxel and average the result in a ROI containing gray matter (59).

We derive with our current FENSI implementation mean tSNR values of  $0.4 \pm 0.2$  at 7 T and  $1.1 \pm 0.2$  at 17.2 T. These results are in good agreement with the SNR values ( $0.8 \pm 0.2$ ) reported by Ouyang et al. (85) on a 3 T clinical MRI scanner. The mean tSNR obtained at 17.2 T is not higher than that of ASL (tSNR of QUIPSS II / VS-ASL = 2.1 / 1.1) calculated at 3 T (59). Based on a SNR criterion, the implementation of the FENSI technique does not enhance the scanner performances compared to conventional ASL techniques.

Different factors impact the SNR. FENSI is only sensitive to the blood flow component orthogonal to the labeling plane, whereas ASL acquires within a single voxel signal from the spins flowing in all the directions. In addition, the labeling efficiency of ASL sequences is increased compared to FENSI by the use of inversion pulses ( $180^\circ$  FA radio-frequency pulses). One should also consider the nature of the tracer. ASL techniques label an entire feeding artery when FENSI targets microvascular flow at capillary level.

Future developments should investigate the potential increase of SNR when performing FENSI. We present here several suggestions to improve the efficiency of the FENSI technique.

As in ASL, FENSI flux-weighted images are generated by subtracting control and tag images. Both these images contain static tissue and can be affected by physiological noise or motion which can dominate the small fluctuations of signal caused by the labeled flowing blood. Different ASL groups have recently studied the use of background suppression (BGS) pulses to minimize the noise associated with static tissue (59,61,64). Reports indicate a significant SNR increase (+100-160 %) when using BGS-ASL or BGS-VS-ASL instead of regular ASL and VS-ASL sequences (59).

In practice, the implementation of BGS pulses is difficult with FENSI because of the position of the tagging and imaging slices that overlap. Well-defined pulse profiles should be used to invert the magnetization of the static spins from the imaging slab without affecting the flowing spins from the tag.

Assuming that physiological noise and motion have very little influence on control and tag image intensities, most of the information about microvasculature is contained in the tag image. The BGS-FENSI technique can also benefit from the use of asymmetric control and tag encoding. Acquiring

several tags for a single control can substantially increase the temporal resolution / SNR of flow labeling techniques, without impacting quantification when used in association with BGS pulses (198).

### *Conclusion*

Despite major improvements, the use of the technique FENSI remains limited compared to ASL. Suffering from a poor coverage and tSNR compared to ASL techniques, we suggest that FENSI is used as a complement of ASL to investigate locally microvascular networks, far from macrovasculature. Future methodological developments around FENSI should inquire about the potential increase of sensitivity to compete with ASL techniques.

## **VI.3 The FENSI technique at UHF: gains and roses**

New perspectives were offered to the FENSI sequence with the arrival of the 17.2 T Bruker MRI scanner dedicated to rodents at Neurospin in the fall 2010. After optimization of the technique at 17.2 T, the advantages and drawbacks of UHF are investigated. We highlight several key-points to keep in mind when implementing the FENSI method at high field.

### *Increase of the blood longitudinal relaxation time at high field*

For a given tissue, substance or structure,  $T_1$  increases with the magnetic field. The longitudinal relaxation time of blood  $T_{1b}$  is of particular importance for ASL sequences and FENSI as it characterizes the temporal evolution of the tag.

$T_{1b}$  has been experimentally measured at various magnetic fields between 1.5 and 11.7 T. **Table 11** illustrates the experimental results obtained from literature (199-204). Based on these results, Dobre et al. (203) proposed a linear model for the change in longitudinal relaxation with static magnetic field  $B_0$ :  $T_{1b \text{ linear}} = 1167 \text{ ms} + B_0(T) * 129 \text{ ms/T}$ , valid between 1.5 and 9.4 T. It is worth noting that  $T_{1b}$  also depend on the particular hematocrit and oxygenation level in the blood (204). The values reported in **Table 11** correspond to arterial blood hematocrit (Hct = 0.4) and oxygenation (>75%) levels. In veins,  $T_{1b}$  slightly changes due to lower oxygenation (199-201).

An accurate *in vivo* measurement of the arterial  $T_{1b}$  is difficult to implement in practice as arterial blood is highly pulsatile and in-flow effects affect  $T_1$  calculation. In literature,  $T_{1b}$  measurements protocols are often performed *in vitro* and involve: blood sampling on different animals (bovine, rabbit), mixing of the samples with a solution of heparin in order to prevent blood coagulation, and storage between the sampling and MR acquisition. During the MRI session, the blood is circulated inside the magnet through a gas exchange system. Oxygenation and temperature are carefully monitored. Hematocrit rates, blood gases and pH are measured prior and post MR acquisition to ensure normal physiological conditions. The blood circulation is only stopped between radio-frequency deposition and FID acquisition.

**Table 11  $T_{1b}$  of arterial blood measured at various field strengths**

Magnetic field $B_0$ (T)	Experimental $T_{1b}$ (ms)	Reference
<b>1.5</b>	1355	Lu et al. (199)
	1435	Barth and Moser (200)
<b>3</b>	1664	Lu et al. (201)
<b>4.7</b>	1700	Silvennoinen et al. (202)
	1833	Dobre et al. (203)
<b>7</b>	2212	Dobre et al. (203)
<b>9.4</b>	2429	Dobre et al. (203)
<b>11.7</b>	2813	Lin et al. (204)
<b>17.2</b>	3192	-

*Our experimental measurement of  $T_{1b}$  at 17.2 T (3192 ms) is in good agreement with the linear model (203) established between 1.5 T and 9.4 T, and extrapolated at 17.2 T ( $T_{1b \text{ linear}} = 3385 \text{ ms}$ ).*

Recently, Lin et al. (204) proposed a simpler protocol to measure  $T_{1b}$  at 11.7 T. The blood sample is taken from the femoral artery of an anesthetized rat. The blood gases are analyzed and the hematocrit concentration determined by a high speed industrial micro-hematocrit centrifuge. The sample is quickly placed in the magnet where its temperature is adjusted to 37°C in contact with a circulating water bed.  $T_{1b}$  is determined based on a multiple-TR sequence. The total preparation and scanning time does not exceed 30 min. The blood gases are again analyzed after the MRI session. The experimental  $T_{1b}$  measured at 11.7 T with this method (2813 ms) fits the linear model ( $T_{1b \text{ linear}} = 2676 \text{ ms}$ ).

The same protocol is used to measure the  $T_1$  of arterial blood at 17.2 T. For MR acquisition, we use a Fast Spin-Echo sequence (FOV 1 x 1 x 4 mm<sup>2</sup>, matrix size 32 x 32, TE = 40 ms, RARE factor = 4) and 12 TRs between 500 and 25000 ms (TA = 6 min 40 s). The hematocrit rate Hct could not be monitored but literature indicates that Hct has in normal conditions only little

influence ( $< 15\%$ ) on  $T_{1b}$  at 11.7 T (204). The data is fitted based on a saturation recovery model:  $S(TR) = A \cdot (1 - \exp(-TR/T_{1b}))$ . In those conditions and at 37°C, we find an experimental  $T_{1b}$  of  $3192 \pm 140$  ms. This is to our knowledge the first determination of the longitudinal relaxation time of arterial blood at such a high magnetic field. Our measurements corroborate the linear model proposed by Dobre et al. (203) and validate the linear variation of  $T_{1b}$  with  $B_0$ .

### *SNR increase at high field*

The increase of signal with field  $B_0$  strength is well-documented in literature and lies in the solution of Maxwell's equations. At equilibrium, the NMR signal is proportional to the square of  $B_0$ . The background noise also increases with the magnetic field and its variance is proportional to the square of  $B_0$ . Therefore the SNR, defined as the ratio of the average signal by the standard deviation of the noise, increases linearly with  $B_0$ . This is a strong source of motivation in research for developing higher magnetic fields NMR and MRI systems. The objective is here to minimize scan times in the clinic and/or increase the spatial or temporal resolution.

The recent developments of non-invasive perfusion MRI techniques directly depend on this quest for higher fields. By labeling a small fraction of the total population of spins, ASL and FENSI methods are limited by the SNR. Several repetitions of control and tag images are required to generate a single CBF or CBFlux map, explaining why DSC-MRI is still at the moment considered as the gold standard in clinical perfusion MRI. The current installation in many hospitals of high field clinical MRI scanners will help ASL techniques catch up with DSC-MRI in this domain.

Regarding FENSI, the technique is implemented at 7 and 17.2 T. One expects a +145 % SNR/tSNR increase of MR signal based on field strength only. One must add to this effect the more efficient labeling of slow spins due to longer  $T_{1b}$ , as illustrated in the previous paragraph. Some imaging parameters are optimized at 17.2 T in order to prevent a decay of the MR signal due to a decrease of the transverse relaxation time  $T_2$  at high field. **Table 12** summarizes the list of FENSI parameters used for *in vivo* measurements after optimization of the sequence at 7 and 17.2 T. Experimentally the SNR of the flux-weighted image sensitized to the same blood velocities is increased by  $\sim 160\%$  at 17.2 T (same acquisition time) and encourages the use of FENSI at UHF.

**Table 12 Comparison of the FENSI parameters used to perform *in vivo* CBFlux measurements at 7 and 17.2 T**

$B_0$ (T)	7	17.2
TR/TE (ms)	6000/13	5000/20
Number of segments	4	1
In-plane resolution (mm)	0.25 x 0.25	0.25 x 0.25
Field of View (mm)	20 x 20	20 x 20
Slice thickness (mm)	6.5	8
Tag thickness (mm)	1	2
Number of control tags	3	3
Number of tags	150	67
$T_{SAT}$ (ms)	3000	1000
Total Acquisition Time	15min	
SNR	$3.8 \pm 1.1$	$10.0 \pm 1.3$

The second column presents the list of parameters used in the tumor study (chapter 3). We present the average SNR obtained in a ROI centered on cortical gray matter in the flux-weighted image ( $N = 10$  rats). At 17.2 T (third column), the SNR is significantly increased ( $p < 0.01$ ) after optimization of the FENSI parameters.

#### Susceptibility artefacts

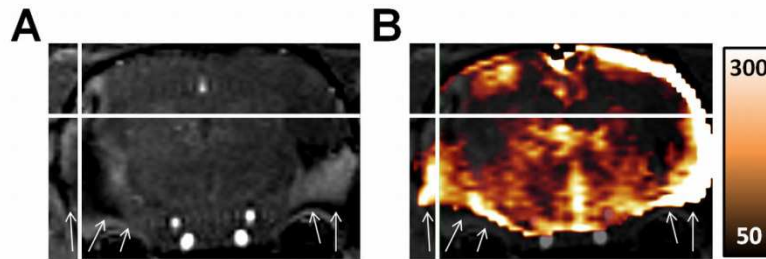


**Figure 6.3 Impact of susceptibility artefacts on CBFlux quantification. A.** At UHF, susceptibility artefacts are visible on  $T_2^*$ -weighted imaging (FLASH, TR/TE = 15/2 ms, spatial resolution 120 x 120 x 400  $\mu\text{m}$ ), near the ears (white arrows) and in the cortical left hemisphere (white cross). **B.** Overlay of the CBFlux map ( $\mu\text{L}/\text{min}/\text{cm}^2$ ) on the  $T_2^*$ -weighted image. Abnormal increase and decrease of the normal brain CBFlux can be observed in the regions indicated by the white arrows and cross, respectively. The CBF increase observed in the upper-right cortical region is due to motion of the subject during acquisition.

$T_2$  and  $T_2^*$  transverse relaxation times decrease when the magnetic field increases. The study on the effect on various anesthetics on the BOLD contrast at 17.2 T (chapter 4) illustrate that the MR signal at UHF is very sensitive to the local perturbations of the magnetic field. The flux-weighted

information represents only a fraction of the image acquired in control or tag mode with FENSI, but the SNR of the flux-weighted image depends on the quality of the entire imaging slice.

These effects are particularly visible in the rat brain near the ears due to major  $B_0$  field inhomogeneities caused by magnetic susceptibility differences. Throughout this manuscript, a single loop coil positioned over the rat brain is used as transceiver. This choice was initially motivated by an increased sensitivity near the coil in the rat cortex and striatum when performing FENSI at 7 T. In addition it allows for reduced FOV without the need for additional saturation bands.

Due to the large imaging slice thickness (6.5 – 10 mm) required to accumulate labeled spins, artefacts are likely to appear on the edges of the brain and around the ears at UHF (**Figure 6.3-A**). Their contribution to the flux-weighted image remains small, as they theoretically contribute to both control and tag images. However, the MR signal can be highly distorted and cause dark spots on the CBFlux map (**Figure 6.3-B**). Based on our experience at 17.2 T we recommend that the shimming must be properly performed prior to the FENSI acquisitions to minimize susceptibility artefacts, as they can be misleading when interpreting CBFlux data. On Bruker systems, automatic iterative shim protocols, such as Fastmap or Mapshim can help homogenize the field around the slice of interest.

#### *Efficiency of the labeling and refocusing of the spins*

Susceptibility effects are not the only pitfalls of the use of FENSI and ASL perfusion sequences at UHF. The labeling efficiency ( $\alpha$ ) relies on the pulse shape and power used for spin inversion and directly impacts flux calculation with ASL and FENSI techniques. It is defined for FENSI by the missing magnetization (between control and tag) of the label taken immediately after saturation divided by the magnetization of the labeling slab taken at equilibrium. Typical ASL techniques use pulses with labeling efficiencies comprised between 0.75 and 1 (perfect saturation/inversion). For FENSI, the saturation is often assumed ideal for CBFlux calculation based on equation [1.7].

Regarding the FENSI technique implemented *in vivo* in this manuscript, 45° - 45° FA pulses are introduced within the control preparation module to balance MT effects between control and tag. The magnetization of the control image can be decreased if the refocusing of the spins by the second pulse is not perfect or affects a different population of spins. To counter this last effect, the delay between the 45 and -45° pulses is minimized.

In addition, the application of a slice-selective gradient (with frequency offset  $\Delta f$ ) during the first  $45^\circ$  FA pulse introduces an additional dephasing of the semi-saturated spins (proportional to  $\Delta f$ ) which can affect the tag profile (**Figure 6.4-B**). In order to compensate for that effect, the phase of the two  $\pm 45^\circ$  radio-frequency pulses must be carefully adjusted, depending on the position of the labeling slab with respect to the center of the magnet.

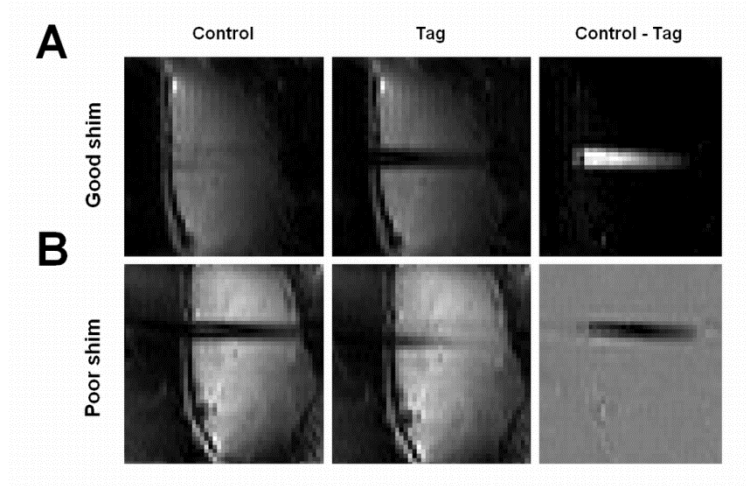


**Figure 6.4 Control and Tag profiles acquired orthogonally to the labeling slice** (sagittal view). **A.** Provided a good shim and adjustment of the phase of the  $45^\circ$  pulses, spins are fully refocused or saturated on the Control and Tag intensity profiles, respectively. The tag profile is obtained by subtraction of the control and tag intensity. **B.** The labeling and refocusing efficiency is impacted by the off-resonance effects and the dephasing of the spins subject to the first  $45^\circ$  pulse. This can result in an inversion of the control and tag profiles, leading to negative CBF<sub>flux</sub> values.

To visualize the quality of the tag (**Figure 6.4-A**) imaging is performed orthogonal to the labeling plane, and subtracting the MR signal acquired after having saturated or refocused the spins with a single pair of the same  $45 \pm 45^\circ$  FA pulses used for CBF<sub>flux</sub> quantification.  $\alpha$  is measured on the tag profile, and varies in practice between 0.85 and 0.97 when the system is properly shimmed. Failure to obtain a decent control or tag profile is illustrated in **Figure 6.4-B**. Off-resonance effects decrease the labeling and refocusing efficiency and can result in an inversion of the control and tag signals.

#### *On the use of UHF*

The FENSI technique was successfully implemented at 7 and 17.2 T, and CBF<sub>flux</sub> measurements between HF and UHF compared. The use of UHF

allows for significantly higher SNR/tSNR in the FENSI control, tag, and flux-weighted images, reducing the acquisition time necessary to quantify CBFlux *in vivo*. In addition, the longitudinal relaxation time of blood is doubled at 17.2 T compared to clinical fields of 1.5 to 3 T. The labeling efficiency is increased, which is of particular importance in FENSI to measure slow flows and in multi-slices ASL schemes where the gaps between the labeling and the imaging locations can be substantially large.

Although the FENSI method benefits from the use of high magnetic fields, flux-weighted images acquired at UHF can suffer from artefacts due to magnetic field inhomogeneities. In the most severe cases, control and tag images can fail to efficiently refocus and label spins, respectively. The labeling efficiency must be carefully assessed before any FENSI experiment to prevent a possible underestimation of CBFlux.

## **VI.4 Perspectives and applications**

In this section we suggest different ways of using the FENSI technique, in need of being investigated. Some can be applied in the very near future. The other ones might require further technical and methodological developments.

### *FENSI and Intra Voxel Incoherent Motion*

The interactions between perfusion MRI and DWI can be studied at high field using Intra Voxel Incoherent Motion (IVIM). By considering the capillary bed as a random maze where blood flow constantly changes direction, the fraction of flowing spins can be estimated with the IVIM model using DWI at very low b-values. IVIM can in principle be used to characterize the apparent diffusion coefficient and the spin fraction related to perfusion (7-8).

The relationship between IVIM and perfusion remains however controversial (9). In addition, no study has ever investigated the spatial dependence of the IVIM parameters in patients suffering from cerebrovascular diseases, and compared the results with those obtained with perfusion MRI and immunohisto-chemistry.

We propose the implementation of a multi-modal preclinical imaging protocol to probe microvasculature. In this manuscript we show that tumor microvascular networks can be characterized at different developmental stages. The results obtained with FENSI correlate with immunohisto-chemistry and microvessel concentration. In addition, FENSI is capable of providing flowing spins fraction parametric maps when using long saturation



durations. This allows for a direct comparison of IVIM and FENSI-based vascular fractions ( $f_{\text{IVIM}}/f_{\text{FENSI}}$ ) in different brain locations, including the gliosarcoma periphery and core. Results can also be compared to contrast-enhanced MRI and immunohisto-chemistry to provide an accurate estimation of the microvessel concentration.

Preliminary results highlight the large spatial heterogeneity of  $f_{\text{FENSI}}$  and  $f_{\text{IVIM}}$  inside the tumor. Interestingly, both measures do not seem to correlate everywhere in the brain. Further studies will investigate the specificities of both techniques and compare  $f_{\text{FENSI}}$  and  $f_{\text{IVIM}}$  with the true microvessel concentration obtained with CD31 staining.

### *FENSI functional MRI*

Our efforts towards preclinical FENSI functional MRI are described in chapter 4. Despite the implementation of a robust fMRI protocol at 7 T, we could not detect any significant CBFlux change in the rat brain in response to a forepaw electrical stimulus. Failure to detect flux changes is likely due to poor SNR, as highlighted by the CBFlux calculation during the hypercapnia challenge performed at 7 T.

The SNR of the flux-weighted image is increased by the implementation of the FENSI technique at UHF. At 17.2 T, our calculations exhibit temporal SNR values ( $t\text{SNR}_{\text{FENSI}} = 1.1$ ) similar to that of qFENSI ( $t\text{SNR}_{\text{qFENSI}} = 0.8$ ) or VS-ASL ( $t\text{SNR}_{\text{VS-ASL}} = 1.1$ ). During stimulation, both qFENSI and VS-ASL methods were proven capable of quantifying blood flux and blood flow changes, respectively (59,85). Based on these results, we believe that the FENSI technique can be successfully applied to preclinical functional MRI.

Provided functional FENSI experiments can be performed on a large database, the comparison of the BOLD and CBFlux based activation maps can be of prime interest to characterize the tight relationships between neural activity, brain metabolism, cerebral blood flow and the hemodynamic response.

The spatial localization of brain activity is especially relevant, as the BOLD contrast mainly comes from susceptibility changes from the venous network whereas FENSI labels at microvascular level. FENSI has the potential to reveal the metabolic changes following stimulation at sub-millimeter level and investigate highly localized flux changes. However, the temporal resolution of FENSI (8-10 seconds / flux-weighted image) will not help resolve problems of causality or neural inference.

### *Pharmacological MRI / Treatment follow-up*

As opposed to BOLD, FENSI quantifies a true biological marker of the brain metabolism. This allows for repeated and/or longitudinal studies, and possible comparison of datasets between research centers. These characteristics make FENSI suitable for pharmacological MRI as well as diagnostic and treatment follow-up.

### *Cerebrovascular diseases, ischemia and collateral flow*

Most of ASL (with the possible exception of VS-ASL and FAIR) techniques cannot accurately quantify slow flows due to the elevated transit times between the labeling and imaging positions. The different ASL methods implemented in routine on clinical scanners have been adjusted to be sensitive to regular blood transit times. This can result in CBF quantification failure in patients suffering from AVM, arterial occlusion, ischemia or other cerebrovascular diseases.

On the other hand, the Flow Enhanced Signal Intensity technique is suited for microvascular flow characterization. By labeling spins at capillary level, the flux-weighted image can be sensitized to a wide range of velocities, ranging from 1 to 30 mm/s. These can reflect the blood flow inside the capillaries, arterioles, venules and small blood vessels in general.

By the means of extended saturation durations, spins flowing at reduced speed can accumulate into the imaging slice and generate flux contrast. Compared to conventional ASL, the FENSI technique is less sensitive to transit time variations. It is, along with VS-ASL or FAIR, better suited to characterize local micro-perfusion due to the labeling/imaging slice proximity.

Regarding ischemic patients, ASL is often used to localize the 'penumbra', defined as the hypo-perfused area surrounding the infarction that can recover when properly treated. Although the gold standard to characterize the penumbra is PET, MRI can be used to accurately localize this area. The diffusion/perfusion mismatch reveals for instance the area of low CBF (visible with ASL) that is not subject to cellular death (visible with DWI) and is therefore a good match for the penumbra.

Quantification of the penumbra volume is crucial as it correlates with neural recovery. Microvascular CBFlux quantification can inform further on the flow dynamics at capillary level. In addition, the FENSI technique could be used to investigate the collateral flow circulation (16), whose role is to feed the brain with blood through collateral vascular channels when the main arteries

are blocked. This secondary vascular network is characterized by extended blood transit times and has a major impact on recovery from cerebral ischemia (17-18).

### *Muscular diseases*

Last but not least, we recommend that the FENSI technique is tested in conditions that do not favor conventional ASL. In the absence of a well-defined and straight feeding artery, ASL methods suffer from poor SNR due to an inefficient labeling and reduced blood velocities. Theoretically, FENSI can provide an accurate measurement of the local blood flux in structures distal from the macrovasculature. It may for instance be suited to characterize non-invasively microvascular perturbations in muscles using MRI. There is at the moment no evidence of the functioning of the FENSI technique in tissues located outside the brain. This research area is soon to be investigated.

## General conclusion

The objective of this work was to investigate the development of a new non-invasive quantitative perfusion MRI sequence - the FENSI technique - and its potential application to the characterization of microvascular flow dynamics.

The stakes of perfusion MRI in neuroimaging are presented. The conventional methods - ASL, DSC-MRI - used to derive perfusion (in units of cerebral blood flow) are detailed and their advantages and drawbacks discussed. We introduce the FENSI technique, a recently developed MRI sequence that can characterize microvasculature (in units of cerebral blood flux) and is of potential interest compared to ASL methods. Different issues must however be addressed. The flux-weighted signal can be contaminated by MT effects that prevent the possible quantification of blood flux at capillary level. A post-processing correction method is proposed to compensate for MT effects. The first FENSI parametric flux maps are derived at 7 T. A second approach is considered where MT effects are fully balanced between the control and tag images, allowing for a truly non-invasive quantification of cerebral blood flux *in-vivo*.

We characterize cerebral microvasculature at different stages of the 9L gliosarcoma tumor growth using the MT-balanced FENSI technique. Our CBFlux results at early stage (tumor diameter < 3 mm) reflect major inter-individuals variations of the glioma global vasculature. Late stage gliomas (tumor diameter > 3 mm) exhibit significantly lower blood flux (-40 %), in good agreement with literature on 9L perfusion. In addition, different tumor compartments can be visualized on the flux parametric maps. The comparison with immunohisto-chemistry suggests that CBFlux correlates with the local microvessel concentration.

Many efforts have been made during this thesis to investigate the temporal dynamics of microvascular flow and the potential of FENSI when applied to functional MRI. A fMRI protocol is implemented at 7 T, and the hemodynamic response to a forepaw electrical stimulus characterized based on BOLD contrast. Regarding dynamic acquisitions, the FENSI technique does not meet our expectations at 7 T due to low temporal SNR and seems better suited to characterize longitudinal CBFlux changes. As opposed to BOLD, it does not suffer from large scales signal fluctuations and provides a truly quantitative measurement of the brain metabolism. The implementation of the sequence at UHF gives rise to serious hopes regarding the use of FENSI in fMRI. We highlight at 17.2 T specific contrasts due to the use of various anesthetics commonly used in the clinic.

The adjustment of different imaging parameters sensitizes the FENSI technique to various velocities and increases the number of potential applications. After exploring the influence of the experiment's geometry on the flux-weighted contrast, we highlight in this manuscript a different use for FENSI that can reveal the vascular spin fraction. The method remains however sensitive to flow directionality. Its strengths and weaknesses compared to conventional perfusion MRI are discussed. Sadly, using FENSI does not increase the SNR compared to optimized ASL strategies. The method will however benefit from the actual trend towards higher magnetic field MRI scanners. Potential applications range from fMRI and DWI characterization to pharmacological MRI and stroke treatment. The large majority of cerebrovascular disorders affect the blood transit times. FENSI can be used as a complement of ASL to help resolve the apparent hypo-perfused areas highlighted by CBF mapping.

Different tools and techniques were developed during this PhD. For the first time, a completely non-invasive quantification technique was implemented on two preclinical high field MR scanners at 7 and 17.2 T. A robust and reproducible rat functional MRI protocol - now up and running - was designed and optimized at different field strengths, including meticulous animal preparation. Methodological developments included the programming and implementation of perfusion MRI and triggered fMRI acquisitions. Image processing was performed using custom-written software to automate calculations. The 9L gliosarcoma model characterized in this manuscript is now commonly used to study cerebrovascular perturbations associated with tumor growth in the rodent brain.

Beyond methodological and experimental developments, we begin to understand the underlying mechanisms of Flow Enhanced MRI and non-invasive microvascular contrast. The possible characterization of ischemic patients using the FENSI technique will be assessed in the following months. The performances of FENSI at UHF are promising and will be used to study the precise locations of neural activity beyond the venous contribution that is accessible with BOLD fMRI. Additional and extensive investigations on the 9L rat brain tumor model must validate the correlation of CBFlux with microvessel concentration. The future comparison of IVIM and FENSI based vascular fraction maps with immunohisto-chemistry is expected to clarify the true nature of Intra Voxel Incoherent Motion. In addition, the different experiments that we performed raise questions of potential interest in clinical practice. Can we monitor the effects of anesthetics on the central nervous system in real time using MRI?

## References

1. Sutton BP, Ouyang C, Ching B, Ciobanu L. Functional imaging with FENSI: Flow-ENhanced Signal Intensity. *Magnet Reson Med* 2007;58.
2. Bloch F, Hansen WW, Packard M. Nuclear Induction. *Phys Rev* 1946;69(3-4):127-127.
3. Purcell EM, Torrey HC, Pound RV. Resonance Absorption by Nuclear Magnetic Moments in a Solid. *Phys Rev* 1946;69(1-2):37-38.
4. Lauterbur PC. Image Formation by Induced Local Interactions - Examples Employing Nuclear Magnetic-Resonance. *Nature* 1973;242(5394):190-191.
5. Mansfield P. Proton Spin Imaging by Nuclear Magnetic-Resonance. *Contemp Phys* 1976;17(6):553-576.
6. Haacke EM. Magnetic resonance imaging : physical principles and sequence design. New York: Wiley; 1999. xxvii, 914 p. p.
7. Le Bihan D, Breton E, Lallemand D, Grenier P, Cabanis E, Laval-Jeantet M. MR imaging of intravoxel incoherent motions: application to diffusion and perfusion in neurologic disorders. *Radiology* 1986;161(2):401-407.
8. Le Bihan D. Intravoxel incoherent motion perfusion MR imaging: a wake-up call. *Radiology* 2008;249(3):748-752.
9. Koh DM, Collins DJ, Orton MR. Intravoxel incoherent motion in body diffusion-weighted MRI: reality and challenges. *AJR Am J Roentgenol* 2011;196(6):1351-1361.
10. Sigmund EE, Cho GY, Kim S, Finn M, Moccaldi M, Jensen JH, Sodickson DK, Goldberg JD, Formenti S, Moy L. Intravoxel incoherent motion imaging of tumor microenvironment in locally advanced breast cancer. *Magnet Reson Med* 2011;65(5):1437-1447.
11. Parkes LM, Rashid W, Chard DT, Tofts PS. Normal cerebral perfusion measurements using arterial spin labeling: reproducibility, stability, and age and gender effects. *Magnet Reson Med* 2004;51(4):736-743.
12. Wang Z, Fernandez-Seara M, Alsop DC, Liu WC, Flax JF, Benasich AA, Detre JA. Assessment of functional development in normal infant brain using arterial spin labeled perfusion MRI. *Neuroimage* 2008;39(3):973-978.
13. van Osch MJP, Teeuwisse WM, van Walderveen MAA, Hendrikse J, Kies DA, van Buchem MA. Can Arterial Spin Labeling Detect White Matter Perfusion Signal? *Magnet Reson Med* 2009;62(1):165-173.
14. Detre JA, Alsop DC, Vives LR, Maccotta L, Teener JW, Raps EC. Noninvasive MRI evaluation of cerebral blood flow in cerebrovascular disease. *Neurology* 1998;50(3):633-641.
15. Markus HS. Cerebral perfusion and stroke. *J Neurol Neurosurg Psychiatry* 2004;75(3):353-361.
16. Liebeskind DS. Collateral circulation. *Stroke* 2003;34(9):2279-2284.
17. Henderson RD, Eliasziw M, Fox AJ, Rothwell PM, Barnett HJ. Angiographically defined collateral circulation and risk of stroke in patients with severe carotid artery stenosis. *North American*

- Symptomatic Carotid Endarterectomy Trial (NASCET) Group. *Stroke* 2000;31(1):128-132.
18. Robertson RL, Burrows PE, Barnes PD, Robson CD, Poussaint TY, Scott RM. Angiographic changes after pial synangiosis in childhood moyamoya disease. *AJNR Am J Neuroradiol* 1997;18(5):837-845.
  19. Donahue KM, Krouwer HG, Rand SD, Pathak AP, Marszalkowski CS, Censky SC, Prost RW. Utility of simultaneously acquired gradient-echo and spin-echo cerebral blood volume and morphology maps in brain tumor patients. *Magnet Reson Med* 2000;43(6):845-853.
  20. Lemasson B, Valable S, Farion R, Krainik A, Remy C, Barbier EL. In vivo imaging of vessel diameter, size, and density: A comparative study between MRI and histology. *Magnet Reson Med* 2012.
  21. Wolf RL, Wang JJ, Wang SM, Melhem ER, O'Rourke DM, Judy KD, Detre JA. Grading of CNS neoplasms using continuous arterial spin labeled perfusion MR imaging at 3 tesla. *Journal of Magnetic Resonance Imaging* 2005;22(4):475-482.
  22. Warmuth C, Gunther M, Zimmer C. Quantification of blood flow in brain tumors: Comparison of arterial spin labeling and dynamic susceptibility-weighted contrast-enhanced MR imaging. *Radiology* 2003;228(2):523-532.
  23. Ozsunar Y, Mullins ME, Kwong K, Hochberg FH, Ament C, Schaefer PW, Gonzalez RG, Lev MH. Glioma Recurrence Versus Radiation Necrosis? A Pilot Comparison of Arterial Spin-Labeled, Dynamic Susceptibility Contrast Enhanced MRI, and FDG-PET Imaging. *Acad Radiol* 2010;17(3):282-290.
  24. Alsop DC, Detre JA, Grossman M. Assessment of cerebral blood flow in Alzheimer's disease by spin-labeled magnetic resonance imaging. *Ann Neurol* 2000;47(1):93-100.
  25. Johnson NA, Jahng GH, Weiner MW, Miller BL, Chui HC, Jagust WJ, Gorno-Tempini ML, Schuff N. Pattern of cerebral hypoperfusion in Alzheimer disease and mild cognitive impairment measured with arterial spin-labeling MR imaging: Initial experience. *Radiology* 2005;234(3):851-859.
  26. Chao LL, Buckley ST, Kornak J, Schuff N, Madison C, Yaffe K, Miller BL, Kramer JH, Weiner MW. ASL perfusion MRI predicts cognitive decline and conversion from MCI to dementia. *Alzheimer Dis Assoc Disord* 2010;24(1):19-27.
  27. Liu HL, Kochunov P, Hou J, Pu Y, Mahankali S, Feng CM, Yee SH, Wan YL, Fox PT, Gao JH. Perfusion-weighted imaging of interictal hypoperfusion in temporal lobe epilepsy using FAIR-HASTE: comparison with H(2)(15)O PET measurements. *Magnet Reson Med* 2001;45(3):431-435.
  28. Engelhorn T, Doerfler A, Weise J, Baehr M, Forsting M, Hufnagel A. Cerebral perfusion alterations during the acute phase of experimental generalized status epilepticus: prediction of survival by using perfusion-weighted MR imaging and histopathology. *AJNR Am J Neuroradiol* 2005;26(6):1563-1570.
  29. Pollock JM, Tan H, Kraft RA, Whitlow CT, Burdette JH, Maldjian JA. Arterial spin-labeled MR perfusion imaging: clinical applications. *Magn Reson Imaging Clin N Am* 2009;17(2):315-338.
  30. Detre JA, Wang JJ. Technical aspects and utility of fMRI using BOLD and ASL. *Clin Neurophysiol* 2002;113(5):621-634.

31. Ogawa S, Tank DW, Menon R, Ellermann JM, Kim SG, Merkle H, Ugurbil K. Intrinsic Signal Changes Accompanying Sensory Stimulation - Functional Brain Mapping with Magnetic-Resonance-Imaging. *P Natl Acad Sci USA* 1992;89(13):5951-5955.
32. Villringer A, Rosen BR, Belliveau JW, Ackerman JL, Lauffer RB, Buxton RB, Chao YS, Wedeen VJ, Brady TJ. Dynamic imaging with lanthanide chelates in normal brain: contrast due to magnetic susceptibility effects. *Magnet Reson Med* 1988;6(2):164-174.
33. Rosen BR, Belliveau JW, Vevea JM, Brady TJ. Perfusion imaging with NMR contrast agents. *Magnet Reson Med* 1990;14(2):249-265.
34. Zierler KL. Equations for Measuring Blood Flow by External Monitoring of Radioisotopes. *Circulation Research* 1965;16:309-321.
35. Axel L. Cerebral blood flow determination by rapid-sequence computed tomography: theoretical analysis. *Radiology* 1980;137(3):679-686.
36. Boxerman JL, Hamberg LM, Rosen BR, Weisskoff RM. MR contrast due to intravascular magnetic susceptibility perturbations. *Magnet Reson Med* 1995;34(4):555-566.
37. Reiter T, Ritter O, Prince MR, Nordbeck P, Wanner C, Nagel E, Bauer WR. Minimizing Risk of Nephrogenic systemic fibrosis in Cardiovascular Magnetic Resonance. *J Cardiovasc Magn Reson* 2012;14(1):31.
38. Weisskoff RM, Zuo CS, Boxerman JL, Rosen BR. Microscopic susceptibility variation and transverse relaxation: theory and experiment. *Magnet Reson Med* 1994;31(6):601-610.
39. Lev MH, Kulke SF, Sorensen AG, Boxerman JL, Brady TJ, Rosen BR, Buchbinder BR, Weisskoff RM. Contrast-to-noise ratio in functional MRI of relative cerebral blood volume with sprodiamide injection. *J Magn Reson Imaging* 1997;7(3):523-527.
40. Inoue S, Kabuto T, Masunaga S, Souma T, Takaki A, Hosoya T, Yoshioka K, Ito S. Determination of the Optimal ROI Setting Position of the Input Function for the (99m)Tc-ethyl Cysteinate Dimmer Brain Uptake Ratio Method. *Nihon Hoshasen Gijutsu Gakkai Zasshi* 2012;68(3):269-276.
41. Bleeker EJW, van Buchem MA, Webb AG, van Osch MJP. Phase-Based Arterial Input Function Measurements for Dynamic Susceptibility Contrast MRI. *Magnet Reson Med* 2010;64(2):358-368.
42. Rosen BR, Belliveau JW, Buchbinder BR, McKinstry RC, Porkka LM, Kennedy DN, Neuder MS, Fisel CR, Aronen HJ, Kwong KK, et al. Contrast agents and cerebral hemodynamics. *Magnet Reson Med* 1991;19(2):285-292.
43. Detre JA, Leigh JS, Williams DS, Koretsky AP. Perfusion Imaging. *Magnet Reson Med* 1992;23(1):37-45.
44. Williams DS, Detre JA, Leigh JS, Koretsky AP. Magnetic-Resonance-Imaging of Perfusion Using Spin Inversion of Arterial Water. *P Natl Acad Sci USA* 1992;89(1):212-216.
45. Wong EC, Buxton RB, Frank LR. A theoretical and experimental comparison of continuous and pulsed arterial spin labeling techniques for quantitative perfusion imaging. *Magnet Reson Med* 1998;40(3):348-355.
46. Wang J, Alsop DC, Li L, Listerud J, Gonzalez-At JB, Schnall MD, Detre JA. Comparison of quantitative perfusion imaging using arterial spin labeling at 1.5 and 4.0 Tesla. *Magnet Reson Med* 2002;48(2):242-254.



47. Edelman RR, Siewert B, Darby DG, Thangaraj V, Nobre AC, Mesulam MM, Warach S. Qualitative mapping of cerebral blood flow and functional localization with echo-planar MR imaging and signal targeting with alternating radio frequency. *Radiology* 1994;192(2):513-520.
48. Wong EC, Buxton RB, Frank LR. Quantitative imaging of perfusion using a single subtraction (QUIPSS and QUIPSS II). *Magnet Reson Med* 1998;39(5):702-708.
49. Kim SG. Quantification of relative cerebral blood flow change by flow-sensitive alternating inversion recovery (FAIR) technique: application to functional mapping. *Magnet Reson Med* 1995;34(3):293-301.
50. Golay X, Stuber M, Pruessmann KP, Meier D, Boesiger P. Transfer insensitive labeling technique (TILT): Application to multislice functional perfusion imaging. *Jmri-J Magn Reson Im* 1999;9(3):454-461.
51. Golay X, Petersen ET, Hui F. Pulsed star labeling of arterial regions (PULSAR): a robust regional perfusion technique for high field imaging. *Magnet Reson Med* 2005;53(1):15-21.
52. Schwarzbauer C, Heinke W. BASE imaging: a new spin labeling technique for measuring absolute perfusion changes. *Magnet Reson Med* 1998;39(5):717-722.
53. Wong EC, Buxton RB, Frank LR. Implementation of quantitative perfusion imaging techniques for functional brain mapping using pulsed arterial spin labeling. *Nmr Biomed* 1997;10(4-5):237-249.
54. Tanabe JL, Yongbi M, Branch C, Hrabe J, Johnson G, Helpner JA. MR perfusion imaging in human brain using the UNFAIR technique. Un-inverted flow-sensitive alternating inversion recovery. *J Magn Reson Imaging* 1999;9(6):761-767.
55. Mai VM, Berr SS. MR perfusion imaging of pulmonary parenchyma using pulsed arterial spin labeling techniques: FAIRER and FAIR. *J Magn Reson Imaging* 1999;9(3):483-487.
56. Gai ND, Talagala SL, Butman JA. Whole-brain cerebral blood flow mapping using 3D echo planar imaging and pulsed arterial tagging. *J Magn Reson Imaging* 2011;33(2):287-295.
57. Dai WY, Garcia D, de Bazelaire C, Alsop DC. Continuous Flow-Driven Inversion for Arterial Spin Labeling Using Pulsed Radio Frequency and Gradient Fields. *Magnet Reson Med* 2008;60(6):1488-1497.
58. Wu WC, Fernandez-Seara M, Detre JA, Wehrli FW, Wang J. A theoretical and experimental investigation of the tagging efficiency of pseudocontinuous arterial spin labeling. *Magnet Reson Med* 2007;58(5):1020-1027.
59. Wong EC, Cronin M, Wu WC, Inglis B, Frank LR, Liu TT. Velocity-selective arterial spin labeling. *Magnet Reson Med* 2006;55(6):1334-1341.
60. Wu WC, Wong EC. Feasibility of velocity selective arterial spin labeling in functional MRI. *J Cerebr Blood F Met* 2007;27(4):831-838.
61. Ye FQ, Frank JA, Weinberger DR, McLaughlin AC. Noise reduction in 3D perfusion imaging by attenuating the static signal in arterial spin tagging (ASSIST). *Magnet Reson Med* 2000;44(1):92-100.
62. Henkelman RM, Huang X, Xiang QS, Stanisz GJ, Swanson SD, Bronskill MJ. Quantitative interpretation of magnetization transfer. *Magnet Reson Med* 1993;29(6):759-766.

63. Zhang W, Silva AC, Williams DS, Koretsky AP. NMR measurement of perfusion using arterial spin labeling without saturation of macromolecular spins. *Magnet Reson Med* 1995;33(3):370-376.
64. Shen Q, Duong TQ. Background suppression in arterial spin labeling MRI with a separate neck labeling coil. *Nmr in Biomedicine* 2011;24(9):1111-1118.
65. Talagala SL, Ye FQ, Ledden PJ, Chesnick S. Whole-brain 3D perfusion MRI at 3.0 T using CASL with a separate labeling coil. *Magnet Reson Med* 2004;52(1):131-140.
66. Hendrikse J, van Osch MJ, Rutgers DR, Bakker CJ, Kappelle LJ, Golay X, van der Grond J. Internal carotid artery occlusion assessed at pulsed arterial spin-labeling perfusion MR imaging at multiple delay times. *Radiology* 2004;233(3):899-904.
67. Ciobanu L. High Resolution MR Microscopy [PhD]. Columbus, OH: Ohio State University; 2002. 79 p.
68. Ciobanu L, Seeber DA, Pennington CH. 3D MR Microscopy with resolution 3.7 $\mu$ m by 3.3 $\mu$ m by 3.3 $\mu$ m. *J Magn Reson* 2002;158:178-182.
69. Lauterbur PC, Hyslop WB, Morris HD. NMR microscopy: old resolutions and new desires. XI International Society of Magnetic Resonance Conference. Vancouver, B.C.; 1992.
70. Pennington CH. Prospects for Diffusion Enhancement of Signal and Resolution (DESIRE) in Magnetic Resonance Microscopy. submitted to *Concepts in Magnetic Resonance* 2003.
71. Ciobanu L, Webb AG, Pennington CH. Signal enhancement by diffusion: experimental observation of the "DESIRE" effect. *J Magn Reson* 2004;170:252-256.
72. Weiger M, Zeng Y, Fey M. A closer look into DESIRE for NMR microscopy. *J Magn Reson* 2008;190(1):95-104.
73. Jelescu IO, Boulant N, Le Bihan D, Ciobanu L. Experimental demonstration of diffusion signal enhancement in 2D DESIRE images. *J Magn Reson* 2012;218:44-48.
74. Heo S, Prakash RS, Voss MW, Erickson KI, Ouyang C, Sutton BP, Kramer AF. Resting hippocampal blood flow, spatial memory and aging. *Brain Res* 2010;1315C:119-127.
75. Reynaud O, Ciobanu L. Post-processing correction of magnetization transfer effects in FENSI perfusion MRI data. *Magnet Reson Med* 2011;65(2):457-462.
76. Wolff SD, Balaban RS. Magnetization transfer contrast (MTC) and tissue water proton relaxation in vivo. *Magnet Reson Med* 1989;10(1):135-144.
77. Henkelman RM, Stanisz GJ, Graham SJ. Magnetization transfer in MRI: a review. *Nmr Biomed* 2001;14(2):57-64.
78. Wolff SD, Chesnick S, Frank JA, Lim KO, Balaban RS. Magnetization transfer contrast: MR imaging of the knee. *Radiology* 1991;179(3):623-628.
79. Wolff SD, Balaban RS. Magnetization transfer imaging: practical aspects and clinical applications. *Radiology* 1994;192(3):593-599.
80. Grossman RI, Gomori JM, Ramer KN, Lexa FJ, Schnall MD. Magnetization transfer: theory and clinical applications in neuroradiology. *Radiographics* 1994;14(2):279-290.

81. Yang YH. Perfusion MR imaging with pulsed arterial spin-labeling: Basic principles and applications in functional brain imaging. *Concept Magnetic Res* 2002;14(5):347-357.
82. Wittlich F, Kohno K, Mies G, Norris DG, Hoehnberlage M. Quantitative Measurement of Regional Blood-Flow with Gadolinium Diethylenetriaminepentaacetate Bolus Track Nmr Imaging in Cerebral Infarcts in Rats - Validation with the Iodo[C-14]Antipyrine Technique. *P Natl Acad Sci USA* 1995;92(6):1846-1850.
83. Vannucci RC, Lyons DT, Vasta F. Regional cerebral blood flow during hypoxia-ischemia in immature rats. *Stroke* 1988;19(2):245-250.
84. Beg SA, Hansen-Schwartz JA, Vikman PJ, Xu CB, Edvinsson LI. ERK1/2 inhibition attenuates cerebral blood flow reduction and abolishes ET(B) and 5-HT(1B) receptor upregulation after subarachnoid hemorrhage in rat. *J Cereb Blood Flow Metab* 2006;26(6):846-856.
85. Ouyang C, Sutton BP. Localized blood flow imaging using quantitative flow-enhanced signal intensity. *Magnet Reson Med* 2012;67(3):660-668.
86. Petersen ET, Zimine I, Ho YCL, Golay X. Non-invasive measurement of perfusion: a critical review of arterial spin labelling techniques. *Brit J Radiol* 2006;79(944):688-701.
87. Herscovitch P, Raichle ME. What is the correct value for the brain--blood partition coefficient for water? *J Cereb Blood Flow Metab* 1985;5(1):65-69.
88. Leithner C, Muller S, Fuchtemeier M, Lindauer U, Dirnagl U, Roysl G. Determination of the brain-blood partition coefficient for water in mice using MRI. *J Cereb Blood Flow Metab* 2010;30(11):1821-1824.
89. Ohgaki H, Kleihues P. Epidemiology and etiology of gliomas. *Acta Neuropathol* 2005;109(1):93-108.
90. Mineo JF, Bordron A, Baroncini M, Ramirez C, Maurage CA, Blond S, Dam-Hieu P. Prognosis factors of survival time in patients with glioblastoma multiforme: a multivariate analysis of 340 patients. *Acta Neurochir (Wien)* 2007;149(3):245-252; discussion 252-243.
91. Van Meir EG, Hadjipanayis CG, Norden AD, Shu HK, Wen PY, Olson JJ. Exciting New Advances in Neuro-Oncology The Avenue to a Cure for Malignant Glioma. *Ca-Cancer J Clin* 2010;60(3):166-193.
92. Lamar RE, Spigel DR, Burris HA, Markus TM, Kuzur M, Ervin T, Fichtel L, Greco FA, Hainsworth JD. Phase II trial of radiation therapy/temozolomide followed by temozolomide/sorafenib in the first-line treatment of glioblastoma multiforme (GBM). *J Clin Oncol* 2009;27(15).
93. Radner H, Blumcke I, Reifenberger G, Wiestler OD. The new WHO classification of tumors of the nervous system 2000. *Pathology and genetics. Pathologie* 2002;23(4):260-283.
94. Folkman J, Merler E, Abernathy C, Williams G. Isolation of a tumor factor responsible for angiogenesis. *J Exp Med* 1971;133(2):275-288.
95. Yancopoulos GD, Davis S, Gale NW, Rudge JS, Wiegand SJ, Holash J. Vascular-specific growth factors and blood vessel formation. *Nature* 2000;407(6801):242-248.
96. Carmeliet P. Mechanisms of angiogenesis and arteriogenesis. *Nat Med* 2000;6(4):389-395.
97. Belfi CA, Ting LL, Hassenbusch SJ, Tefft M, Ngo FQH. Determination of Changes in Tumor Blood Perfusion after Hydralazine Treatment by

- Dynamic Paramagnetic-Enhanced Magnetic-Resonance-Imaging. *Int J Radiat Oncol* 1992;22(3):477-482.
98. Soyer P, Dufresne AC, Somveille E, Lenormand S, Scherrer A, Rymer R. Differentiation between hepatic cavernous hemangioma and malignant tumor with T2-weighted MRI: Comparison of fast spin-echo and breathhold fast spin-echo pulse sequences. *Clin Imag* 1998;22(3):200-210.
  99. Lev MH. Glial tumor grading and outcome prediction using dynamic spin-echo MR susceptibility mapping compared with conventional contrast-enhanced MR: Confounding effect of elevated rCBV of oligodendrogliomas (vol 25, pg 214, 2004). *Am J Neuroradiol* 2004;25(3):B1-B1.
  100. Colvin DC, Loveless ME, Does MD, Yue Z, Yankeelov TE, Gore JC. Earlier detection of tumor treatment response using magnetic resonance diffusion imaging with oscillating gradients. *Magnetic Resonance Imaging* 2011;29(3):315-323.
  101. Kimura H, Takeuchi H, Koshimoto Y, Arishima H, Uematsu H, Kawamura Y, Kubota T, Itoh H. Perfusion imaging of meningioma by using continuous arterial spin-labeling: Comparison with dynamic susceptibility-weighted contrast-enhanced MR images and histopathologic features. *Am J Neuroradiol* 2006;27(1):85-93.
  102. Weber MA, Zoubaa S, Schlieter M, Juttler E, Huttner HB, Geletneky K, Ittrich C, Lichy MP, Kroll A, Debus J, Giesel FL, Hartmann M, Essig M. Diagnostic performance of spectroscopic and perfusion MRI for distinction of brain tumors. *Neurology* 2006;66(12):1899-1906.
  103. Law M, Yang S, Wang H, Babb JS, Johnson G, Cha S, Knopp EA, Zagzag D. Glioma grading: sensitivity, specificity, and predictive values of perfusion MR imaging and proton MR spectroscopic imaging compared with conventional MR imaging. *AJNR Am J Neuroradiol* 2003;24(10):1989-1998.
  104. Brown SL, Ewing JR, Kolozsvary A, Butt S, Cao Y, Kim JH. Magnetic resonance imaging of perfusion in rat cerebral 9L tumor after nicotinamide administration. *Int J Radiat Oncol* 1999;43(3):627-633.
  105. Rong Y, Durden DL, Van Meir EG, Brat DJ. 'Pseudopalisading' necrosis in glioblastoma: a familiar morphologic feature that links vascular pathology, hypoxia, and angiogenesis. *J Neuropathol Exp Neurol* 2006;65(6):529-539.
  106. Cavusoglu M, Pfeuffer J, Ugurbil K, Uludag K. Comparison of pulsed arterial spin labeling encoding schemes and absolute perfusion quantification. *Magn Reson Imaging* 2009;27(8):1039-1045.
  107. Silva AC, Kim SG, Garwood M. Imaging blood flow in brain tumors using arterial spin labeling. *Magnet Reson Med* 2000;44(2):169-173.
  108. Gaa J, Warach S, Wen P, Thangaraj V, Wielopolski P, Edelman RR. Noninvasive perfusion imaging of human brain tumors with EPISTAR. *Eur Radiol* 1996;6(4):518-522.
  109. Moffat BA, Chen M, Kariaapper MS, Hamstra DA, Hall DE, Stojanovska J, Johnson TD, Blaivas M, Kumar M, Chenevert TL, Rehemtulla A, Ross BD. Inhibition of vascular endothelial growth factor (VEGF)-A causes a paradoxical increase in tumor blood flow and up-regulation of VEGF-D. *Clin Cancer Res* 2006;12(5):1525-1532.

110. Unekawa M, Tomita M, Tomita Y, Toriumi H, Miyaki K, Suzuki N. RBC velocities in single capillaries of mouse and rat brains are the same, despite 10-fold difference in body size. *Brain Res* 2010;1320:69-73.
111. Hudetz AG. Blood flow in the cerebral capillary network: A review emphasizing observations with intravital microscopy. *Microcirculation* 1997;4(2):233-252.
112. Schmidek HH, Nielsen SL, Schiller AL, Messer J. Morphological studies of rat brain tumors induced by N-nitrosomethylurea. *J Neurosurg* 1971;34(3):335-340.
113. Benda P, Someda K, Messer J, Sweet WH. Morphological and immunochemical studies of rat glial tumors and clonal strains propagated in culture. *J Neurosurg* 1971;34(3):310-323.
114. Henderson SD, Kimler BF, Morantz RA. Radiation therapy of 9L rat brain tumors. *Int J Radiat Oncol Biol Phys* 1981;7(4):497-502.
115. Vats TS, Morantz RA, Wood GW, Tilzer S. Study of effectiveness of bleomycin in rat brain tumor model intravenously and intracerebrally. *Int J Radiat Oncol Biol Phys* 1979;5(9):1527-1529.
116. Barker M, Hoshino T, Gurcay O, Wilson CB, Nielsen SL, Downie R, Eliason J. Development of an animal brain tumor model and its response to therapy with 1,3-bis(2-chloroethyl)-1-nitrosourea. *Cancer Res* 1973;33(5):976-986.
117. Barker M, Deen DF, Baker DG. BCNU and X-ray therapy of intracerebral 9L rat tumors. *Int J Radiat Oncol Biol Phys* 1979;5(9):1581-1583.
118. Kimler BF, Martin DF, Evans RG, Morantz RA, Vats TS. Combination of Radiation-Therapy and Intracranial Bleomycin in the 9L Rat-Brain Tumor-Model. *Int J Radiat Oncol* 1990;18(5):1115-1121.
119. Fleshner M, Watkins LR, Redd JM, Kruse CA, Bellgrau D. A 9L gliosarcoma transplantation model for studying adoptive immunotherapy into the brains of conscious rats. *Cell Transplant* 1992;1(4):307-312.
120. Kruse CA, Lillehei KO, Mitchell DH, Kleinschmidt-DeMasters B, Bellgrau D. Analysis of interleukin 2 and various effector cell populations in adoptive immunotherapy of 9L rat gliosarcoma: allogeneic cytotoxic T lymphocytes prevent tumor take. *Proc Natl Acad Sci U S A* 1990;87(24):9577-9581.
121. Barba D, Hardin J, Ray J, Gage FH. Thymidine kinase-mediated killing of rat brain tumors. *J Neurosurg* 1993;79(5):729-735.
122. Kim JH, Kim SH, Kolozsvary A, Brown SL, Kim OB, Freytag SO. Selective enhancement of radiation response of herpes simplex virus thymidine kinase transduced 9L gliosarcoma cells in vitro and in vivo by antiviral agents. *Int J Radiat Oncol Biol Phys* 1995;33(4):861-868.
123. Ram Z, Walbridge S, Shawker T, Culver KW, Blaese RM, Oldfield EH. The effect of thymidine kinase transduction and ganciclovir therapy on tumor vasculature and growth of 9L gliomas in rats. *J Neurosurg* 1994;81(2):256-260.
124. Tapscott SJ, Miller AD, Olson JM, Berger MS, Groudine M, Spence AM. Gene therapy of rat 9L gliosarcoma tumors by transduction with selectable genes does not require drug selection. *Proc Natl Acad Sci U S A* 1994;91(17):8185-8189.

125. Stojiljkovic M, Piperski V, Dacevic M, Rakic L, Ruzdijic S, Kanazir S. Characterization of 9L glioma model of the Wistar rat. *J Neurooncol* 2003;63(1):1-7.
126. Fross RD, Warnke PC, Groothuis DR. Blood-Flow and Blood-to-Tissue Transport in 9L-Gliosarcomas - the Role of the Brain-Tumor Model in Drug Delivery Research. *J Neuro-Oncol* 1991;11(3):185-197.
127. Darpolor MM, Molthen RC, Schmainda KM. Multimodality imaging of abnormal vascular perfusion and morphology in preclinical 9L gliosarcoma model. *PLoS One* 2011;6(1):e16621.
128. Silva AC, Zhang W, Williams DS, Koretsky AP. Estimation of water extraction fractions in rat brain using magnetic resonance measurement of perfusion with arterial spin labeling. *Magnet Reson Med* 1997;37(1):58-68.
129. Wang X, Duan X, Yang G, Zhang X, Deng L, Zheng H, Deng C, Wen J, Wang N, Peng C, Zhao X, Wei Y, Chen L. Honokiol crosses BBB and BCSFB, and inhibits brain tumor growth in rat 9L intracerebral gliosarcoma model and human U251 xenograft glioma model. *PLoS One* 2011;6(4):e18490.
130. Lemasson B, Serduc R, Maisin C, Bouchet A, Coquery N, Robert P, Le Duc G, Tropres I, Remy C, Barbier EL. Monitoring Blood-Brain Barrier Status in a Rat Model of Glioma Receiving Therapy: Dual Injection of Low-Molecular-Weight and Macromolecular MR Contrast Media. *Radiology* 2010;257(2):342-352.
131. Quarles CC, Schmainda KM. Assessment of the morphological and functional effects of the anti-angiogenic agent SU11657 on 9L gliosarcoma vasculature using dynamic susceptibility contrast MRI. *Magnet Reson Med* 2007;57(4):680-687.
132. Barth RF. Rat brain tumor models in experimental neuro-oncology: The 9L, C6, T9, F98, RG2 (D74), RT-2 and CNS-1 gliomas. *J Neuro-Oncol* 1998;36(1):91-102.
133. Weizsaecker M, Deen DF, Rosenblum ML, Hoshino T, Gutin PH, Barker M. The 9L rat brain tumor: description and application of an animal model. *J Neurol* 1981;224(3):183-192.
134. Plate KH, Breier G, Millauer B, Ullrich A, Risau W. Up-regulation of vascular endothelial growth factor and its cognate receptors in a rat glioma model of tumor angiogenesis. *Cancer Res* 1993;53(23):5822-5827.
135. Doblus S, He T, Saunders D, Pearson J, Hoyle J, Smith N, Lerner M, Towner RA. Glioma morphology and tumor-induced vascular alterations revealed in seven rodent glioma models by in vivo magnetic resonance imaging and angiography. *J Magn Reson Imaging* 2010;32(2):267-275.
136. Ullrich RT, Jikeli JF, Diedenhofen M, Bohm-Sturm P, Unruh M, Vollmar S, Hoehn M. In-vivo visualization of tumor microvessel density and response to anti-angiogenic treatment by high resolution MRI in mice. *PLoS One* 2011;6(5):e19592.
137. Doblus S, He T, Saunders D, Pearson J, Hoyle J, Smith N, Lerner M, Towner RA. Glioma Morphology and Tumor-Induced Vascular Alterations Revealed in Seven Rodent Glioma Models by In Vivo Magnetic Resonance Imaging and Angiography. *Journal of Magnetic Resonance Imaging* 2010;32(2):267-275.

138. Peterson DL, Sheridan PJ, Brown WE, Jr. Animal models for brain tumors: historical perspectives and future directions. *J Neurosurg* 1994;80(5):865-876.
139. Guo M, Roman RJ, Fenstermacher JD, Brown SL, Falck JR, Arbab AS, Edwards PA, Scicli AG. 9L gliosarcoma cell proliferation and tumor growth in rats are suppressed by N-hydroxy-N'-(4-butyl-2-methylphenol) formamidine (HET0016), a selective inhibitor of CYP4A. *J Pharmacol Exp Ther* 2006;317(1):97-108.
140. Miller CR, Perry A. Glioblastoma. *Arch Pathol Lab Med* 2007;131(3):397-406.
141. Belliveau JW, Kennedy DN, McKinstry RC, Buchbinder BR, Weisskoff RM, Cohen MS, Vevea JM, Brady TJ, Rosen BR. Functional Mapping of the Human Visual-Cortex by Magnetic-Resonance-Imaging. *Science* 1991;254(5032):716-719.
142. Turner R, LeBihan D, Moonen CTW, Despres D, Frank J. Echo-Planar Time Course Mri of Cat Brain Oxygenation Changes. *Magnet Reson Med* 1991;22(1):159-166.
143. Ogawa S, Lee TM, Kay AR, Tank DW. Brain Magnetic-Resonance-Imaging with Contrast Dependent on Blood Oxygenation. *P Natl Acad Sci USA* 1990;87(24):9868-9872.
144. Ogawa S, Lee TM, Nayak AS, Glynn P. Oxygenation-Sensitive Contrast in Magnetic-Resonance Image of Rodent Brain at High Magnetic-Fields. *Magnet Reson Med* 1990;14(1):68-78.
145. Silva AC, Lee SP, Iadecola C, Kim SG. Early temporal characteristics of cerebral blood flow and deoxyhemoglobin changes during somatosensory stimulation. *J Cerebr Blood F Met* 2000;20(1):201-206.
146. Lee AT, Glover GH, Meyer CH. Discrimination of Large Venous Vessels in Time-Course Spiral Blood-Oxygen-Level-Dependent Magnetic-Resonance Functional Neuroimaging. *Magnet Reson Med* 1995;33(6):745-754.
147. Kim SG, Hendrich K, Hu XP, Merkle H, Ugurbil K. Potential Pitfalls of Functional Mri Using Conventional Gradient-Recalled Echo Techniques. *Nmr Biomed* 1994;7(1-2):69-74.
148. Chaigneau E, Oheim M, Audinat E, Charpak S. Two-photon imaging of capillary blood flow in olfactory bulb glomeruli. *P Natl Acad Sci USA* 2003;100(22):13081-13086.
149. Duvernoy HM, Delon S, Vannson JL. Cortical blood vessels of the human brain. *Brain Res Bull* 1981;7(5):519-579.
150. Kim SG, Ogawa S. Biophysical and physiological origins of blood oxygenation level-dependent fMRI signals. *J Cereb Blood Flow Metab* 2012.
151. Ekstrom A. How and when the fMRI BOLD signal relates to underlying neural activity: The danger in dissociation. *Brain Res Rev* 2010;62(2):233-244.
152. Logothetis NK. What we can do and what we cannot do with fMRI. *Nature* 2008;453(7197):869-878.
153. Hyder F, Behar KL, Martin MA, Blamire AM, Shulman RG. Dynamic Magnetic-Resonance-Imaging of the Rat-Brain during Forepaw Stimulation. *J Cerebr Blood F Met* 1994;14(4):649-655.
154. Masamoto K, Kim T, Fukuda M, Wang P, Kim SG. Relationship between neural, vascular, and BOLD signals in isoflurane-anesthetized rat somatosensory cortex. *Cereb Cortex* 2007;17(4):942-950.

155. Bock C, Krep H, Brinker G, Hoehn-Berlage M. Brainmapping of alpha-chloralose anesthetized rats with T-2\*-weighted imaging: distinction between the representation of the forepaw and hindpaw in the somatosensory cortex. *Nmr in Biomedicine* 1998;11(3):115-119.
156. Lu HB, Soltysik DA, Ward BD, Hyde JS. Temporal evolution of the CBV-fMRI signal to rat whisker stimulation of variable duration and intensity: A linearity analysis. *Neuroimage* 2005;26(2):432-440.
157. Spenger C, Josephson A, Klason T, Hoehn M, Schwindt W, Ingvar M, Olson L. Functional MRI at 4.7 Tesla of the rat brain during electric stimulation of forepaw, hindpaw, or tail in single- and multislice experiments. *Exp Neurol* 2000;166(2):246-253.
158. Ferris CF, Snowden CT, King JA, Duong TQ, Ziegler TE, Ugurbil K, Ludwig R, Schultz-Darken NJ, Wu ZJ, Olson DP, Sullivan JM, Tannenbaum PL, Vaughan JT. Functional imaging of brain activity in conscious monkeys responding to sexually arousing cues. *Neuroreport* 2001;12(10):2231-2236.
159. Lahti KM, Ferris CF, Li FH, Sotak CH, King JA. Imaging brain activity in conscious animals using functional MRI. *J Neurosci Meth* 1998;82(1):75-83.
160. Ueki M, Mies G, Hossmann KA. Effect of Alpha-Chloralose, Halothane, Pentobarbital and Nitrous-Oxide Anesthesia on Metabolic Coupling in Somatosensory Cortex of Rat. *Acta Anaesth Scand* 1992;36(4):318-322.
161. Vanhemelrijck J, Verhaegen M, Vanaken H. Cerebral Effects of Inhalational Anesthetics. *Bailliere Clin Anaes* 1993;7(4):1035-1055.
162. Griffin KM, Blau CW, Kelly ME, O'Herlihy C, O'Connell PR, Jones JF, Kerskens CM. Propofol allows precise quantitative arterial spin labelling functional magnetic resonance imaging in the rat. *Neuroimage* 2010;51(4):1395-1404.
163. Zhao FQ, Welsh D, Williams M, Coimbra A, Urban MO, Hargreaves R, Evelhoch J, Williams DS. fMRI of pain processing in the brain: A within-animal comparative study of BOLD vs. CBV and noxious electrical vs. noxious mechanical stimulation in rat. *Neuroimage* 2012;59(2):1168-1179.
164. Zhao FQ, Zhao TJ, Zhou L, Wu QL, Hu XP. BOLD study of stimulation-induced neural activity and resting-state connectivity in medetomidine-sedated rat. *Neuroimage* 2008;39(1):248-260.
165. Kim T, Masamoto K, Fukuda M, Vazquez A, Kim SG. Frequency-dependent neural activity, CBF, and BOLD fMRI to somatosensory stimuli in isoflurane-anesthetized rats. *Neuroimage* 2010;52(1):224-233.
166. Lu J, Dai G, Egi Y, Huang S, Kwon SJ, Lo EH, Kim YR. Characterization of cerebrovascular responses to hyperoxia and hypercapnia using MRI in rat. *Neuroimage* 2009;45(4):1126-1134.
167. Huttunen JK, Grohn O, Penttonen M. Coupling between simultaneously recorded BOLD response and neuronal activity in the rat somatosensory cortex. *Neuroimage* 2008;39(2):775-785.
168. Sanganahalli BG, Herman P, Hyder F. Frequency-dependent tactile responses in rat brain measured by functional MRI. *Nmr in Biomedicine* 2008;21(4):410-416.
169. van Zijl PC, Hua J, Lu H. The BOLD post-stimulus undershoot, one of the most debated issues in fMRI. *Neuroimage* 2012.



170. Yu X, Glen D, Wang SM, Dodd S, Hirano Y, Saad Z, Reynolds R, Silva AC, Koretsky AP. Direct imaging of macrovascular and microvascular contributions to BOLD fMRI in layers IV-V of the rat whisker-barrel cortex. *Neuroimage* 2012;59(2):1451-1460.
171. Reynaud O, Pyatigorskaya N, Petiet A, Le Bihan D, Ciobanu L. A robust protocol for Diffusion-Weighted functional MRI on rodents at 7 T. 2010; Florence.
172. Chen JJ, Pike GB. MRI measurement of the BOLD-specific flow-volume relationship during hypercapnia and hypocapnia in humans. *Neuroimage* 2010;53(2):383-391.
173. Grubb RL, Jr., Raichle ME, Eichling JO, Ter-Pogossian MM. The effects of changes in PaCO<sub>2</sub> on cerebral blood volume, blood flow, and vascular mean transit time. *Stroke* 1974;5(5):630-639.
174. Levine RL, Sunderland JJ, Rowe BR, Nickles RJ. The study of cerebral ischemic reversibility: Part II. Preliminary preoperative results of fluoromethane positron emission tomographic determination of perfusion reserve in patients with carotid TIA and stroke. *Am J Physiol Imaging* 1986;1(2):104-114.
175. Ziyeh S, Rick J, Reinhard M, Hetzel A, Mader I, Speck O. Blood oxygen level-dependent MRI of cerebral CO<sub>2</sub> reactivity in severe carotid stenosis and occlusion. *Stroke* 2005;36(4):751-756.
176. Cohen ER, Rostrup E, Sidaros K, Lund TE, Paulson OB, Ugurbil K, Kim SG. Hypercapnic normalization of BOLD fMRI: comparison across field strengths and pulse sequences. *Neuroimage* 2004;23(2):613-624.
177. Davis TL, Kwong KK, Weisskoff RM, Rosen BR. Calibrated functional MRI: mapping the dynamics of oxidative metabolism. *Proc Natl Acad Sci U S A* 1998;95(4):1834-1839.
178. Ciobanu L, Reynaud O, Uhrig L, Jarraya B, Le Bihan D. Effects of anesthetic agents on brain blood oxygenation level revealed with ultra-high field MRI. *PLoS One* 2012;7(3):e32645.
179. Ogawa S, Lee TM. Magnetic resonance imaging of blood vessels at high fields: in vivo and in vitro measurements and image simulation. *Magnet Reson Med* 1990;16(1):9-18.
180. Park SH, Masamoto K, Hendrich K, Kanno I, Kim SG. Imaging brain vasculature with BOLD microscopy: MR detection limits determined by in vivo two-photon microscopy. *Magnet Reson Med* 2008;59(4):855-865.
181. Marques JP, Maddage R, Mlynarik V, Gruetter R. On the origin of the MR image phase contrast: An in vivo MR microscopy study of the rat brain at 14.1 T. *Neuroimage* 2009;46:345- 352.
182. Barth M, Reichenbach JR, Venkatesan R, Moser E, Haacke EM. High-resolution, multiple gradient-echo functional MRI at 1.5 T. *Magn Reson Imaging* 1999;17(3):321-329.
183. Kundu P, Inati SJ, Evans JW, Luh WM, Bandettini PA. Differentiating BOLD and non-BOLD signals in fMRI time series using multi-echo EPI. *Neuroimage* 2012;60(3):1759-1770.
184. Peltier SJ, Noll DC. T(2)(\*) dependence of low frequency functional connectivity. *Neuroimage* 2002;16(4):985-992.
185. Menon RS, Ogawa S, Tank DW, Ugurbil K. Tesla Gradient Recalled Echo Characteristics of Photic Stimulation-Induced Signal Changes in the Human Primary Visual-Cortex. *Magnet Reson Med* 1993;30(3):380-386.

186. Turner R, Jezzard P, Wen H, Kwong KK, Le Bihan D, Zeffiro T, Balaban RS. Functional mapping of the human visual cortex at 4 and 1.5 tesla using deoxygenation contrast EPI. *Magnet Reson Med* 1993;29(2):277-279.
187. Gati JS, Menon RS, Ugurbil K, Rutt BK. Experimental determination of the BOLD field strength dependence in vessels and tissue. *Magnet Reson Med* 1997;38(2):296-302.
188. Yacoub E, Shmuel A, Pfeuffer J, Van de Moortele PF, Adriany G, Andersen P, Vaughan JT, Merkle H, Ugurbil K, Hu XP. Imaging brain function in humans at 7 Tesla. *Magnet Reson Med* 2001;45(4):588-594.
189. Chen Y, Wang DJ, Detre JA. Test-retest reliability of arterial spin labeling with common labeling strategies. *J Magn Reson Imaging* 2011;33(4):940-949.
190. Chen YF, Wang DJJ, Detre JA. Comparison of arterial transit times estimated using arterial spin labeling. *Magn Reson Mater Phy* 2012;25(2):135-144.
191. Wolf RL, Detre JA. Clinical neuroimaging using arterial spin-labeled perfusion magnetic resonance Imaging. *Neurotherapeutics* 2007;4(3):346-359.
192. Wells JA, Lythgoe MF, Gadian DG, Ordidge RJ, Thomas DL. In Vivo Hadamard Encoded Continuous Arterial Spin Labeling (H-CASL). *Magnet Reson Med* 2010;63(4):1111-1118.
193. Frank LR, Lu K, Wong EC. Perfusion Tensor Imaging. *Magnet Reson Med* 2008;60(6):1284-1291.
194. Bokkers RP, Hernandez DA, Merino JG, Mirasol RV, van Osch MJ, Hendrikse J, Warach S, Latour LL. Whole-brain arterial spin labeling perfusion MRI in patients with acute stroke. *Stroke* 2012;43(5):1290-1294.
195. Alsop DC, Detre JA. Multisection cerebral blood flow MR imaging with continuous arterial spin labeling. *Radiology* 1998;208(2):410-416.
196. Gunther M, Oshio K, Feinberg DA. Single-shot 3D imaging techniques improve arterial spin labeling perfusion measurements. *Magnet Reson Med* 2005;54(2):491-498.
197. Ouyang C, Sutton BP. Pseudo-continuous transfer insensitive labeling technique. *Magnet Reson Med* 2011;66(3):768-776.
198. Yan L, Kilroy E, Wang DJ. A Flexible framework of perfusion fMRI using Asymmetric Labeling and Control Acquisitions with Background Suppressed pCASL GRASE. 2012; Melbourne.
199. Lu H, Golay X, Pekar JJ, van Zijl PCM. Functional magnetic resonance Imaging based on changes in vascular space occupancy. *Magnet Reson Med* 2003;50(2):263-274.
200. Barth M, Moser E. Proton NMR relaxation times of human blood samples at 1.5 T and implications for functional MRI. *Cell Mol Biol* 1997;43(5):783-791.
201. Lu HZ, Clingman C, Golay X, van Zijl PCM. Determining the longitudinal relaxation time (T-1) of blood at 3.0 tesla. *Magnet Reson Med* 2004;52(3):679-682.
202. Silvennoinen MJ, Kettunen MI, Kauppinen RA. Effects of hematocrit and oxygen saturation level on blood spin-lattice relaxation. *Magnet Reson Med* 2003;49(3):568-571.

203. Dobre MC, Ugurbil K, Marjanska M. Determination of blood longitudinal relaxation time (T-1) at high magnetic field strengths. *Magn Reson Imaging* 2007;25(5):733-735.
204. Lin AL, Qin Q, Zhao X, Duong TQ. Blood longitudinal (T (1)) and transverse (T (2)) relaxation time constants at 11.7 Tesla. *MAGMA* 2012;25(3):245-249.

## **Appendix – List of relevant publications**

### Peer-reviewed journals

Reynaud O, Ciobanu L. Post-processing correction of magnetization transfer effects in FENSI perfusion MRI data. *Magnet Res Med* 2011;65(2):457-462.

Ciobanu L, Reynaud O, Uhrig L, Jarraya B, Le Bihan D. Effects of anesthetic agents on brain blood oxygenation level revealed with ultra-high field MRI. *PlosOne* 2012;7(3):e32645.

Reynaud O, Ciobanu L. Quantification of microvascular blood flux and late stage tumor compartmentalization in 9L gliosarcoma using flow-enhanced MRI. *NMR in Biomedicine*, submitted.

### Oral communications

Reynaud O, Pyatigorskaya N, Petiet A, Le Bihan D, Ciobanu L. A robust protocol for diffusion-weighted functional MRI on rodents at 7 T. *World Wide Magnetic Resonance Conference 2010, Florence* (presentation #314).

Reynaud O, Ciobanu L. FENSI MRI of glioma brain tumors in rat models. *European Society for Magnetic Resonance in Medicine and Biology 2011, Leipzig* (presentation #348).